

ELECTRICAL CHARACTERISTICS OF DIELECTRIC BARRIER  
DISCHARGE

TAY WEE HORNG

FACULTY OF SCIENCE  
UNIVERSITY OF MALAYA  
KUALA LUMPUR

2013

**ELECTRICAL CHARACTERISTICS OF DIELECTRIC  
BARRIER DISCHARGE**

**TAY WEE HORNG**

**DISSERTATION SUBMITTED IN FULFILMENT OF  
THE REQUIREMENTS FOR THE DEGREE OF  
MASTER OF SCIENCE**

**DEPARTMENT OF PHYSICS  
FACULTY OF SCIENCE  
UNIVERSITY OF MALAYA  
KUALA LUMPUR**

**2013**

# UNIVERSITI MALAYA

## ORIGINAL LITERARY WORK DECLARATION

Name of Candidate: **TAY WEE HORNG**

I/C/Passport No: **850616016045**

Registration/Matric No.: **SGR090057**

Name of Degree: **MASTER OF SCIENCE**

Title of Project Paper/Research Report/Dissertation/Thesis ("this Work"):

**"ELECTRICAL CHARACTERISTICS OF DIELECTRIC BARRIER DISCHARGE"**

Field of Study: **PLASMA TECHNOLOGY**

I do solemnly and sincerely declare that:

- (1) I am the sole author/writer of this Work,
- (2) This Work is original,
- (3) Any use of any work in which copyright exists was done by way of fair dealing and for permitted purposes and any excerpt or extract from, or reference to or reproduction of any copyright work has been disclosed expressly and sufficiently and the title of the Work and its authorship have been acknowledged in this Work,
- (4) I do not have any actual knowledge nor do I ought reasonably to know that the making of this work constitutes an infringement of any copyright work,
- (5) I hereby assign all and every rights in the copyright to this Work to the University of Malaya ("UM"), who henceforth shall be owner of the copyright in this Work and that any reproduction or use in any form or by any means whatsoever is prohibited without the written consent of UM having been first had and obtained,
- (6) I am fully aware that if in the course of making this Work I have infringed any copyright whether intentionally or otherwise, I may be subject to legal action or any other action as may be determined by UM.

(Candidate Signature) 

Date:

Subscribed and solemnly declared before,

Witness's Signature



**Professor Dr. Wong Chiow San**  
Jabatan Fizik  
Universiti Malaya  
50603 Kuala Lumpur

Date:

Name: **PROFESSOR DR WONG CHIOW SAN**

Designation:

Witness's Signature



Name: **DR YAP SEONG LING**

Designation

**Dr. Yap Seong Ling**  
Plasma Technology Research Center  
Department of Physics  
Faculty of Science  
University of Malaya  
50603 Kuala Lumpur

Date:

## ABSTRACT

The industrial application of the dielectric barrier discharge (DBD) has a long tradition. However, the lack of understanding of some of its fundamental issues, such as the stochastic behaviors, is still a challenge for DBD researchers. In this project, considerable efforts to understand the fundamental aspects of DBD have been made. The aim of this work is to study the electrical characteristics of DBD to determine a suitable condition for utilization of the device for applications. Several diagnostic tools such as high-voltage probe, resistive current, charge measurement, and high-speed camera imaging were employed for the investigation. In order to study the electrical behaviors of DBD, the experimental work was carried out in two parts: current pulse amplitude statistical studies and the energy investigation. For the pulse amplitude statistical studies, the stochastic variation of the current pulse amplitude has been analyzed by the statistical method. The stochastic behavior of the discharge current amplitude has been compared with a proposed empirical equation of the distribution pulse height. This proposed statistical function is found to be in good agreement with the experimental discharge pulse amplitude variation for discharges with varying space gaps. This empirical equation successfully predicts the existence of two discharge regimes, which were observed from the experimental results. For the energy investigation, the DBD dissipation energy was studied experimentally and numerically. A dynamic circuit model constructed with Matlab Simulink accurately simulated the discharge energy of DBD. The surface resistance introduced in this electrical model represents the average effect that effectively accounts for the resistance encountered by the charges between the discharging and non-discharging regions on the dielectric. The expanded QV Lissajous can be reasonably explained by the fact that the total energy is summed by the energy of the DBD discharge and the energy consumed by the spreading

charges on the dielectric surface. By having the experimental results accurately fitted with the simulated results from the model, the efficiency of discharge can be obtained from the electrical modeling. The efficiency of the DBD has been found to be higher with a smooth surface compared to a rough surface. The efficiency is reduced when the applied voltage is increased. Based on the energy and current pulse amplitude distribution model, the DBD system can be designed according to the desired condition by controlling the required energy efficiency and pulse height distribution.

## ABSTRAK

Nyahcas penghalang dielektrik (DBD) telah lama diaplikasikan dalam bidang industri. Walau bagaimanapun, kekurangan pemahaman, seperti sifat stokastik, masih merupakan satu cabaran dalam DBD pengajian. Dalam projek ini, kerja yang penting untuk mendapatkan pemahaman yang lebih mendalam telah disumbangkan. Kerja yang kami hasilkan adalah mengaji ciri-ciri nyahcas penghalang dielektrik (DBD) untuk mendapatkan keadaan aplikasi yang lebih berkesan. Beberapa peralatan yang tradisional telah digunakan untuk menentukan sifat DBD seperti penduga voltan tinggi, pengukuran arus, pengukuran caj, dan pengimejan kamera kelajuan tinggi. Untuk mengaji sifat elektrik, pengajian ini dijalankan dengan dua bahagian yang berasingan: cara statistik untuk nadi yang tidak stabil and pengukuran tenaga dengan QV Lissajous. Bagi bahagian statistik untuk nadi yang tidak stabil, sifat stokastik DBD dikajikan dengan cara statistik. DBD yang dikaji telah dibandingkan dengan kaedah statistik yang dicadangkan. Kaedah statistik ini memberi keterangan yang baik dalam pembentukan nyahcas yang impulsif dengan jarak jurang ruang yang berbeza. Kaedah statistik ini berjaya meramalkan kewujudan dua rejim dalam statistik ketinggian nadi yang didapati daripada eksperimen. Selain itu, kaedah ini boleh meramalkan statistik dengan tepat, jadi menambahkan kebolehan kita dalam mengawali DBD. Bagi pengukuran tenaga DBD, tenaga yang dipakai oleh DBD telah dikaji secara eksperimen dan berangka. Satu litar dynamic yang dibina dengan “Matlab Simulink” meramalkan tenaga nyahcas dengan jitu. Rintangan yang dikenali dalam pemodelan elektrik ini adalah kesan yang menjumlahkan rintangan yang dihadapi oleh caj antara rantau tidak bernyahcas dan rantau bernyahcas pada permukaan dielektrik. Pengembangan QV Lissajous boleh menjelaskan bahawa jumlah tenaga yang dipakai merangkumi tenaga DBD and tenaga yang dipakai untuk caj merebak di atas permukaan dielektrik. Dengan keputusan berangka yang berjaya menyamai keputusan eksperimen, kecekapan nyachas boleh

diperolehi daripada model elektrik ini. Kecekapan DBD yang didapati menunjukkan kecekapan yang lebih tinggi telah diperolehi dengan permukaan licin and kecekapan yang lebih rendah diperolehi dengan permukaan yang kasar. Kecekapan juga boleh dikurangkan dengan menaikkan bekalan voltan. Berdasarkan model elektrik dan kaedah statistik yang dicadangkan, sistem DBD boleh direka mengikut aplikasi yang dikehendaki dengan mengawal kecekapan tenaga dan pengedaran ketinggian nadi.

## ACKNOWLEDGEMENTS

I would like to thank my supervisor Professor Dr. Wong Chiow San and Dr. Yap Seong Ling for their guidance and advices throughout the entire project. This project would not be possible without their consistent guidance.

I also would like to acknowledge my appreciation to Mr. Jasbir Singh for his technical expertise and experience support. I am also thankful to Mr Ching Leng Chu for his assistance on my work.

I am very grateful for having wonderful friends during my life. I would like to address special thanks to the members of the Plasma Research Center, Li San, Siew Kien, Sang Huat, Yen Sian, Lian Kuang, Wei Xiang, Chee Yee, Farah, Yuen Sim, Sarah, Norhyati, Prasertsung, for their friendship, helpful and delightful discussions.

Finally yet importantly, I would like to thank my parents for their moral support and encouragement enabled me to pursue my master degree.



# TABLE OF CONTENT

|   | Page |
|---|------|
| <b>ABSTRACT</b>   | I    |
| <b>ABSTRAK</b>  | III  |
| <b>ACKNOWLEDGEMENTS</b>   | V    |
| <b>TABLE OF CONTENTS</b>  | VI   |
| <b>LIST OF FIGURES</b>  | XI   |
| <b>LIST OF TABLE</b>  | XV   |
| <b>NOMENCLATURE</b>   | XVI  |
| <br>  |      |
| <b>Chapter 1: Introduction and Literature Review</b>                                  | 1    |
| 1.1 History and Introduction  | 1    |
| 1.2 Applications of DBD   | 3    |
| 1.2.1 The ozone generator   | 4    |
| 1.2.2 Surface treatment   | 4    |
| 1.2.3 Pollution control   | 6    |
| 1.2.4 Extreme ultraviolet excimer, ultraviolet excimer and plasma<br>fluorescent lamp | 7    |
| 1.2.5 Flow control  | 7    |
| 1.2.6 Biomedical application  | 8    |
| 1.3 Research and Development  | 9    |
| 1.3.1 Introduction  | 9    |
| 1.3.2 The DBD discharge modes   | 9    |
| 1.3.3 Investigation of the filamentary current  | 12   |
| 1.3.4 General investigation of the filamentary discharge                              | 14   |

|  |  |        |
|--|--|--------|
| 1.3.5  | The optical emission spectroscopy                            | 16     |
| 1.4  | DBD Modeling   | 20     |
| 1.4.1  | Introduction of electrical modeling of DBD                   | 20     |
| 1.4.2  | Basic concept of the DBD electrical modeling                 | 21     |
| 1.4.3  | Lui and Neiger model   | 22     |
| 1.4.4  | Bhosle discrete volume model                                 | 24     |
| 1.4.5  | Barrientos model   | 26     |
| 1.4.6  | Pal single current model                                     | 28     |
| 1.4.7  | Summary of electrical models                                 | 28     |
| 1.5  | Objectives   | 30     |
| 1.6  | Dissertation Layout  | 30     |
| <br><b>Chapter 2: Experimental Setup and Methodology</b> |  | <br>31 |
| 2.1  | Experimental Setup   | 31     |
| 2.1.1  | The DBD reactor  | 31     |
| 2.1.2  | Power supply circuitry                                       | 34     |
| 2.2  | Diagnostic Techniques  | 35     |
| 2.2.1  | Introduction   | 35     |
| 2.2.2  | High voltage measurement                                     | 36     |
| 2.2.3  | Current measurement  | 36     |
| 2.2.4  | Charge measurement   | 37     |
| 2.3  | Basic Discharge Characteristics and Analysis Methods         | 38     |
| 2.3.1  | Typical discharge current and voltage profiles               | 38     |
| 2.3.2  | Measured current components                                  | 39     |
| 2.3.3  | Removal of displacement current and background noise         | 41     |
| 2.3.4  | The stochastic behaviors of time separation and pulse height | 43     |

|   |   |           |
|---|---|-----------|
| 2.3.5                                       | Temporal evolution of nanosecond pulse                                | 44        |
| 2.3.6                                       | Correlation of the pulse height and charge transferred                | 45        |
| 2.3.7                                       | Distribution of current pulse   | 47        |
| 2.3.8                                       | The space gap capacitance and dielectric capacitance                  | 48        |
| 2.3.9                                       | QV Lissajous figure under breakdown condition                         | 51        |
| 2.3.10                                      | The time evolution of space gap voltage and dielectric voltage        | 52        |
| <b>Chapter 3: Electrical Characteristic</b> |   | <b>55</b> |
| 3.1   | Introduction  | 55        |
| 3.2   | The Statistical Studies of Discharge Behavior of DBD                  | 56        |
| 3.2.1                                       | The experimental current pulse distribution                           | 56        |
| 3.2.2                                       | The time separation between consecutive current pulses                | 60        |
| 3.2.3                                       | The empirical distribution function                                   | 67        |
| 3.2.4                                       | Comparison of experimental results and proposed distribution function | 73        |
| 3.3   | Discharge Energy Consideration  | 77        |
| 3.3.1                                       | Observation of experimental QV Lissajous figure                       | 77        |
| 3.3.2                                       | The dynamic electrical circuit model                                  | 80        |
| 3.3.3                                       | Factor $D$ determination  | 83        |
| 3.3.4                                       | Matlab Simulink code  | 86        |
| 3.3.5                                       | Results and discussions   | 88        |

|   |     |
|---|-----|
| <b>Chapter 4: Conclusion and Suggestion for Future Work</b> | 100 |
| 4.1 Conclusion  | 100 |
| 4.2 Suggestion of Future Work                               | 103 |
| 4.2.1 High-speed imaging                                    | 103 |
| 4.2.2 Optical emission spectroscopy                         | 104 |
| 4.2.3 Homogenous discharge                                  | 105 |
| <b>References</b>   | 107 |
| <b>Appendix: Research outputs</b>                           | 118 |

## LIST OF FIGURES

- Figure 1.1:** The collection of different typical configurations of DBD.
- Figure 1.2:** Surface treatment and layer deposition by DBD (Wagner, et al., 2003).
- Figure 1.3:** The comparison of the current measurement between the homogenous discharges in left hand side, labeled as (a) with the filamentary discharge in right hand side labeled as (b) (Gherardi & Massines, 2001).
- Figure 1.4:** (a) The mix-discharge mode where the discharge current is due to combination of homogeneous discharge current and filamentary current pulses. (b) The two components are shown separated (Jidenko, et al., 2002).
- Figure 1.5:** The existence of two regime in the discharge statistical pattern was observed by Siliprandi (Siliprandi, et al., 2008).  $\langle Q_{tot} \rangle$  is the mean total charge transferred by the discharge current. Activity ration is the fraction of the current pulse duration to the total DBD “ON” time. The two regimes of discharge pattern are separated by 23.55 kV peak to peak applied voltage (regime transition voltage).
- Figure 1.6:** (a) Schematic diagram of the voltage and current waveform versus time. (b) Schematic diagram of voltage to charge Lissajous figure.
- Figure 1.7:** Emission spectra of  $N_2$  in the homogenous discharge (GDBD) and filamentary discharge (FDBD). The  $(ON_2)$  emission intensity is representative of the  $N_2(A^3\Sigma_u^+)$  metastable density. The  $(ON_2)$  emission is only observed in homogenous discharge (Massines, Segur, Gherardi, Khamphan, & Ricard, 2003).
- Figure 1.8:** The contour of the relative intensity shows the velocity of ion streamer increases with the distance from anode (Kozlov, Brandenburg, Wagner,

Morozov, & Michel, 2005).

- Figure 1.9:** The three different DBD arrangements studied by Hoder (Hoder, et al., 2010).
- Figure 1.10:** The single dielectric DBD reactor can be represented by the simplest equivalent electric circuit.
- Figure 1.11:** The dynamic electric circuit of the DBD reactor in Lui and Neiger model (Liu & Neiger, 2001, 2003).
- Figure 1.12:** The equivalent circuit for  $N_f$  filaments (Bhosle, Zissis, Damelin court, & Dawson, 2004).
- Figure 1.13:** Model implemented in Matlab Simulink software. (a) The general electrical circuit. (b) The coding block of MCB.
- Figure 1.14:** The comparison of the proposed filamentary discharge electric models.
- Figure 2.1:** Schematic diagram of the DBD arrangement.
- Figure 2.2:** Schematic diagram of DBD experimental setup.
- Figure 2.3:** Resistivity current measurement circuit.
- Figure 2.4:** Charge measurement circuit.
- Figure 2.5:** The typical filamentary discharge current pulse and applied voltage.
- Figure 2.6:** Step of the filamentary discharge current pulse analysis.
- Figure 2.7:** The diagram of the double stochastic DBD pulse.
- Figure 2.8:** The detected impulsive current of DBD and the calculated current by Equation 2.10.
- Figure 2.9:** The straight correlation between the charge and the pulse height.
- Figure 2.10:** The typical distribution of pulse height.
- Figure 2.11:** The total effective capacitance of DBD reactor before breakdown with negligible error.
- Figure 2.12:** The typical QV Lissajous under breakdown condition.

- Figure 2.13:** The space gap breakdown voltage versus the space gap distance.
- Figure 2.14:** The typical voltage waveform of the applied voltage, dielectric voltage, and space gap voltage. The gray color background is ON mode period. The white color background is OFF mode period.
- Figure 3.1:** The PDF of 0.5 mm space gap.
- Figure 3.2:** The PDF of 1.0 mm space gap.
- Figure 3.3:** The PDF of 1.5 mm space gap.
- Figure 3.4:** The PDF of 2.0 mm space gap.
- Figure 3.5:** Comparison of (a) the single point microdischarge with (b) multiple channels microdischarge.
- Figure 3.6:** The gradient of applied voltage near to the zero voltage is determined and only the pulses occur in this range of  $dV_T/dt$  are selected for analysis.
- Figure 3.7:** The correlation between the average height of current pulses and the average time separation for  $dV_T/dt$  of 2.629 GV/s, 3.396 GV/s and 4.080 GV/s.
- Figure 3.8:** The schematic diagram of the multiple microdischarge channels.
- Figure 3.9:** The comparison of experimental regime transition voltage with simulated result for discharges with 1.0 mm space gap.  $V_{pp}^t$  is the simulated regime transition voltage obtained by using Equation 3.20. The full line is simulated by using Equation 3.19 for each applied voltages.
- Figure 3.10:** The comparison of the computational results and experimental results for PDF with different space gaps with 35 kV pk-pk applied voltage.
- Figure 3.11:** The comparison between the experimental result (left) and the proposed density function of 2.0 mm space gap.

- Figure 3.12:** Comparison of the experimental current pulse amplitude with the simulated results.
- Figure 3.13:** Comparison of the experimentally detected number of pulses with the simulated results.
- Figure 3.14:** The experimental and theoretical QV Lissajous figure.
- Figure 3.15:** The equivalent circuit for filamentary discharge with surface resistors.
- Figure 3.16:** The electrical model of DBD and the dynamic currents in equivalent circuit.
- Figure 3.17:** The image from top view of DBD discharge.
- Figure 3.18:** The process to convert the image file to matrix format. The black color represents zero value and white color represents value 1.
- Figure 3.19:** The variation of factor  $D$  for discharges with various space gaps distance.
- Figure 3.20:** The interface of Matlab Simulink code.
- Figure 3.21:** The Simulink codes of (a) discharge current block, and (b) measurement analysis block.
- Figure 3.22:** The comparison between the experimental result and simulated result.
- Figure 3.23:** Comparison of (a) simulated and (b) experimental waveforms of the dissipation power of space gap and the total current for discharge with 0.5 mm air gap and 30 kV pk-pk applied voltage.
- Figure 3.24:** Comparison of (a) simulated and (b) experimental waveforms of the applied voltage  $V_T$ , air gap voltage  $V_g$ , and dielectric voltage  $V_d$  for discharge with 0.5 mm air gap and 30 kV pk-pk applied voltage.
- Figure 3.25:** QV Lissajous resulting from (a) simulation and (b) experiment for 0.2 mm air gap and various applied voltages when factor  $D$  and surface resistance are 0.013 and 2.18 M $\Omega$  respectively.



- Figure 3.26:** QV Lissajous resulting from (a) simulation and (b) experiment for 1.0 mm air gap and various applied voltages when factor  $D$  and surface resistance are 0.014 and 2.3 M $\Omega$  respectively.
- Figure 3.27:** QV Lissajous resulting from (a) simulation and (b) experiment for 1.0 mm air gap and rough dielectric surface when factor  $D$  and surface resistance are 0.017 and 4.5 M $\Omega$  respectively.
- Figure 3.28:** The total energy dissipated versus the applied voltage for DBD with various air gaps. The lines represent the simulated results and the symbols represent the experimental results.
- Figure 3.26:** The simulated total energy, discharge energy, surface energy, and efficiency versus the applied voltage for smooth dielectric with (a) 0.2 mm air gap, (b) 0.5 mm air gap, and (c) 1.0 mm air gap. For rough dielectric with 1.0 mm air gap the results are shown in (d).
- Figure 4.1:** Image of the single negative current pulse in the 5 mm gap DBD captured by ICCD camera with gate width of 500 ns. Three synchronous breakdowns were observed in a single negative discharge current pulse.
- Figure 4.2:** The DBD optical emission spectra under atmospheric gas.

## **LIST OF TABLE**

**Table 1.1** Nomenclature of electrical model.

**Table 3.1** List of the parameters used in the PDF function equation.

**Table 3.2** List of the simulation parameter.

## NOMENCLATURE

*Arabic*

| <b>Symbol</b> | <b>Description</b>   | <b>Unit</b>        |
|---------------|--|--------------------|
| $C_c$         | Charge monitor capacitance   | [F]                |
| $c_{cor}$     | Correction factor  | [-]                |
| $C_d$         | Dielectric capacitance   | [F]                |
| $C_{d,D}$     | Dielectric capacitance of discharge region   | [F]                |
| $C_{d,N}$     | Dielectric capacitance of non-discharge region   | [F]                |
| $C_g$         | Space gap capacitance  | [F]                |
| $C_{g,D}$     | Space gap capacitance of discharge region  | [F]                |
| $C_{g,N}$     | Space gap capacitance of non-discharge region  | [F]                |
| $C_{d,k}$     | Dielectric capacitance of channel k  | [F]                |
| $C_p$         | DBD capacitance  | [F]                |
| $C_T$         | Total effective capacitance of DBD reactor   | [F]                |
| $d$           | Distance of space gap  | [m]                |
| $D$           | Ratio of the total area of the discharging regions to the total area of the electrodes | [-]                |
| $E_{DBD}$     | Energy of the DBD discharge in one cycle   | [J]                |
| $E_{surface}$ | Energy consumed by the surface resistance in one cycle                                 | [J]                |
| $E_{Total}$   | Total dissipation energy of DBD system in one cycle                                    | [J]                |
| $f$           | Frequency of the applied voltage   | [s <sup>-1</sup> ] |
| $i$           | Pulse height   | [A]                |
| $i_o$         | Constants value depend on the gas used   | [A]                |
| $I_c$         | Displacement current   | [A]                |
| $I_{dect}$    | Detected external DBD current in the equivalent circuit                                | [A]                |

|             |   |                    |
|-------------|---|--------------------|
| $I_{dis}$   | Discharge current   | [A]                |
| $I_{limit}$ | Minimum detected value  | [A]                |
| $I_o$       | Constant value in the voltage controlled current source                           | [A]                |
| $I_{sf}$    | Total effective current of the surface discharge                                  | [A]                |
| $I_T(t)$    | Total measured current  | [A]                |
| $j$         | Imaginary value   | [-]                |
| $n_p(i)$    | Total number density of the pulses with current amplitude $i$                     | [A <sup>-1</sup> ] |
| $n_p(u)$    | Total number density function of the pulses with channel<br>breakdown voltage $u$ | [V <sup>-1</sup> ] |
| $n_c(u)$    | Total number density of channels with channel breakdown<br>voltage $u$            | [V <sup>-1</sup> ] |
| $N$         | Number of the detected pulses   | [-]                |
| $N_c$       | Total number of channels  | [-]                |
| $q(k)$      | Charge transfer from a single discharge pulse of channel $k$                      | [C]                |
| $Q(t)$      | Total charge transfer   | [C]                |
| $Q_T$       | Total charge transfer   | [C]                |
| $R_m$       | Current monitor resistance  | [Ω]                |
| $R_p$       | DBD resistance  | [Ω]                |
| $R_{probe}$ | Resistance of high voltage probe  | [Ω]                |
| $R_{sf}$    | Total effective resistance of the charge surface progresses                       | [Ω]                |
| $S$         | Effective total electrode area  | [m <sup>2</sup> ]  |
| $S_k$       | Effective occupied area of individual channel $k$                                 | [m <sup>2</sup> ]  |
| $t$         | Time  | [s]                |
| $t_s$       | Pulse starting time   | [s]                |
| $\bar{u}$   | Mean of the channel breakdown voltage   | [V]                |

|              |  |              |
|--------------|--|--------------|
| $u(k)$       | Space gap breakdown voltage of channel k                   | [V]          |
| $V_b$        | Peak to peak breakdown voltage of DBD system               | [V]          |
| $V_c$        | Voltage across the charge monitor capacitance              | [V]          |
| $V_d$        | Dielectric voltage   | [V]          |
| $V_{d,D}$    | Dielectric voltage of discharge region                     | [V]          |
| $V_{d,N}$    | Dielectric voltage of non-discharge region                 | [V]          |
| $V_g$        | Space gap voltage  | [V]          |
| $V_{g,b}$    | Space gap breakdown voltage                                | [V]          |
| $V_{g,D}$    | Space gap voltage of discharge region                      | [V]          |
| $V_{g,N}$    | Space gap voltage of non-discharge region                  | [V]          |
| $V_m(t)$     | Voltage across the current monitor resistor                | [V]          |
| $V_{nb}$     | Breakdown voltage in the voltage controlled current source | [V]          |
| $V_{pp}^t$   | Regime transition voltage                                  | [V]          |
| $V_T$        | Applied voltage  | [V]          |
| $V_{T,p}$    | Peak voltage of applied voltage                            | [V]          |
| $Z_{Load}$   | Load impedance   | [ $\Omega$ ] |
| $Z_{source}$ | Total impedance of the source                              | [ $\Omega$ ] |

*Greek*

| <b>Symbol</b> | <b>Description</b>  | <b>Unit</b>          |
|---------------|---|----------------------|
| $\alpha$      | Constants value depend on the gas used  | [V <sup>-1</sup> ]   |
| $\beta$       | Constant value in the voltage controlled current source                                       | [-]                  |
| $\gamma$      | Ratio of the amount of charge flowing to equivalent circuit to the total amount of DBD charge | [-]                  |
| $\epsilon_o$  | Vacuum permittivity   | [F.m <sup>-1</sup> ] |

|              |                                  |         |
|--------------|----------------------------------|---------|
| $\epsilon_r$ | Relative permittivity            | [-]     |
| $\theta$     | Calibration phase angle          | [rad]   |
| $\sigma$     | Standard deviation               | [V]     |
| $\tau_o$     | Time constant                    | [s]     |
| $\omega$     | Angular velocity of power supply | [rad/s] |

# Chapter 1: Introduction and Literature Review

## 1.1 History and Introduction

Non-thermal plasma is commonly generated under low pressure feeding gas. This type of plasma contains high density of excited species that can be responsible for many chemical reactions. However, it will be more convenient if the non-thermal plasma can be generated at atmospheric pressure. One of the successful approaches to generate non-thermal plasma in atmospheric pressure is the utilization of dielectric barrier discharge (DBD). The DBD is also known as the silent discharge, atmospheric discharge, and barrier discharges.

Werner Von Siemens developed the first DBD reactor for ozone generation in 1857. Initially, the DBD is mainly used for the ozone generator (Kogelschatz, 1990). In 1932, Buss showed that the DBD discharge composed of a large number of bright filaments covering the narrow space gap by a photographic trace. A uniform discharge obtained in DBD was later reported by Okazaki and his collaborators in 1988 and 1993 (Kanazawa, Kogoma, Moriwaki, & Okazaki, 1988; Okazaki, Kogoma, Uehara, & Kimura, 1993). They called the type of discharge as the atmospheric pressure glow discharge (APGD). Besides that, Eliasson (Eliasson, Hirth, & Kogelschatz, 1987) also studied the different modes of DBD, namely homogenous and filamentary modes.

The dielectric barrier discharges is commonly generated in the filamentary mode under atmospheric pressure. The numerous bright filament discharge may either regularly or randomly distributed over the discharge space gap (Kogelschatz, 2002). Even so, under a certain operating conditions, dielectric barrier discharges in a homogenous mode can be generated. The investigation of homogenous DBD was also

carried out by several other groups (Gherardi, Gouda, Gat, Ricard, & Massines, 2000; Roth, Rahel, Dai, & Sherman, 2005).

A method to estimate the filamentary discharge energy was proposed by Manley in 1943 (Manley, 1943). He used a voltage to charge Lissajous method, which is also known as QV Lissajous figure method to calculate the total dissipation energy of DBD. Besides, the DBD properties are experimentally studied by Eliasson (Eliasson, Egli, & Kogelschatz, 1994; Eliasson, et al., 1987). The mechanism of the transition between the two discharge modes has been studied based on optical investigation and electric measurement (Massines, Gherardi, Naude, & Segur, 2009; Massines, et al., 2003). More reviews on the early work and the application of DBD were presented by Kogelschatz (Kogelschatz, 2003; Kogelschatz, Eliasson, & Egli, 1997, 1999).

A DBD can be produced when at least one of the electrodes is covered by a dielectric layer, such as glass, quartz or ceramics. An alternating voltage or a repetitively pulsed power source can be used to power the DBD reactor. The function of the dielectric layer between the electrodes is to prevent the formation of arc discharge and to limit the DBD current. A space gap ranging from 0.1 mm to few cm is commonly applied under atmospheric air condition. In order to generate the DBD, the minimum peak to peak applied voltage must be higher than the breakdown voltage of the discharge. According to Paschen law, the breakdown electric field is about  $30 \text{ kVcm}^{-1}$  under atmospheric air condition.



## 1.2 Applications of DBD

In particular, DBD operated at the atmospheric air condition and 50 Hz power source is attractive because of its simplicity in configuration and power system. The affordable AC power supply can be used instead of the sophisticated pulsing circuits. The DBD reactor can also be scaled up in size or volume for industrial application. The flexibility of DBD configuration is also one of the advantages to be considered. The different geometric arrangements are shown in the Figure 1.1.

The configurations shown are the parallel plate (A-C), multi needle (D), needle to plate (E), needle to needle (F), surface discharge (G), actuator (H), coplanar discharge (I), wire mesh (J), cylindrical (K), and DBD Jet (L).

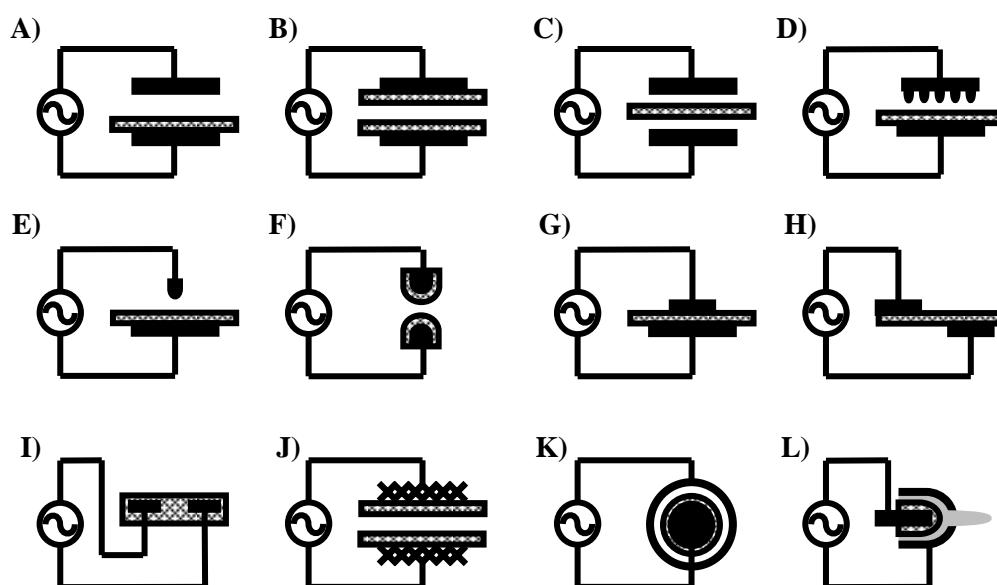


**Figure 1.1:** The collection of different typical configurations of DBD.

The applications of the plasma technology based on the DBD are being considered in many industrial areas. The DBD based applications such as ozone synthesis, surface treatment, pollution control, excimer, flow control, and biomedical application will be discussed in the following sub sections. Other applications of DBD include high

intensity of CO<sub>2</sub> laser, reforming of methane (Goujard, Tatibouet, & Batiot-Dupeyrat, 2011), and dust removal (Atten, Pang, & Reboud, 2009).

### **1.2.1 The ozone generator**

The DBD based ozonizer has a long history in the industry. The typical arrangement of the DBD based ozonizer is in cylindrical geometry (refer to Figure 1.1, labeled as K). The inner electrode is covered by a Pyrex glass tube and connected to a high-voltage supply. Formation of ozone is due to the reaction between the oxygen radicals and oxygen molecules (Eliasson, et al., 1987; Kogelschatz, et al., 1999). One of the common applications of ozone is for the drinking water treatment (Siddiqui, Amy, & Murphy, 1997). Recently, the ozone is extensively used in food industry and odor removal. The ozone generated from DBD reactor can also be used for color removal of a textile waste (Ramasamy, Rahman, & Wong, 2001).

### **1.2.2 Surface treatment**

The DBD has also been used in the surface treatment of material (Wagner, et al., 2003). The advantages of DBD in surface treatment are the flexibility of DBD geometrical and the ability to be operated under atmospheric pressure. Surface treatment by DBD includes the modification of the polymer surface (Esen, et al., 2005; Kwon, Myung, Lee, & Choi, 2006; Kwon, Tang, Myung, Lu, & Choi, 2005; Massines, Gouda, Gherardi, Duran, & Croquesel, 2001; Zhang, Shao, Long, et al., 2010) and cleaning (Kersten, Steffen, & Behnke, 1996; Yi, Lee, & Yeom, 2003).

Borcia studied the effect of various polymer films treated by DBD. The results showed that the surface hydrophilicity can be improved due to the surface oxidation. In further explanation, the molecular oxygen in the atmospheric air is excited by the DBD which can be rapidly reacted with the treated surface to increase the surface hydrophilicity (Borcia, Anderson, & Brown, 2004).

Massines reported a comparison of the filamentary discharge and homogenous discharge for surface modification in 1998 (Massines & Gouda, 1998). Massines reported that both types of the discharge can enhance the hydrophilicity effect. However, the homogenous discharge brings a better result in the hydrophilicity effect.

The DBD filaments are randomly distributed to cover the treated surface. Zhang investigated both the homogenous and filamentary DBD by a nanosecond unipolar pulse (Zhang, Shao, Long, et al., 2010). He reported that the surface energy is improved due to the physical etching and introduction of oxygen-containing polar functional groups. However, the surface energy improvement has the ageing effect. It is attributed to the reorientation of the polar chemical groups.

A summary of surface treatment by DBD is given by Wagner as shown in Figure 1.2 (Wagner, et al., 2003).

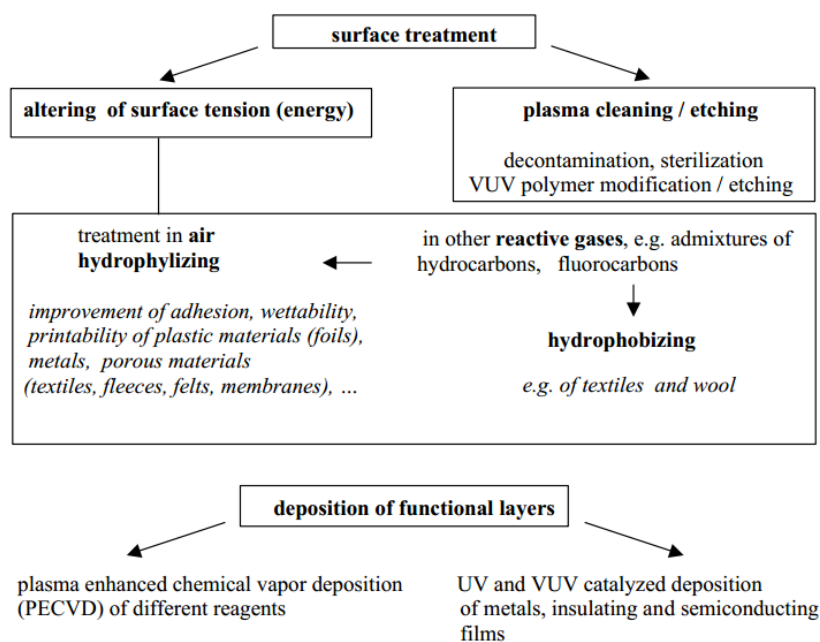


**Figure 1.2:** Surface treatment and layer deposition by DBD (Wagner, et al., 2003).

The high hydrophilic effect enhances the wettability, printability, and adhesion on the polymer surface. Besides, the DBD treatment can also increase the hydrophobic effect on the treated Polypropylene film by using Helium/CF<sub>4</sub> DBD as evidenced by an increased contact angle (De Geyter, et al., 2008).

### 1.2.3 Pollution control

In the DBD formation, electrons are accelerated and collided with molecules thus creating a large number of free radicals. The DBD reactor behaves like a chemical reactor, which contains of a large variety of reactions. The reaction inside the DBD involves the free radicals, molecular, ions and electrons. The removal of common gaseous pollutant such as nitrogen and sulfur oxides was studied by Hashim and Wong (Hashim, Wong, Abas, & Dahlan, 2007; Wong, Hashim, Abas, & Dahlan, 2010). Besides, Xia studied the removal of ammonia by the DBD. He reported the potential application of the DBD for removing odor causing gas from the gas streams (Xia, et al., 2008).

Manojlovic compared the efficiency of ozonation and direct treatment of pollutants by DBD. The results showed that the direct DBD treatment had higher efficiency for removing arsenic (Manojlovic, et al., 2008). Furthermore, the decomposition of volatile organic compounds (VOCs), NH<sub>3</sub>, H<sub>2</sub>S and CO<sub>2</sub> by DBD was reported by Kogelschatz in literature (Kogelschatz, et al., 1999).

#### **1.2.4 Extreme ultraviolet excimer, ultraviolet excimer and plasma fluorescent lamp**

The UV radiation can be emitted by a DBD operated with appropriate gas mixture such as Ar<sup>2\*</sup>, Kr<sup>2\*</sup>, Xe<sup>2\*</sup>, ArCl\*, KrCl\*, and XeCl\* (Kogelschatz, 1990). The DBD operating with halogen gas, such as Cl and Br, is also an alternative method to produce UV radiation (Lomaev et al., 2006). A DBD based excimer can have the configuration in the form of wire mesh (Wang et al., 2006), coplanar electrodes or making use of the transparent indium-tin oxide (ITO) conductor as one of the electrodes. On the other hand, the DBD based neon excimer lamp can be used for generating extreme ultraviolet (EUV) (Carman, Kane, & Ward, 2010). Moreover, mercury free fluorescent and the plasma display are based on the concept of the conversion of DBD's UV emission to visible light by a phosphor layer.

#### **1.2.5 Flow control**

The potential of flow control by DBD had been studied by Enlo (Enloe, McHarg, & McLaughlin, 2008) and Lagmich (Lagmich, Callegari, Pitchford, & Boeuf, 2008). Commonly, the DBD flow controller is arranged in actuator configuration. The DBD flow controller is also referred as electrohydrodynamic (EHD) actuators. The advantages of this DBD actuator are the small size of the device, the absence of

mechanical parts, reduced drag, robustness, simplicity and low power consumption while allowing real time control (Moreau, 2007).

The DBD actuator can generate the charge particles in the surrounding air. Due to the existing of electromagnetic force on the dielectric surface of the actuator, the charge particles can be accelerated to produce a zero net mass flux over the dielectric surface. The flow induced by the DBD actuator is known as ionic wind. The velocity of the ionic wind can reach a velocity of  $8 \text{ ms}^{-1}$  at 0.5 mm above the dielectric surface (Moreau, 2007).

### **1.2.6 Biomedical application**

During the last decade, plasma based biomedical application has been rapidly developed. Biomedical application such as skin diseases treatment (Fridman, et al., 2007), blood coagulation (Fridman, et al., 2006), and sterilization (Tanino, Xilu, Takashima, Katsura, & Mizuno, 2007; Xu, et al., 2009) have been studied. The DBD configurations such as the plasma jets (Kolb, et al., 2008; Xu, et al., 2009), floating electrode (FE DBD) (Fridman, et al., 2006; Fridman, et al., 2007), and surface DBD (SDBD) (Weltmann, et al., 2010), can be used for generating the low temperature plasma for medical application.

Treatment with low-temperature plasma enhances the speed of blood coagulates without any tissue damage while simulating tissue regeneration effect (Fridman, et al., 2006). Possibility of infection of wound is also reduced with the treatment (Fridman, et al., 2006; Tanino, et al., 2007; Xu, et al., 2009).

Nevertheless, medical risk of plasma treatment like the toxicity of DBD treatment on endothelial cells was studied (Kalghatgi, Fridman, Fridman, Friedman, & Clyne, 2008). The author compared the difference of the duration of the DBD treatment. The report suggested that the short-duration DBD treatment results in non-toxic effect to the endothelial cell. Short duration of DBD treatment for endothelial cells enhances the cell proliferation, which increases the tissue regeneration effect. However, the cytotoxic effect of the endothelial cell may occur after a long duration of the DBD treatment.

## **1.3 Research and Development**

### **1.3.1 Introduction**

The DBD mechanism is developed based on the evidence of the experimental investigations. The plasma diagnostic techniques employed in the investigation of DBD discharges include electrical measurements (voltage, discharge current and charge flow), spectroscopy, and high speed imaging technique. In this section, the research and development on DBD in the literature is reviewed.

### **1.3.2 The DBD discharge modes**

The homogenous mode and filamentary mode of DBD can be easily distinguished, where filamentary discharge is generated in a numerous filament form, and homogenous discharge is a uniform discharge covering the electrode. These different discharge modes produce different current waveforms. A homogenous discharge in nitrogen feeding gas is shown in the left-hand side of Figure 1.3, labeled as (a). This kind of discharge has been defined as homogenous discharge, or Townsend-like discharge (Massines, Gherardi, Naude, & Segur, 2005; Luo et al., 2007) where the current signal

is a single long duration non-impulsive current waveform in a range of few  $\mu\text{s}$ . In the case of filamentary discharge mode as shown in the right hand side of Figure 1.3, labeled as (b), the current waveform consists of a large number of extremely short current pulses each with a duration in the range of a few ns or shorter. The amplitude of the impulsive current in filamentary discharge is higher than that in a homogenous discharge. Massines suggested that each discharge streamer was corresponding to a single current pulse.

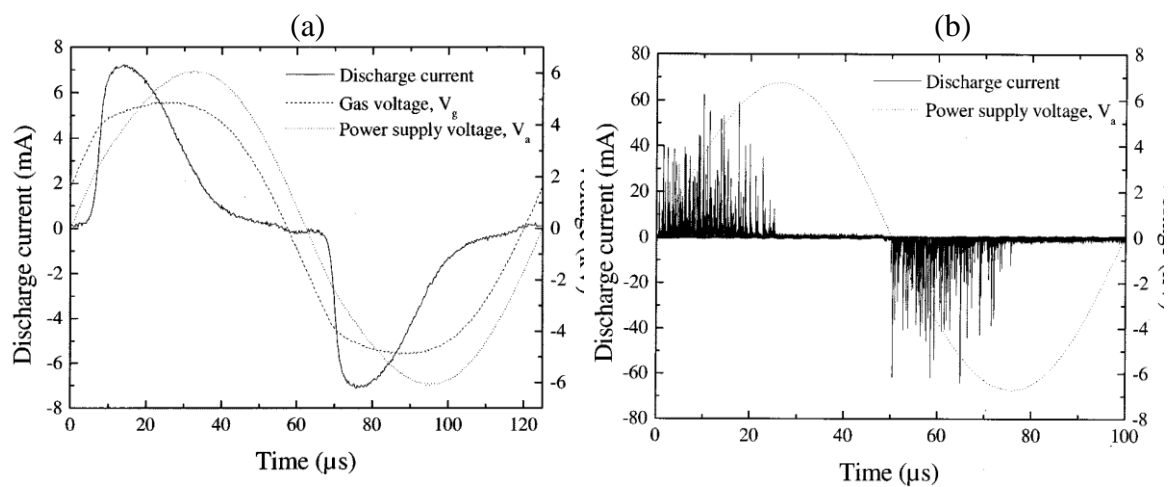


**Figure 1.3:** The comparison of the current measurement between the homogenous discharges in left hand side, labeled as (a) with the filamentary discharge in right hand side labeled as (b) (Gherardi & Massines, 2001).

The third mode of discharge is the mix mode (Petit, Jidenko, Goldman, Goldman, & Borra, 2002). This type of discharge consists of both homogenous and filamentary mode, which is also termed as transient discharge or mix-discharge.

Petit investigated the electrical characterization of the mix-discharge using a numerical analysis by Matlab software. He observed a long-duration non-impulsive current (pseudocontinuous current) overlapping with the impulsive current as shown in Figure 1.4 (Petit, et al., 2002). The author believes that this current is not caused by the



capacitive current, which is due to the variation of the voltage between the capacitor. Petit suggested that the non-impulsive is caused by the overlapping homogenous discharge in filamentary discharge.

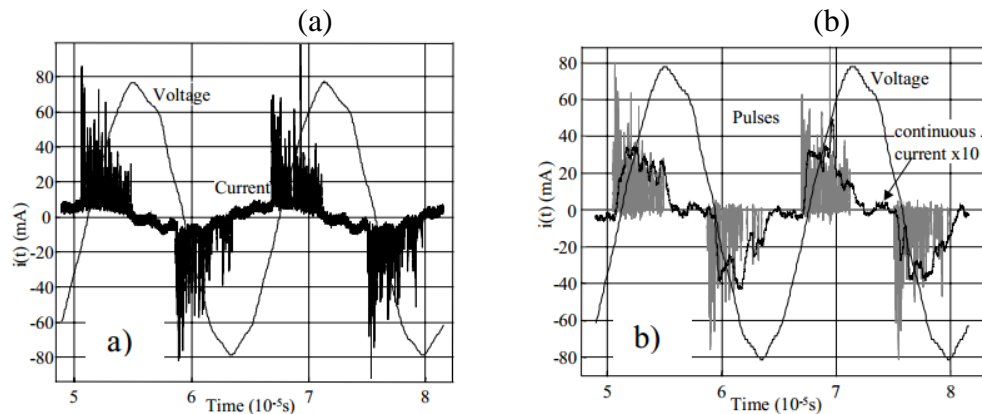


**Figure 1.4:** (a) The mix-discharge mode where the discharge current is due to combination of homogeneous discharge current and filamentary current pulses. (b) The two components are shown separated (Jidenko, et al., 2002).

For the mix-discharge mode, the measured current consists of three components after eliminating the background noise (Petit, et al., 2002). The first component is the capacitive current caused by the alternating applied voltage on the DBD reactor. The second component is the impulsive current associated with the DBD. The third component is the non-impulsive current. The second and third components are present only when the DBD is ON. Beside Petit report, the non-impulsive current in filamentary discharge is also observed by Jidenko and Laurentie (Jidenko, Petit, & Borra, 2006; Laurentie, Jolibois, & Moreau, 2009).

### **1.3.3 Investigation of the filamentary current**

The impulsive current is highly unstable in the filamentary DBD discharge. Van Brunt developed a statistical analysis method for the data treatment of the impulsive current amplitude, charges per pulse, duration of pulse, time separation between consecutive pulses (Vanbrunt & Cernyar, 1991; Vanbrunt, Cernyar, & Vonglahn, 1993). It was believed that the memory effect played an important role in the pulse height distribution and the time separation between the pulses (Vanbrunt, Misakian, Kulkarni, & Lakdawala, 1991). The effect of discharge time on the pulse height distribution was later studied (Vanbrunt, Vonglahn, & Las, 1995). Vanbrunt also suggested that the dielectric surface properties strongly influenced the characteristic of the pulse height distribution (Vanbrunt, Vonglahn, & Las, 1995). Wang also suggested that the dielectric surface properties are modified by the discharge (Wang et al., 2006).

In a separate study, Reichen reported on a detailed study of the influence of the gas velocity based on the pulse height distribution (Reichen, Sonnenfeld, & von Rohr, 2010).

Gulski analyzed the discharge statistical pattern for different DBD geometry by several statistical methods such as skewness, kurtosis and modified cross correlation (Gulski & Kreuger, 1990). He observed that the DBD geometry affect the discharge statistical pattern.

The calculation of the average amplitude of the impulsive current is one of analysis performed. From the investigation of the average impulsive current amplitude, Jidenko observed that there were two different regimes found in the impulsive discharge (Jidenko, et al., 2006). The regimes of the impulsive current are determined by the

applied voltage. In 2008, Siliprandi also observed the two different regimes in the discharge statistical pattern as shown in Figure 1.5. (Siliprandi, et al., 2008).

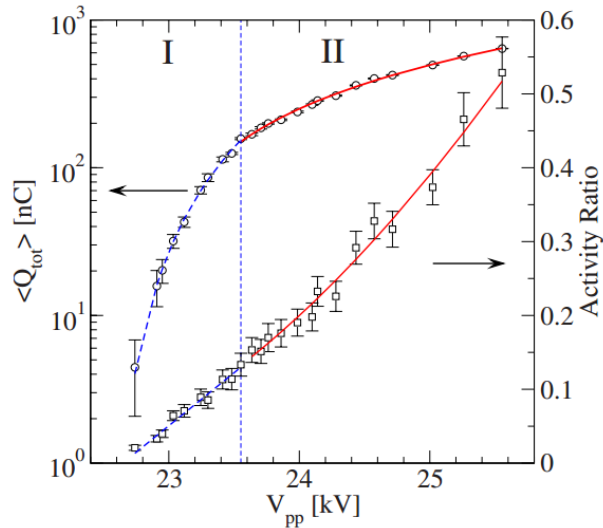


**Figure 1.5:** The existence of two regime in the discharge statistical pattern was observed by Siliprandi (Siliprandi, et al., 2008).  $\langle Q_{tot} \rangle$  is the mean total charge transferred by the discharge current. Activity ratio is the fraction of the current pulse duration to the total DBD “ON” time. The two regimes of discharge pattern are separated by 23.55 kV peak to peak applied voltage (regime transition voltage).

The average amplitude of impulsive current is increasing with the applied voltage until the applied voltage reaches the regime transition voltage. In regime 2, the average discharge current pulse is slowly increased with the applied voltage (Jidenko, et al., 2006).

The impulsive currents are fluctuating stochastically, both spatially and temporally. Hence the analysis of the stochastic nature of the impulsive currents is a time consuming process. Ficker simplified the impulsive current analysis process by a digital acquisition method (Ficker, Macur, Pazdera, Kliment, & Filip, 2001). In his experiment, only the pulse amplitude and the pulse occurring time are recorded in the digital

acquisition. The charge transfer of each impulsive current can be estimated from the amplitude of the impulsive current. This method is used to reduce the data analysis time and the size of the stored data.

The probability density function of the amplitude of impulsive current was also investigated by Ficker experimentally (Ficker, 2003).

### 1.3.4 General investigation of the filamentary discharge

The technique of measuring the total charge transported via a capacitor connected in series with DBD reactor has been introduced in 1943 (Manley, 1943). The total charge transfer was determined by dividing the measured voltage across the capacitor by its capacitance. The well-known Manley's equation can be employed to estimate the energy dissipation in a uniformly distributed filamentary discharge of DBD. This equation can be obtained from the parallelogram in the QV Lissajous figure as shown in the right hand side of Figure 1.6, labeled as (b). (Falkenstein & Coogan, 1997; Wagner et al., 2003).

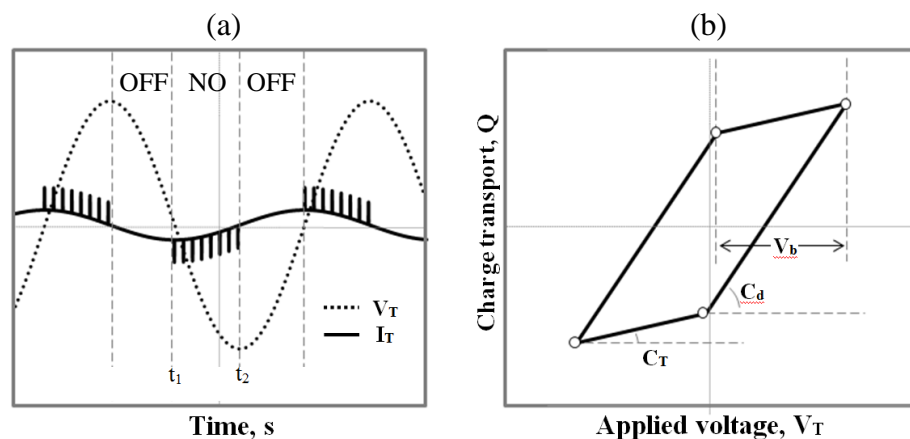


**Figure 1.6:** (a) Schematic diagram of the voltage and current waveform versus time. (b) Schematic diagram of voltage to charge Lissajous figure.

The DBD operating period can be divided into DBD “ON” and DBD “OFF” modes. The DBD “ON” mode is the period from the first current pulse  $t_1$  until the last current pulse  $t_2$  in a single current burst. The DBD “OFF” mode indicates the period of zero DBD current pulse between two current bursts. In the DBD “OFF” mode,  $dQ/dV_T$  is equal to the equivalent capacitance of the DBD reactor ( $C_T$ ), which is the slope obtained in Figure 1.6(b). After the discharge is ignited, a larger number of impulsive currents superposition with background displacement current is observed in the DBD “ON” period as shown in Figure 1.6(a). The effective capacitance of the DBD reactor is then changed to dielectric capacitance ( $C_d$ ).

The breakdown voltage ( $V_b$ ) is the minimum required applied voltage for igniting the DBD. The voltage across the DBD reactor includes the voltage across the space gap and the dielectric. Therefore, the space gap breakdown voltage  $V_g$  can be expressed by:

$$V_g = \frac{V_b}{2} \left( \frac{C_d}{C_d + C_g} \right) \quad (1.1)$$

During DBD “ON” mode, the space gap voltage remained constant and equal to the breakdown voltage of the space gap.

The energy dissipated per cycle can also be derived from the QV Lissajous figure, considering the area under the curve of QV Lissajous figure.

$$E = \oint v(t) dq \quad (1.2)$$

The estimated energy can also be expressed in a simplified form:

$$E = V_b(V_{T,pp} - V_b)(C_d - C_T) \quad (1.3)$$

$V_b$  is the breakdown voltage measured from QV Lissajous as shown in Figure 1.6(a).

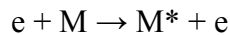
$V_{T,pp}$  is the peak to peak voltage applied across the DBD reactor.

### 1.3.5 The optical emission spectroscopy

The optical emission spectrum can be used for investigating the DBD discharge. From the discharge emission spectrum, the discharge species and metastable density can be deduced from their characteristic wavelength emission.

Massines studied the DBD discharge by the optical investigation method ( Massines, et al., 2003; Massines, et al., 2009). From their experimental result as shown in Figure 1.7, they suggested that the DBD formation is affected by the density of the  $N_2(A^3\Sigma_u^+)$  metastable molecules. The metastable molecules are mainly contributed by the penning ionization. The density of the  $N_2(A^3\Sigma_u^+)$  metastable molecules in homogenous discharge was found to be much higher than that obtained with filament discharge.

The ionization of the gas in DBD can occur in two different processes which are direct ionization and Penning ionization (Massines, et al., 2009). The Penning ionization is a two-step process:



M is the molecules.  $M^*$  is the metastable molecules. The ionization can be slowed down by the Penning ionization which results in lower ion density of Townsend discharges (Massines, et al., 2009). Direct ionization is dominant in the filamentary discharge. This will produce higher density of the ions in filamentary discharge.

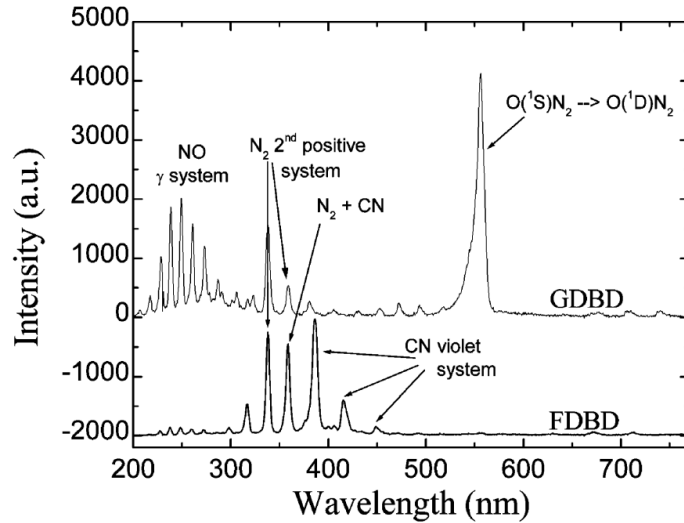


**Figure 1.7:** Emission spectra of  $N_2$  in the homogenous discharge (GDBD) and filamentary discharge (FDBD). The  $(ON_2)$  emission intensity is representative of the  $N_2(A^3\Sigma_u^+)$  metastable density. The  $(ON_2)$  emission is only observed in homogenous discharge (Massines, et al., 2003).

In the optical investigation studies of Kozlov, the author showed that the first light emission was detected at the anode at the beginning, which was caused by the pre-breakdown phase. The pre-breakdown phase is due to small amount of electron progresses and accumulated near to the anode (Kozlov, et al., 2005). In this report, the author showed that the cathode streamers are accelerated to the cathode with an exponentially increasing velocity. The relative intensity of light is shown in the Figure 1.8.

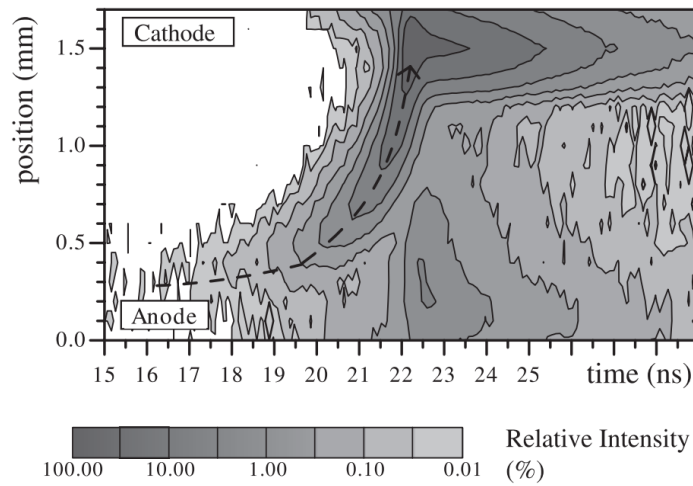


**Figure 1.8:** The contour of the relative intensity shows the velocity of ion streamer increases with the distance from anode (Kozlov, et al., 2005).

The author suggested that there were three different phases of the microdischarge formation (Kozlov, et al., 2001). The first phase is the pre-breakdown phase, which is the avalanche of the electrons to anode. The second phase is the propagation of the ions to cathode. In this second phase, the first maximum intensity light was observed near the cathode. The second maximum intensity light was then obtained near to the anode as shown in Figure 1.8. For the third decay phase, the charge accumulated on the dielectric surface, which reduced the local electric field, results in the decay of the discharge.

In 2010, Hoder studied the spectroscopy of filamentary discharges in three different DBD arrangements (Hoder, et al., 2010). The three different arrangements of DBD reactor are shown in Figure 1.9.



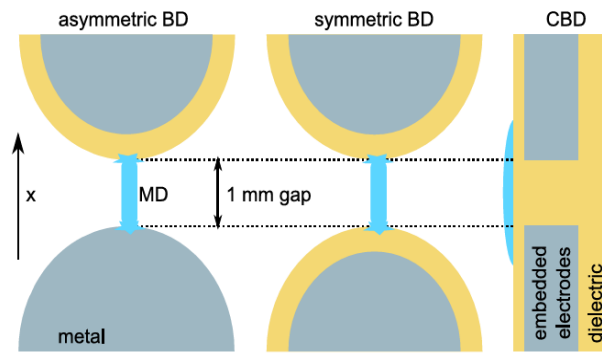


**Figure 1.9:** The three different DBD arrangements studied by Hoder (Hoder, et al., 2010).

In the report, the arrangement of the dielectric cathode (D-) and metal anode (M+) resulted in a shorter pre-breakdown Townsend phase. It is caused by the secondary emission of the dielectric cathode providing a sufficient electron density to enhance the filamentary discharge in shorter time. However, the arrangement of the metal cathode (M-) and dielectric anode (D+) gave a longer pre-breakdown phase, which allows sufficient electron density to build up for the formation of cathode directed ionizing wave. The ion velocity of the M-D+ arrangement is lowest and the time duration of the decay phase of the M+D- arrangement is the longest one.

## 1.4 DBD Modeling

### 1.4.1 Introduction of electrical modeling of DBD

DBD modeling can be classified into physical modeling and electrical modeling. Electrical modeling is the modeling by constructing an electrical circuit to characterize the overall discharge behavior of the DBD. The electrical modeling can be used to predict the external quantities such as external current and voltage. On the other hand, the physical modeling is based on theoretical model such as the ionization and fluid models. The physical modeling is commonly used to predict the interaction phenomena between the electrons, ions and molecules in the discharge.

In 2001, Lui and Neiger derived a set of the electrical dynamic equations for the DBD electrical modeling (Liu & Neiger, 2001). In fact, the Lui and Neiger dynamic equations can be employed in both filamentary and homogenous discharge. In 2004, Bhosle constructed another filamentary discharge electrical model, which took into consideration the discrete volume of the individual microdischarge channels (Bhosle, et al., 2004). Bhosle suggested a varying conductance switch to replace the space gap circuit in the DBD modeling. Barrientos (Valdivia-Barrientos, Pacheco-Sotelo, Pacheco-Pacheco, Benitez-Read, & Lopez-Callejas, 2006) also proposed another filamentary discharge model in 2006. For the Barrientos model, the DBD discharge behaves as an electrical circuit, which consists of a high frequency sinusoidal current source coupled with a resistor in parallel. Zhang reported that the Barrientos model can be used for simulating the overall dynamic behavior of filamentary discharge in 2010 (Zhang, Shao, Yu, et al., 2010). Zhang's report showed a good comparison with the experimental results under atmospheric air and 50 Hz power frequency. In 2009, Pal simulated the filamentary discharge by a resistor and a capacitor connected in series

(Pal, et al., 2009). The DBD “ON/OFF” is controlled by a virtual switch, which could be used to generate a single impulsive current waveform.

For the homogenous discharge electrical modeling, the DBD current can be modelled as a non-linear function of the space gap voltage (Chen, 2003; Flores-Fuentes, et al., 2009; Massines, et al., 2003; Naude, Cambronner, Gherardi, & Massines, 2005).

### 1.4.2 Basic concept of the DBD electrical modeling

To simulate the electrical dynamic of DBD reactor, the electrical circuit used to represent the DBD discharge in the reactor is as shown in Figure 1.10.

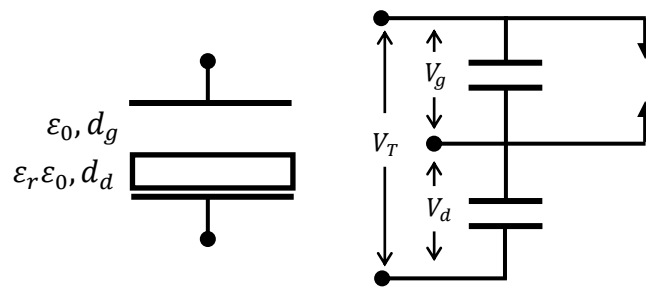


**Figure 1.10:** The single dielectric DBD reactor can be represented by the simplest equivalent electric circuit.

A case of single dielectric layer is used in this example. If the space gap voltage is smaller than the breakdown space gap voltage, the DBD is “OFF” and the DBD behaves like a combination of two capacitors connected in series. The total capacitance  $C_T$  can be calculated by the combination of two capacitors.

If the applied voltage overcomes the breakdown voltage for DBD discharge, the DBD turns into DBD “ON” mode and the current will be transferred via every ignited microdischarge channel. The microdischarge is distributed to cover the DBD electrode uniformly (Eliasson, et al., 1987; Eliasson & Kogelschatz, 1991). If the space gap voltage overcomes the breakdown voltage, the space gap behaves like a conducting layer. The induced discharge current during DBD “ON” mode is measurable. The DBD is turn to “OFF” mode when the applied voltage starts to decrease. The DBD is “ON” again when the space gap voltage overcomes the breakdown voltage in the next half cycle.

However, the conductivity of the space gap during the DBD “ON” mode is difficult to estimate. Due to instability behavior of the filamentary discharge, the construction of the electrical model of filamentary discharges is much more difficult if compared to the homogenous discharge. The review of different electric models for the filamentary discharge will be presented accordingly in the following sub-sections.

### **1.4.3 Lui and Neiger model**

The detailed dynamic electric equation set was derived for the condition under a unipolar square pulses (Liu & Neiger, 2001) and an arbitrary excitation voltage (Liu & Neiger, 2003). The dynamic electric equations show the general relation between the discharge current and the measured current. The measured current is also referred to as the external current. Lui and Neiger assumed that the measured current is smaller than the true DBD current by a factor. Besides, they also suggested that the space gap capacitance can be assumed to be constant during the DBD “ON” and DBD “OFF” mode.

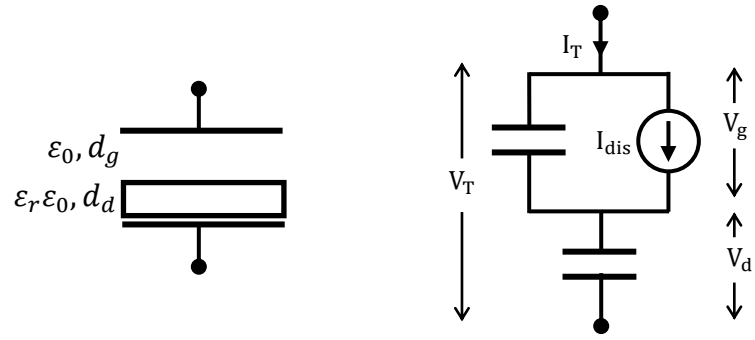


**Figure 1.11:** The dynamic electric circuit of the DBD reactor in Lui and Neiger model (Liu & Neiger, 2001, 2003).

The dynamic electric circuit as shown in Figure 1.11 represents the DBD reactor. The true discharge current in the discharge gap can be calculated from the measured current by using equation (1.4).

$$I_{dis} = C_g \frac{dV_T}{dt} + \frac{C_d + C_g}{C_d} I_T \quad (1.4)$$

$V_T$  is the applied voltage.  $C_d$  and  $C_g$  are the capacitance of the dielectric and space gap respectively.  $C_T$  is the total equivalent capacitance of the DBD reactor. If the initial charge on  $C_d$  is  $Q_d(0)$ , the deposited charge from the previous discharge, then the dielectric voltage can be expressed as:

$$V_d(t) = \frac{1}{C_d} \int_0^t I_T(t) dt + \frac{Q_d(0)}{C_d} \quad (1.5)$$

The instantaneous power consumption of the DBD is obtained by this expression:

$$P_{DBD} = V_g(t) I_{dis}(t) \quad (1.6)$$

where  $V_g$  is the space gap voltage. These equations can be used for determining other electrical quantities such as the space gap voltage, dielectric voltage, true discharge current, and DBD power consumption.

#### 1.4.4 Bhosle discrete volume model

Bhosle proposed a discrete electrical model for filamentary discharge in 2004 (Bhosle, et al., 2004). This model considered the multidischarge channels in discrete volume. The non-discharge region of the DBD has also been taken into consideration. The number of the microdischarge channels is functioned and varied during the DBD “ON” mode. In Bhosle's model, the microdischarge channel is assumed to breakdown individually and not interacting with each other.

Before combining all the microdischarge channels, the single microdischarge channel in DBD reactor was first considered. Bhosle suggested the individual microdischarge channel behaved as a time varying conductor with conductance  $G$  and the discharge fully occupying the small discrete volume. Then, each occupied volume of the microdischarge channel contributes to the capacitance for each channel. The capacitance of the single microdischarge was first determined based on the occupied area and the DBD geometry.

For plate-to-plate geometry, the total equivalent capacitance of DBD reactor,  $C_T$  can be expressed as:

$$C_T = \frac{\epsilon_r \epsilon_0 S_T}{d_d + \epsilon_r d_g} \quad (1.7)$$

where,  $\epsilon_0$  is the permittivity of vacuum, and  $\epsilon_r$  is the relative permittivity of the dielectric.

The dielectric capacitance,  $C_{d,f}$  of the single microdischarge channel can be expressed as:

$$C_{d,f} = C_d \frac{S_f}{S_T} \quad (1.8)$$

$$C_{T,f} = C_T \frac{S_f}{S_T}$$

where,  $S_f$  is the area occupied by a single microdischarge channel.  $S_T$  is the total area of the electrode.  $C_d$  is the total dielectric capacitance.  $C_{T,f}$  is the total effective capacitance of single microdischarge.

The conductance  $G$  is first estimated from the experimental result. In the single channel electrical modeling, the Triac switch is triggered by the space gap voltage. After the ignition of the discharge, the conductance of the space gap is varied according to the experimental conductance  $G$ .

The simplified Bhosle model, which combines all the microdischarge channels, is shown in Figure 1.12. The total effective conductance of overall DBD discharge is the product of the number of channels each with a single channel conductance  $G$ . The dynamic equivalent circuit is then varied according to the number of ignited channels during the DBD “ON” mode.

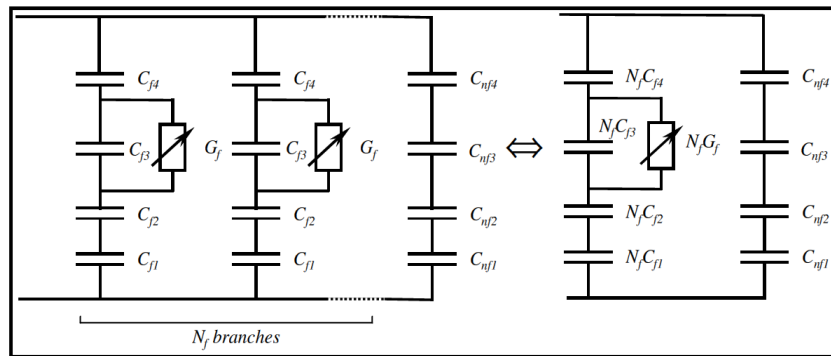


**Figure 1.12:** The equivalent circuit for  $N_f$  filaments (Bhosle, et al., 2004).

$N_f$  identical microdischarge channels are generated to cover the DBD reactor. The equivalent capacitance of the non-discharge region can be calculated by the following expression:

$$C_{T,N} = C_T - N_f C_{T,f} \quad (1.9)$$

Bhosle suggested that the number of the ignited microdischarge channels during the DBD "ON" mode can be determined by a product of two functions expressed as:

$$N_f = H(V_g)\alpha(V_g) \quad (1.10)$$

$H(V_g)$  is the hysteresis phenomenon which is either 0 or 1.  $\alpha(V_g)$  is the number of the ignited channel which is a function of the space voltage,  $V_g$ .

#### 1.4.5: Barrientos model

In 2006, Barrientos proposed another filamentary discharge model (Valdivia-Barrientos, et al., 2006). This model considered the DBD reactor geometry and dielectric materials. Barrientos used a semi-empirical relation for predicting the breakdown voltage. The space gap breakdown voltage is given as a function of the applied voltage frequency,  $f$  as expressed below:

$$V_{g,b} = \frac{1.4\left(\frac{C_d}{C_g}\right)^2}{\ln(f)} \quad (1.11)$$

The lower breakdown voltage for a high frequency discharge is attributed to the existence of memory voltage. It was suggested that the frequency had significant effect on the memory voltage. The deposited memory voltage may reduce the breakdown voltage of the discharge.



Instead of using the varying resistor or conductor to characterize the microdischarge, Barrientos used a high frequency current generator to simulate the overall DBD discharge current. The amplitude of the current is a linear function of the rate of change of the applied voltage,  $dv/dt$ .

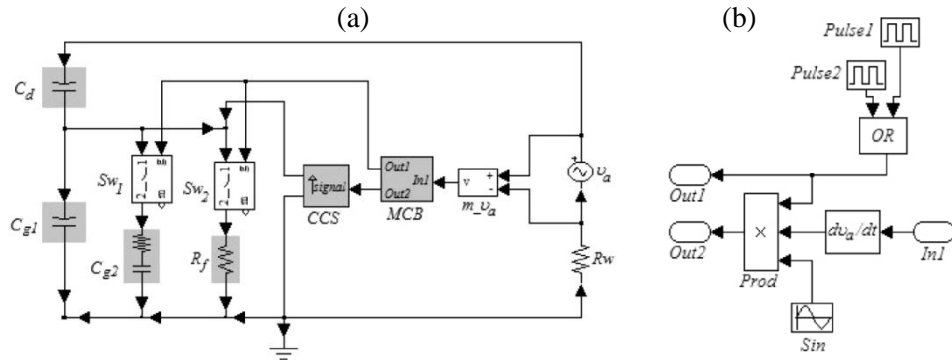


**Figure 1.13:** Barrientos' Model implemented in Matlab Simulink software. (a) The general electrical circuit. (b) The coding block of MCB.

The “Sin” block in Figure 1.13 (b) is the sinusoidal waveform generator, which represents the overall DBD current waveform. The amplitude of the sinusoidal waveform current is a linear function of the rate of change of the applied voltage,  $dv/dt$ . Pulse 1 and pulse 2 are used for triggering the DBD “ON” mode for positive and negative cycle respectively. The possible variable space gap capacitance is taken into consideration. The variation of the space gap capacitance is due to the ionization of the operating gas. The switch  $Sw_1$  is used for controlling the variation of the space gap capacitance. The switch  $Sw_1$  is closed during the DBD “OFF” mode. The total effective space gap capacitance is equal to  $C_{g1} + C_{g2}$ , when the  $Sw_1$  is closed. When the DBD is ON, the  $Sw_1$  is triggered to be an open circuit. This will cause the total effective space gap capacitance to be reduced to only  $C_{g1}$ . Meanwhile, the switch  $Sw_2$  is used for triggering the DBD current. It is only closed when the DBD “ON” mode. The frequency of the current generator is validated with the overall experimental discharge.

In 2010, Zhang used the Barrentos model for simulating the electrical properties of DBD under atmospheric air and 50 Hz (Zhang, Shao, Yu, et al., 2010). The overall electrical properties of filamentary discharge were well simulated by this electrical circuit. However, they presented the discharge current pulses superimposed on a high frequency sinusoidal waveform, which was not observed in the experimental filamentary discharge current.

#### **1.4.6 Pal single pulse model**

In 2009, Pal proposed another electrical model for filamentary discharges (Pal, et al., 2009). This model was constructed for simulating a single impulsive current. During the DBD “ON” mode, a plasma impedance circuit was introduced for characterizing the discharge space gap. The plasma impedance consisted of a resistor in series with a capacitor. Since the capacitance and resistance were not measurable by experiment, their values were validated until a good match between the experimental and simulated results have been obtained. This electrical model was also implemented in Matlab Simulink.

#### **1.4.7 Summary of electrical models**

The DBD electrical modeling is still under development. The representative of the electrical circuit for DBD has not been unified. In summary, two approaches are commonly employed in the electrical modeling. One of the approaches is “ON/OFF” voltage dependent switch. Another approach is voltage control current source. The instability of current pulses, surface charge spreading and collection phenomena have not been taken into account by the electrical models proposed as reported in the

literature. The comparison of the proposed filamentary discharge electric models is shown in Figure 1.14. The nomenclature used in Figure 1.14 is listed in Table 1.1.

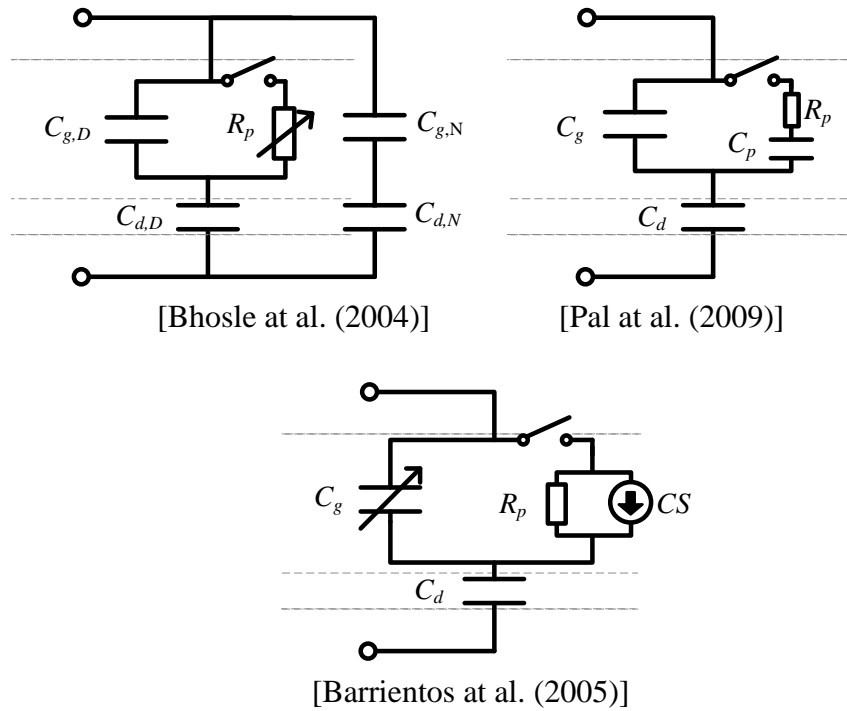


**Figure 1.14:** The comparison of the proposed filamentary discharge electric models.

**Table 1.1:** Nomenclature of electrical model

| Nomenclature | Description                                    |
|--------------|--|
| $C_g$        | Space gap capacitance                          |
| $C_d$        | Dielectric capacitance                         |
| $C_p$        | DBD capacitance                                |
| $C_{g,D}$    | Space gap capacitance of discharge region      |
| $C_{d,D}$    | Dielectric capacitance of discharge region     |
| $C_{g,N}$    | Space gap capacitance of non-discharge region  |
| $C_{d,N}$    | Dielectric capacitance of non-discharge region |
| $R_p$        | DBD resistance                                 |
| $CS$         | Current source                                 |

## **1.5 Objectives**

The objectives of this work can be summarized as following:

1. To design a dielectric barrier discharge system.
2. To study electrical characteristics of the dielectric barrier discharge.

## **1.6 Dissertation Layout**

In this chapter, the brief introduction and historical development of the DBD modeling are given. The various DBD applications and literature review of DBD are also presented in the preceding section.

Chapter 2 presents the experimental setup, diagnostic techniques, and the analysis methods.

In chapter 3, experimental results are reported. The results consist of two main parts: the statistical studies of current pulse and the energy determination of the DBD. Explanation of the experimental results and a proposed probability function are described. The proposed electrical model based on the experimental observation will be presented.

Finally, the conclusion and suggestion for future work are given in chapter 4.

# Chapter 2: Experimental Setup and Methodology

## 2.1 Experimental Setup

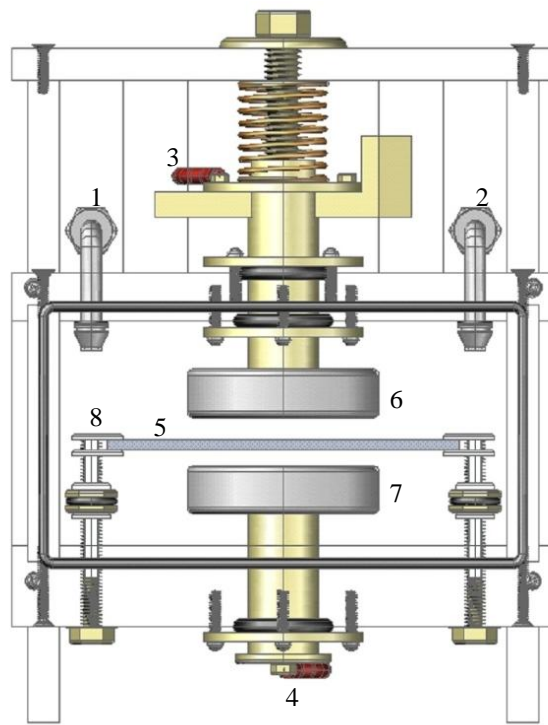
### 2.1.1 The DBD reactor

In this project, the DBD reactor consists of a pair of parallel plate electrodes, that the arrangement has been specifically designed to facilitate the variation of the space gap distance between the two electrodes. The schematics of the DBD reactor used is shown in Figure 2.1. It allows the space gap to be varied from 0.1 mm to 15.0 mm. The space gap can be fixed with the adjustable crew to be better than  $\pm 0.1$  mm error. The electrodes are two circular stainless steel plate with equal diameter 6.0 cm and thickness of 1.5 cm. Stainless steel is used for its resistance to oxidation and corrosion when exposed to ozone. The edge of the electrode is smoothed to prevent localize electric field at the edge of the electrodes. On the other hand, a silver spring had been inserted to stabilize the motion of the electrode.

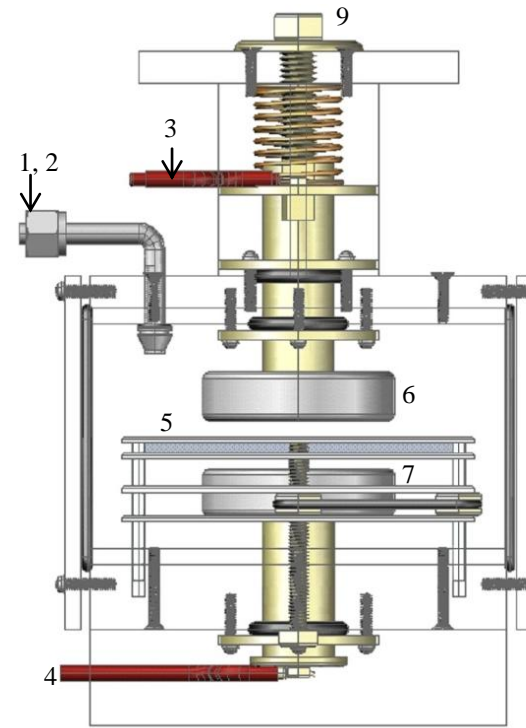
The dielectric layer is a Pyrex glass sheet with a dimension 10 cm  $\times$  10 cm and thickness of 2.0 mm. The dielectric sheet is mounted into position by using two position adjustable dielectric holders. The electrodes system is housed in a Perspex chamber. The front window of the chamber is sealed with a glass window via a square Viton ring. Emission of the visible light can be observed through the glass windows. Although the quartz window is better in spectral transmittance than glass, glass has been conveniently obtained, as they are economically available. Two ports on the top cover of the chamber are used as the gas inlet and outlet. Gas is allowed to flow freely as the DBD is operated under atmospheric pressure.

For this DBD reactor circuitry, the bottom brass rod mounted with electrode is connected to a high-voltage wire. The high-voltage probe with impedance of  $100\text{ M}\Omega$  has been inserted at the end of wire together with power supply port via a ballast resistor of  $8.8\text{ M}\Omega$ . The power supply generates a sinusoidal AC power voltage, which can reach to  $40\text{ kV}$  (pk-pk). Meanwhile, the upper electrode is connected to the ground port through the current and charge measurement circuit as shown in Figure 2.2. The equivalent current is monitored by a resistor in a range from  $100\Omega$  to  $1\text{ K}\Omega$ .

The digital oscilloscope records the measured voltage of high voltage probe and 10 times voltage probe simultaneously. In this project, two digital oscilloscopes were employed according to the required measurement. Yokogawa DL6104 oscilloscope in the bandwidth of  $1\text{ GHz}$  was used for current measurement. Tektronix 2024B oscilloscope in the bandwidth  $200\text{ MHz}$  was used for charge measurement.

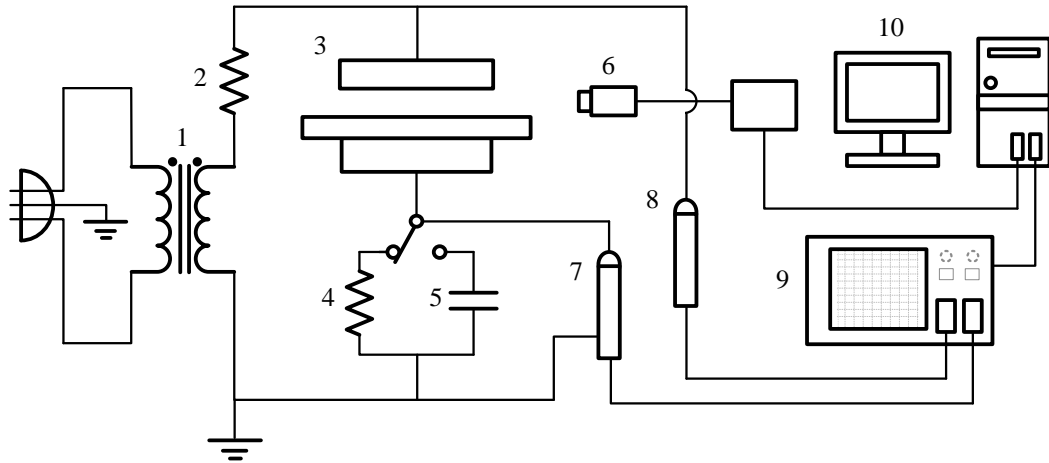


- 1 Gas inlet port
- 2 Gas outlet port
- 3 Electrical ground connection port
- 4 High voltage connection port
- 5 Dielectric sheet



- 6 Ground electrode
- 7 High voltage electrode
- 8 Dielectric holder
- 9 Space gap adjustor

**Figure 2.1:** Schematic of the DBD arrangement.



- |   |                              |    |                               |
|---|------------------------------|----|-------------------------------|
| 1 | Transformer                  | 6  | Optical emission spectroscopy |
| 2 | Ballast resistor             | 7  | 10 times voltage probe        |
| 3 | DBD reactor                  | 8  | High voltage probe            |
| 4 | Current measurement resistor | 9  | Digital oscilloscope          |
| 5 | Charge measurement capacitor | 10 | Computer interfacing          |

**Figure 2.2:** Schematic diagram of DBD experimental setup.

### 2.1.2 Power circuitry

The DBD reactor is powered by a 50 Hz AC power supply via a ballast resistor of 8.8 MΩ as shown in Figure 2.2. The power supply is made up of a step-up transformer immersed in oil and a potentiometer. The maximum voltage of this power supply is about 40 kV (pk-pk). In order to maximize the voltage across to the load, and minimize the current, the impedances bridging required,

$$Z_{Load} \gg Z_{source} \quad (2.1)$$

$Z_{source}$  is the total impedance of the source which includes its internal impedance and ballast resistance. A ballast resistor is added to limit the current and to avoid overheating of the DBD reactor.



$Z_{Load}$  is total effective impedance of the DBD reactor. The high voltage probe is placed across the DBD reactor, which reducing the total effective impedance of the DBD reactor. For the load impedance calculation, the effect of the high-voltage probe in the total effective impedance of the DBD reactor is considered. The resistance of high voltage probe,  $R_{probe}$  is about 100 M $\Omega$ . By ignoring the capacitance of high-voltage probe, the total effective impedance of the DBD reactor, which is in parallel with the high voltage probe, can be calculated by using Equation 2.2:

$$Z_{Load} = \left[ \frac{1}{R_{probe}} - \omega C_T j \right] \left[ \left( \frac{1}{R_{probe}} \right)^2 + (\omega C_T)^2 \right]^{-1} \quad (2.2)$$

$Z_{Load}$  is load impedance. It can be calculated after obtaining the capacitance of DBD reactor.  $C_T$  is total effective capacitance of DBD reactor.  $\omega$  is angular velocity of the power supply.  $j$  is the imaginary value. The load impedance depends on the space gap of DBD reactor. For instance, when the space gap is 0.2 mm, the  $|Z_{Load}|$  is 41.3 M $\Omega$ .; while for space gaps 1.0 mm, it is 61.9 M $\Omega$ . In any case, we consider the effect of space gap and make sure the impedance bridging condition is fulfilled.

## 2.2 Diagnostic Techniques

### 2.2.1 Introduction

In this project, three DBD diagnostic techniques have been used in the study of discharge characteristics. These DBD diagnostic techniques shown as following:

- a) High voltage measurement,
- b) Current measurement, and
- c) Charge measurement.

The DBD diagnostic techniques are important processes to deduce the electrical information from the DBD. In this chapter, the typical measurement techniques for the current and total charge transfer will be discussed.

### 2.2.2 High voltage measurement

The Tecktronix 6015 high-voltage probe is employed in this project for measuring the voltage across the two parallel plate electrodes. The input impedance of this high-voltage probe is about  $100\text{ M}\Omega$  ( $\pm 2\%$ ) in parallel with a capacitor of value in the range of 12 pF to 60 pF. The maximum detected voltage of this voltage probe is 40 kV (pk-pk). The live connector of the high-voltage probe is mounted at the high voltage electrode of DBD reactor, which is connected to the power supply as shown in the Figure 2.1.

### 2.2.3 Current measurement

The difficulty in the current measurement is the extremely short duration of the DBD current pulse. Each of the DBD current pulse lasts for few nanoseconds. For the current measurement, the switch as shown in Figure 2.2 is switched to the left hand-side, which is connected to a current monitor resistor. The current measurement circuit is shown in Figure 2.3. The voltage across the current monitor resistor is measured by a 10 times voltage probe and recorded by digital Yokogawa DL6104 oscilloscope with a bandwidth of 1 GHz.

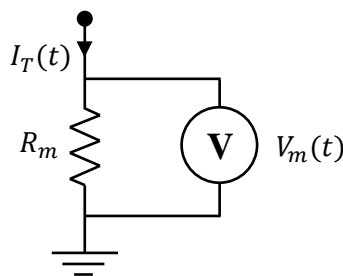


**Figure 2.3:** Resistivity current measurement circuit.

The current profile can be calculated from the voltage measured by the 10 times voltage probe as the expression below.

$$I_T(t) = \frac{V_m(t)}{R_m} \quad (2.3)$$

In our case, a 1 k $\Omega$  high frequency (low inductance) resistor is used for current measurement. The current signal is measured simultaneously with the voltage measured by high voltage probe.

#### **2.2.4 Charge measurement**

For the charge measurement, the switch as shown in Figure 2.2 is switched to the right hand-side, which is connected to a charge monitor capacitor,  $C_c$ . The experimentally measured charge transfer is a very important quantity, which can be used for the determination of the corresponding quantities. The corresponding quantities include total effective capacitance, dielectric capacitance, breakdown voltage, and total energy consumed. Generally, these quantities can be obtained from the charge versus voltage diagram. Due to the stochastic behaviors of the current waveform, the total charge transfer is measured by the charge monitor capacitor rather than the integration from the current waveform. The charge monitor capacitor is connected in series with DBD reactor as shown in Figure 2.2. The charge monitor capacitor,  $C_c$  has a value much higher than the total capacitance of the DBD reactor to minimize its effect on the electric circuit.

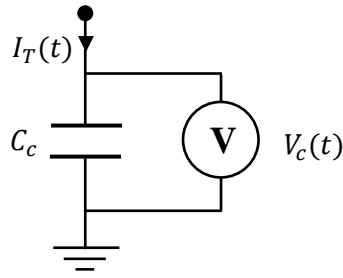


**Figure 2.4:** Charge measurement circuit.

The charge transfer is calculated from the voltage across the capacitor divided by that capacitance.

$$Q(t) = \frac{V_c(t)}{C_c} \quad (2.4)$$

$Q(t)$  is equal to charge transferred.  $V_c(t)$  is equal to voltage across the charge monitor capacitor.  $C_c$  is equal to the capacitance ( $0.47 \mu\text{F}$ ) of the charge monitor capacitor as shown in Figure 2.4.

## 2.3 Basic Discharge Characteristics and Signal Analysis Methods

### 2.3.1 Typical discharge current and voltage profiles

By using the current measurement technique and the high voltage probe, the experimental current and voltage profile is shown in Figure 2.5. The DBD “ON” and DBD “OFF” modes are observed in the current profile. The DBD “ON” mode is the duration from the time ( $t_1$ ) to time ( $t_2$ ). The time ( $t_1$ ) starts from the first DBD pulse in the half cycle. The time  $t_2$  is the last DBD pulse in the same half cycle. Meanwhile, the DBD “OFF” is the period without DBD Pulse. The minimum applied voltage can be determined from the voltage and current profile, which is indicated in Figure 2.5.

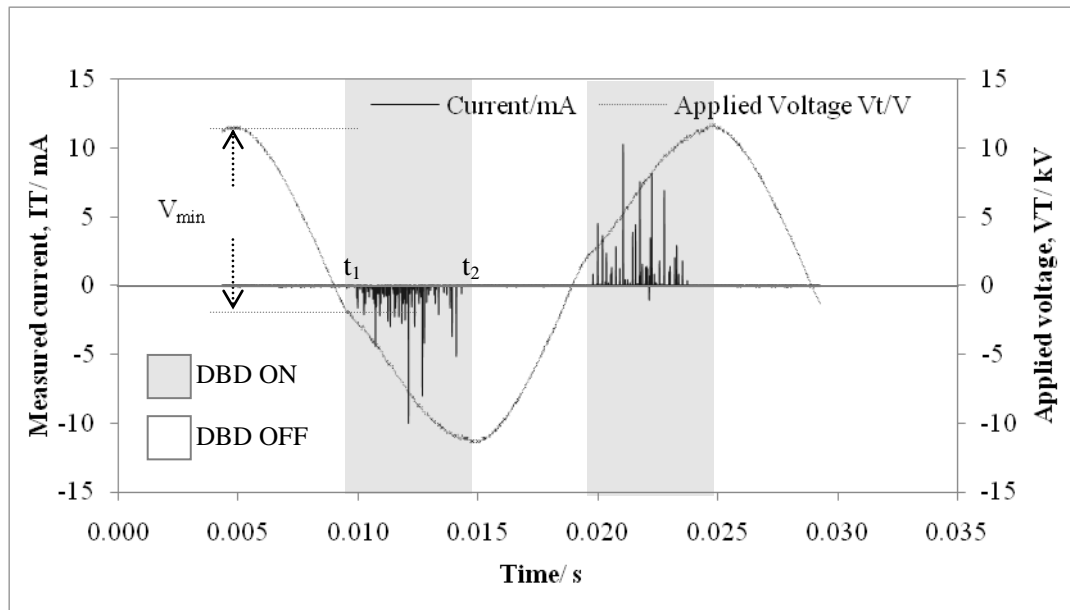


**Figure 2.5:** The typical filamentary discharge current pulse and applied voltage.

During the DBD “ON” mode, numerous current pulses are observed. Voltage distortion also occurs during the DBD “ON” mode. It is believed that the distortion is due to the decrease of the total effective impedance of the DBD reactor during the DBD “ON” mode. The effective capacitance of the reactor will be changed to the dielectric capacitance during the DBD “ON” mode (see section 2.3.9), which will reduce the total impedance of the DBD reactor, thus affecting the impedance bridging condition (see section 2.1.2).

### 2.3.2 Measured current components

The measured current,  $I_T$  is not equal to the DBD discharge current. The measured current consists of four components of the current which are overlapping together (Laurentie, Jolibois, & Moreau, 2009; Petit, et al., 2002). The four components are displacement current, background noise, impulsive current and non-impulsive current. The displacement current is due to the capacitance of the DBD electrodes when the applied voltage is time-varying. This current will only be detected significantly in a

smaller space gap (<0.5mm) since the capacitance of the electrodes in this case will be higher. The background noise is picked up by the oscilloscope. Whereas, the non-impulsive current refers to the DBD current, which has lower value and longer duration. Meanwhile, the impulsive current is the filamentary DBD current which has higher amplitude and very short time duration.

The measured current consists of both impulsive and non-impulsive discharge currents as well as the capacitance displacement current, which can be represented by the following equation:

$$I_T = I_c + I_{dect} \quad (2.5)$$

$I_T$  is the measured external total current,  $I_c$  is the displacement current,  $I_{dect}$  is the detected external DBD current in the equivalent circuit. The external DBD current is the induced DBD current flowing in the external circuit and measurable by current diagnostic. This external DBD current is not equal to the true DBD current. Only a certain ratio of the DBD charge flow is deposited on the space gap.

The detailed expression below describes the correlation between the external total current and the discharge current. The external total current composed of displacement current and DBD current as: (Liu & Neiger, 2001, 2003)

$$I_T = C_T \frac{dV_T}{dt} + \frac{C_d}{C_d + C_g} I_{dis} \quad (2.6)$$

$V_T$  is the applied voltage,  $C_d$  and  $C_g$  are the capacitances of the dielectric and space gap respectively,  $C_T$  is the total equivalent capacitance of the DBD reactor. The first term on the right-hand side is the displacement current,  $I_c$ . The second term is the detected external discharge current,  $I_{dect}$ .

### 2.3.3 Removal of the displacement current and background noise

The measured current consists of the four components. However, only the discharge current is in focus in our study. The displacement current and white noise must be removed from the current waveform before further analysis for discharge current. There are three steps to remove the two components from the measured current. The blue color waveform in Figure 2.6, labeled as (a), is the typical current signal detected by the oscilloscope.

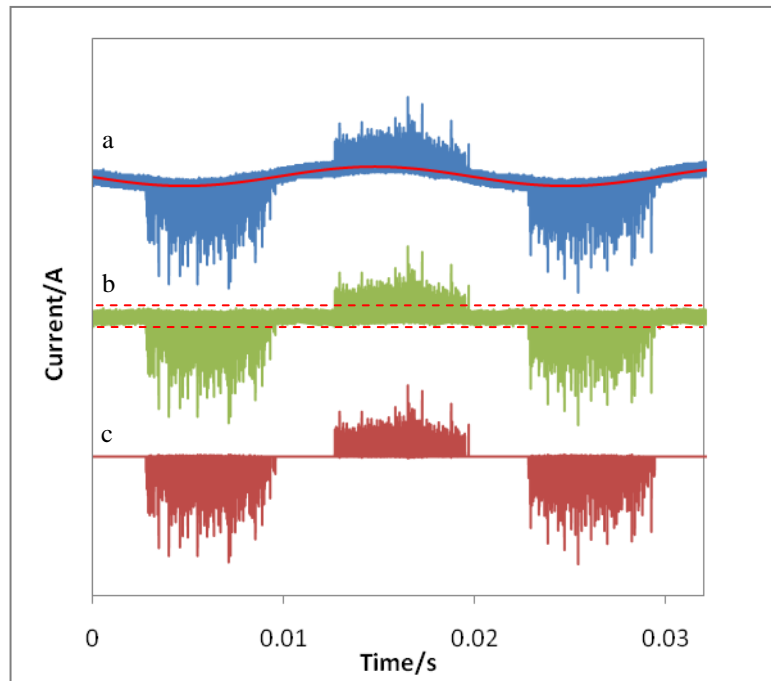


**Figure 2.6:** Step of the filamentary discharge current pulse analysis.

The first step is to remove the displacement current from the measured current. The total capacitance of the smaller gap DBD reactor is higher than the case of larger space gap. Thus, the first step is required for removing the displacement current for the small space gap configuration ( $<0.5$  mm). The capacitance of space gap can be considered as a constant magnitude during DBD “ON” mode. If the time evolution of applied voltage is assumed to be a sinusoidal waveform, the displacement current can be calculated as:

$$I_c(t) = C_T \frac{dv_T}{dt} = C_T \frac{V_{T,p}}{2\pi f} \sin(2\pi f t - \theta) \quad (2.7)$$

$V_T$  is the applied voltage,  $V_{T,p}$  is the peak voltage of applied voltage,  $f$  is the frequency of the applied voltage,  $\theta$  is the calibration phase angle.

The calculated displacement current is shown in Figure 2.6 (a) indicated as red color waveform. Before the subtraction of the displacement current, the phase angle  $\theta$  is adjusted to be equal phase with the measured capacitance current. For the large space gap distance ( $>0.5\text{mm}$ ), the displacement current is not significantly observed compared to the pulse height of DBD. After removing the displacement current, the detected DBD current  $I_{dect}(t)$  is obtained (Reichen, et al., 2010; Siliprandi, et al., 2008), which consists of the background noise as shown in Figure 2.6 (b).

The second step is to remove the background noise (Reichen, et al., 2010; Siliprandi, et al., 2008). A minimum detected value is chosen to be slightly higher than the background noise level, thus filtering the noise by the expression below:

$$I_{dect}(t) = \begin{cases} 0, & |I_{dect}(t)| < I_{limit} \\ I_{dect}(t), & |I_{dect}(t)| \geq I_{limit} \end{cases} \quad (2.8)$$

Last step is to calculate the true discharge current from the measured current. The measured discharge current is not equal to the true discharge current due to only certain amount of the discharge current flow into the external equivalent circuit. A factor  $\gamma$  introduced by Jidenko (Jidenko, et al., 2006) is the ratio of the amount of charge flowing to equivalent circuit to the total amount of DBD charge. The ratio  $\gamma$  is suggested to be equal to  $\frac{C_d}{C_d+C_g}$ , by Liu as expressed in Equation 2.9. The true discharge current is expressed as:

$$I_{dis} = \frac{C_d+C_g}{C_d} I_{det} \quad (2.9)$$



### 2.3.4 The stochastic behaviors of time separation and pulse height

After removing the displacement current and background noise, the stochastic behavior of the discharge pulse can be observed. The number of the discharge pulses can rise up to few hundred. The separation time is defined as the time difference between the consecutive current pulse. The double stochastic is observed in the non-uniform pulse height and the pulse time separation. This double stochastic of the DBD pulse is indicated diagrammatically in Figure 2.7. The pulse time separation and pulse height are marked with  $\Delta t$  and  $i$  respectively.

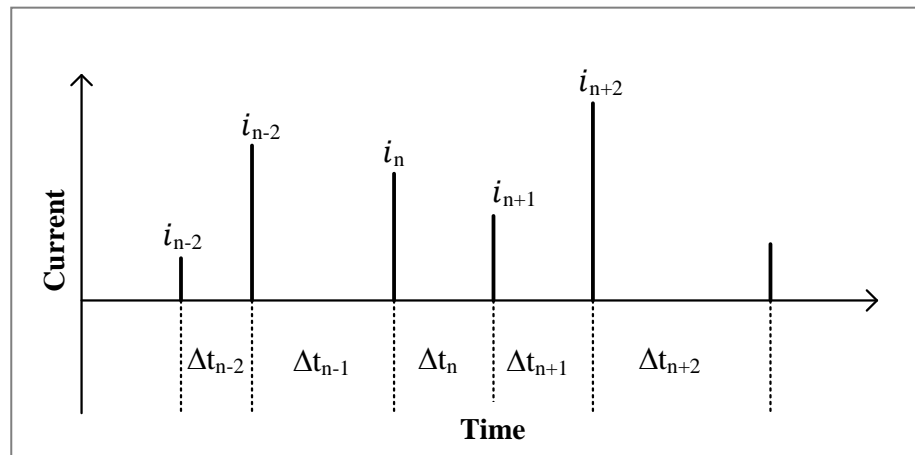


**Figure 2.7:** The diagram of the double stochastic DBD pulse.

In general, the stochastic behavior of the DBD pulses is owing to the external random process. The external random process can be attributed to the self-excitation, which is caused by the secondary emission due to bombardment with the excited species, and the photoemission from the cathode due to UV radiation (Vanbrunt, et al., 1991). The random breakdown voltage of different position is suggested as one of the stochastic characteristics and will be further discussed in the next chapter.

### 2.3.5 Temporal evolution of nanosecond pulse

Beside the overall discharge characteristics as presented in the preceding sub-section, the temporal evolution of the nanosecond pulse is also an important study in this project. Some of the internal quantities of discharge can be obtained from the temporal evolution of the single discharge pulse such as the charge transfer of the single discharge pulse and the pulse time duration. In order to detect the temporal evolution of a single impulsive current, Yokogawa DL6104 oscilloscope with a bandwidth of 1 GHz is used. A typical detected temporal evolution of current pulse is shown in Figure 2.8.

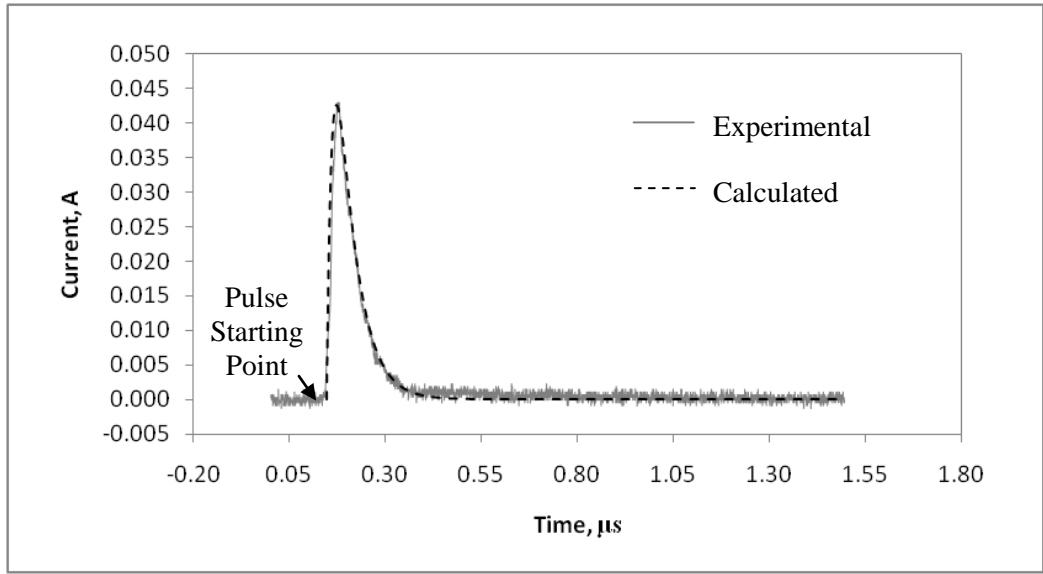


**Figure 2.8:** The detected single discharge pulse of DBD and the calculated current by Equation 2.10.

The shape of the single discharge pulse is similar to the exponential discharge pulse. The exponential discharge current pulse is composed of a sharp rising edge and a long decay tail, which can be represented by two exponential functions as following (Ficker, et al., 2001):

$$I(t) = A(e^{-\frac{t}{\tau_1}} - e^{-\frac{t}{\tau_2}}), \quad \tau_1 > \tau_2 \quad (2.10)$$

$\tau_1$  is a constant parameter used for governing the long decay tail,  $\tau_2$  is a parameter determining the pulse rise, and  $i$  is a temporal evolution of current pulse.

### 2.3.6: Correlation of the pulse height and charge transfer

A technique proposed by Ficker can be used to obtain the correlation between the pulse height and charge transfer (Ficker, et al., 2001). The total charge transfer in a single pulse,  $q$  is estimated by integrating the Equation 2.10 to infinity. The integration result is shown as:

$$q = A(\tau_1 - \tau_2) \quad (2.11)$$

However, the formula can be simplified to obtain the correlation between the pulse height and charge transfer as following:

$$q = \tau_1 \left(\frac{\tau_2}{\tau_1}\right)^{\frac{\tau_2}{\tau_1 - \tau_2}} \cdot i \quad (2.12)$$

By assuming  $\tau_1$  and  $\tau_2$  to be constant for all DBD pulses, the equation is expressed as:

$$q = \tau_o i \quad (2.13)$$

By utilizing Equation 2.13, the charge transfer can be calculated after obtaining the pulse height. This charge transfer determination from the pulse height requires the experimental time constant  $\tau_o$  from the current pulse integration.

Before the integration of the current pulse, the zero level of the signal is calibrated until the pulse starting current is equal to zero, as shown in Figure 2.8. The time varying current is then corrected by Equation 2.9 to obtain the true discharge current. The discharge pulse height is defined by the maximum true discharge current. Therefore, the temporal evolution of discharge current is integrated from pulse starting time to  $0.5 \mu\text{s}$ , which is much larger than the pulse duration to cover the total charge transfer.

$$q = \int_{t_s}^{t_s + 0.5 \mu\text{s}} I_{dis}(t) dt \quad (2.14)$$

This experiment is also repeated for different space gaps. A linear relation of the charge transfer and the pulse height is obtained in the plot of the charge transfer versus the pulse height as shown in Figure 2.9.

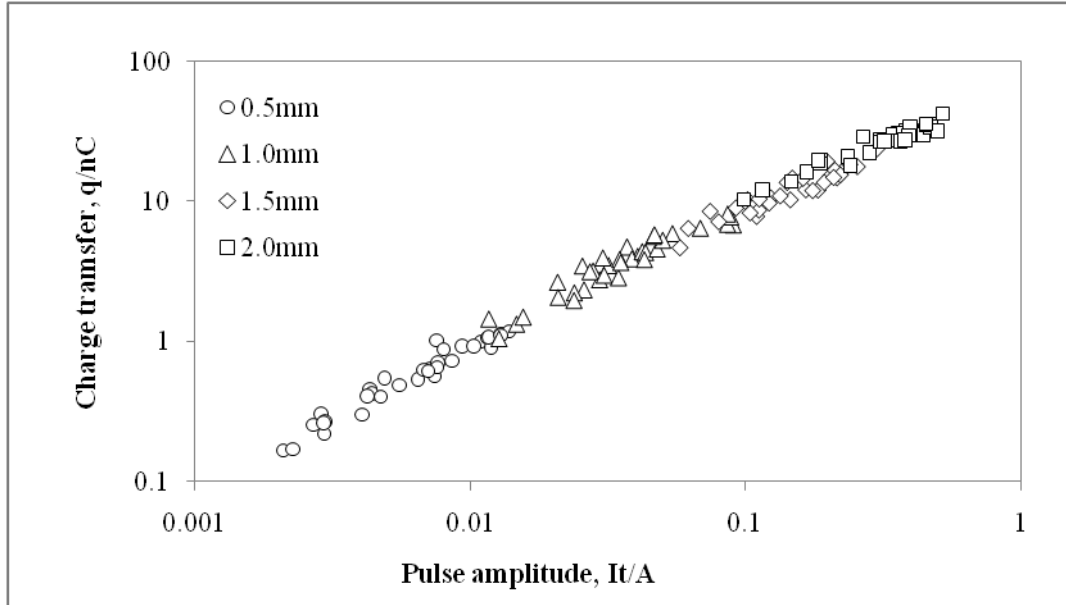


**Figure 2.9:** The straight correlation between the charge and the pulse height.

The time constant,  $\tau_o$  determined from the gradient of the plot is equal to  $77 \pm 2$  ns. The time constants for different configurations are the same indicating that the time constant  $\tau_o$  is not affected by the DBD configuration and the pulse height.

The correlation between the corresponding pulse height and the single pulse charge transfer is then analyzed by the correlation function. The correlation function analysis can be employed to determine the correlation of two quantities. The correlation coefficient is expressed as below:

$$R(x, y) = \frac{\sum_{i=1}^n (x_i - \bar{x})(y_i - \bar{y})}{\sqrt{\sum_{i=1}^n (x_i - \bar{x})^2 \sum_{i=1}^n (y_i - \bar{y})^2}} \quad (2.15)$$

$\bar{x}$  is the mean of the  $x_i$ , while  $\bar{y}$  is the mean of the  $y_i$ . If the two quantities are independent, then the correlation coefficient is equal to zero. If there is a strong correlation between the two quantities, the correlation coefficient is approximately one.

A strong correlation coefficient of 0.975 between the charge transfer and the pulse height is obtained. In view of this high correlation coefficient magnitude, the charge transfer can be confidently determined from the pulse height under our experimental condition.

### 2.3.7 Distribution of current pulses

The pulse height distribution expressed as probability density function  $p(i)$  can be determined by a histogram technique (Ficker, 1995) as below:

$$p(i) = \frac{\Delta N}{N\Delta i} \quad (2.16)$$

$N$  is equal to the total number of the detected pulses per half cycle.  $\Delta N$  is equal to the number of pulses in the interval  $[i + \frac{\Delta i}{2}, i - \frac{\Delta i}{2}]$ . An interval value of  $\Delta i$  can be selected to obtain a representative probability function.

In this project, the pulse height distribution are analyzed by the unconditional probability function. The unconditional probability function is defined as a probability function derived by taking into account of all the detected pulses in the half cycle.

The experimental pulse height distribution, which is shown in the Figure 2.10, is similar to the log normal distribution function. This similar distribution can also be obtained from other corona and DBD statistical studies (Vanbrunt, et al., 1991; Vanbrunt, et al., 1995).

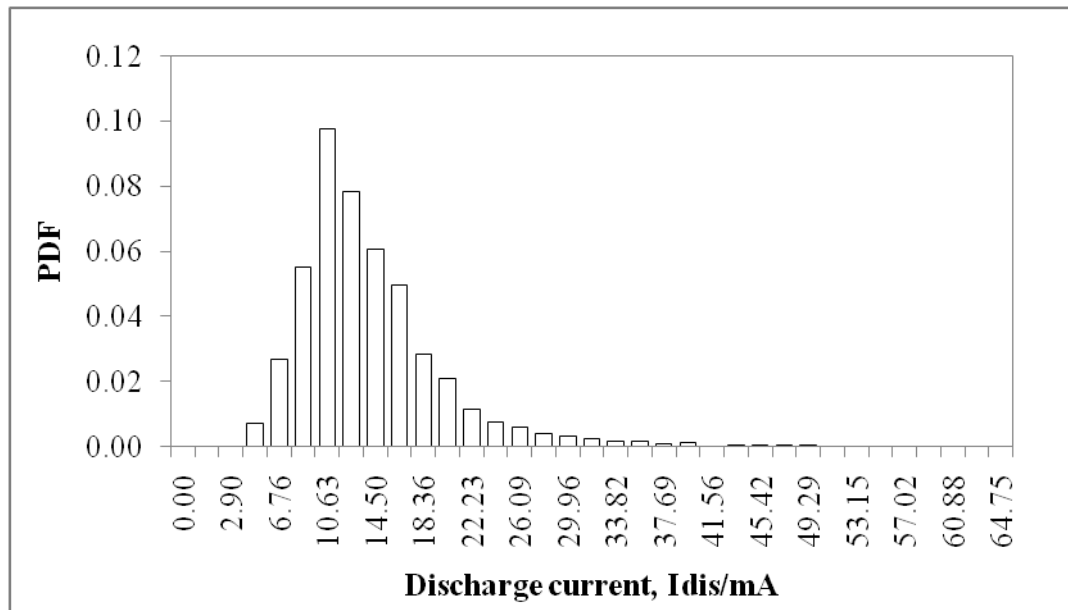


**Figure 2.10:** The typical pulse height distribution.

### 2.3.8 The space gap capacitance and dielectric capacitance

The total effective capacitance of the DBD reactor can be represented by a combination of two capacitors in series (see chapter 1). The existence of the capacitance behavior of DBD reactor is due to the charge polarization of the space gap layer and the dielectric layer. However, the electrical behavior is very sensitive to the space gap and dielectric capacitances. A small error occurring in the calculation of the space gap capacitance or dielectric capacitance will seriously affect the accuracy of the estimate of electrical quantities such as the space gap voltage, dielectric voltage, discharge current and power dissipation. Generally, the space gap and dielectric capacitances are two important parameters in electrical modeling.

The total effective capacitance of the DBD reactor before the breakdown can be obtained by plotting the charge transfer versus the applied voltage. Only a straight line will be observed in the QV diagram before the DBD breakdown. The gradient of the straight line obtained from the QV diagram is equal to the total effective capacitance

( $C_T$ ) of the DBD reactor. The total effective capacitance of the DBD reactor is plotted against the space gap distance for a DBD with glass dielectric layer of 2.0 mm as shown in Figure 2.11.

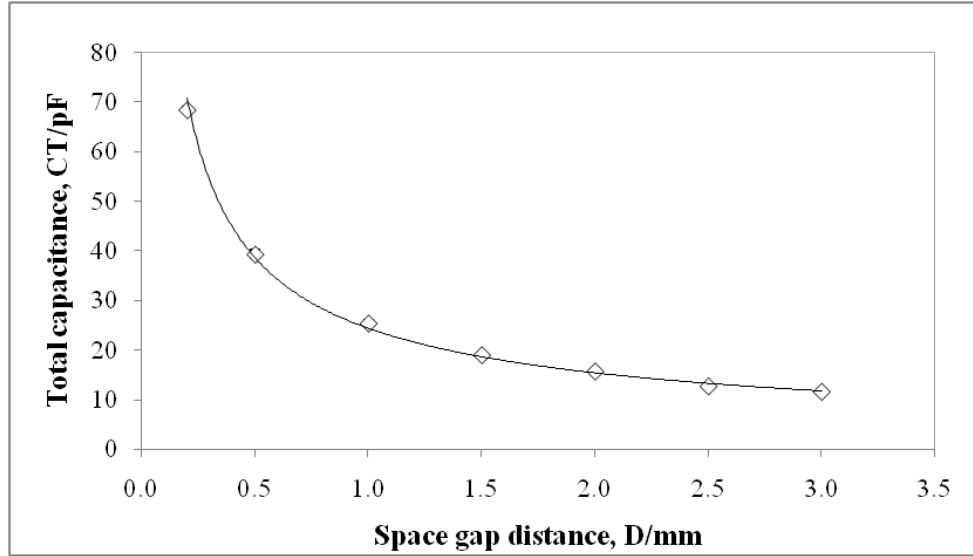


**Figure 2.11:** The total effective capacitance of DBD reactor before breakdown with negligible error.

From the theoretical calculation, the equivalent capacitance  $C_T$  is a combination of two series capacitors based on this equation:

$$C_T = \frac{C_g C_d}{C_g + C_d} \quad (2.17)$$

The space gap capacitance can be calculated from the parallel capacitance expression:

$$C_g = \frac{S \epsilon_r \epsilon_0}{d} \quad (2.18)$$

where  $d$  is the distance of space gap,  $\epsilon_r$  is the relative permittivity, which is taken to be unity, and  $\epsilon_0$  is the vacuum permittivity.

However, the effective area,  $S$  is not equal to the total area of the electrode due to the edge effect. The edge effect, which increases the total effective area, must be considered for electrode with large thickness (Kamchouchi & Zaky, 1975). The total effective area,  $S$  is referred to the summation of the actual electrode area and the edge effect area. The

edge capacitance is directly proportional to the perimeter of the electrode (Kamchouchi & Zaky, 1975).

The experimental dielectric capacitance is obtained by using the QV Lissajous figure method, which will be presented in section 2.3.9. Based on the experimental dielectric capacitance, the total effective capacitance  $C_T$  can be calculated by using Equations 2.17 and 2.18, while, the total effective area,  $S$  is validated with the experimental total effective capacitance. The calculated and experimental  $C_T$  are shown in Figure 2.11. For the best match between the calculated and the experimental  $C_T$ , the total effective area,  $S$  is taken to be  $0.00302 \text{ m}^2$ . The actual electrode area with a radius of 30 mm is approximated to be  $0.00283 \text{ m}^2$ . Assuming the dielectric capacitance to be equal for the same dielectric layer, the average total effective radius for the different space gap is obtained as 31 mm. After knowing the total effective area,  $S$ , the space gap capacitance for different space gap can be calculated by using Equation 2.18.

### **2.3.9 QV Lissajous figure under breakdown condition.**

The simplest way to determine the dielectric capacitance, breakdown voltage, and the energy dissipation is by using the QV Lissajous method under breakdown condition. The typical QV Lissajous figure of DBD under the breakdown condition is shown in Figure 2.12:



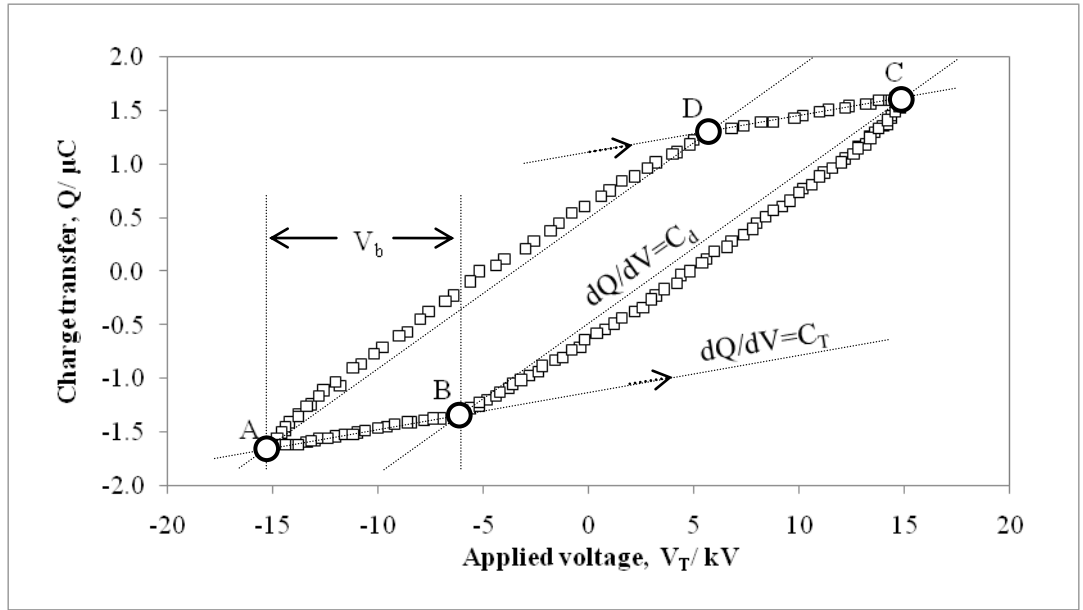


**Figure 2.12:** The typical QV Lissajous figure under breakdown condition.

The gradient of the line between point ‘A’ and point ‘D’, which is parallel with BC line as shown in Figure 2.12, is equal to the dielectric capacitance. The “AD” gradients of different applied voltages are equal. However, the expanded width of the QV Lissajous is observed to be dependence on the applied voltage.

The breakdown voltage of the DBD reactor can be determined from the voltage between the point ‘A’ and point ‘B’, which is indicated as  $V_b$  in Figure 2.12. The breakdown voltage refers to the minimum total applied voltage, which is required for DBD ignition. To calculate the space gap breakdown voltage,  $V_{g,b}$ , the capacitive voltage divider equation can be employed:

$$V_{g,b} = \frac{C_d}{C_d + C_g} V_b \quad (2.19)$$

The space gap breakdown voltage,  $V_{g,b}$  is a function of the space gap distance. The average breakdown voltage with the varied applied voltage versus the space gap distance is plotted as shown in Figure 2.13 below.

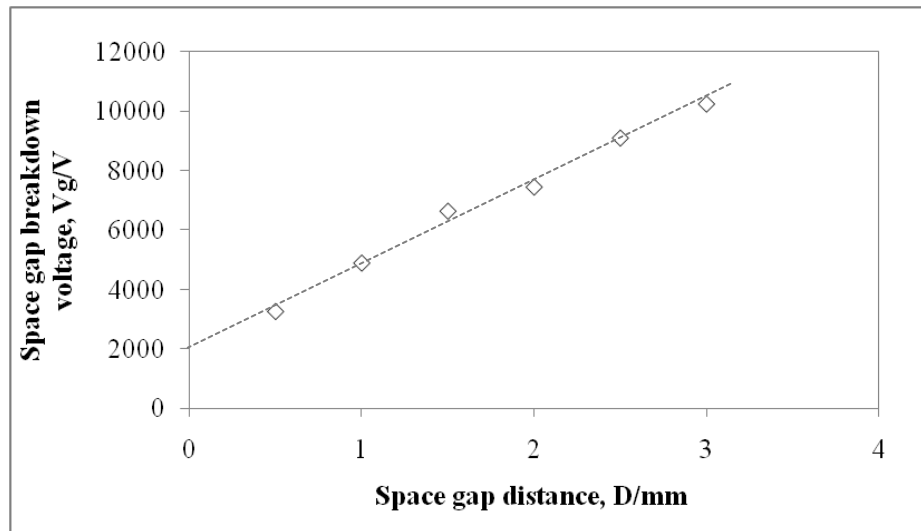


**Figure 2.13:** The space gap breakdown voltage versus the space gap distance.

The total energy dissipated in the DBD reactor can be calculated from the QV Lissajous according to the equation below:

$$E = \oint V(t)dQ \quad (2.20)$$

The enclosed area of the QV Lissajous is exactly equal to the total energy dissipated in DBD reactor. If the QV Lissajous is a perfect parallelogram, the enclosed area can be simply calculated by the Manley's equation, which is derived from the geometry of the QV Lissajous and electrical circuitry equation (see chapter 1).

### 2.3.10 The time evolution of space gap voltage and dielectric voltage

Particularly, the DBD ("ON/OFF") mode is switched in the cycles of "ON" and "OFF" repeatedly, which is governed by the space gap voltage. The DBD is "ON" when the space gap voltage exceeds the space gap breakdown voltage. Whereas, the DBD is "OFF" if the space gap voltage is lower than the space gap breakdown voltage as shown in Figure 2.14. However, the space gap voltage and the dielectric voltage are not directly measurable from the experiment.

$V_g$ ,  $V_d$  and  $V_T$  represent the temporal evolution of voltages between the space gap, the dielectric and the electrodes respectively. The values  $V_T$  can be directly determined by using the high-voltage probe. However, the dielectric voltage is calculated by the general equation: (Liu & Neiger, 2001, 2003; Pal, et al., 2009).

$$V_d(t) = V_d(0) + \frac{1}{C_d} \int_0^t I_T(t) dt \quad (2.21)$$

$V_d(0)$  can be obtained from the dielectric voltage during the initial time. The integrated current can be obtained from the total charge transfer, which is the measured voltage across the charge monitor capacitor  $C_c$ .

$$\int_0^t I_T(t) dt = \frac{V_c(t)}{C_c} \quad (2.22)$$

The dielectric capacitance, used in Equation 2.21, is calculated from the QV Lissajous figure after breakdown (see section 2.3.9). The value of dielectric voltage,  $V_d(t)$  is then utilized to calculate the space gap voltage.

$$V_g(t) = V_T(t) - V_d(t) \quad (2.23)$$

Based on the experimental applied voltage and voltage of charge monitor capacitor, the calculated space gap voltage and dielectric voltage by using Equations 2.21, 2.22, and 2.23 respectively are shown in the Figure 2.14.

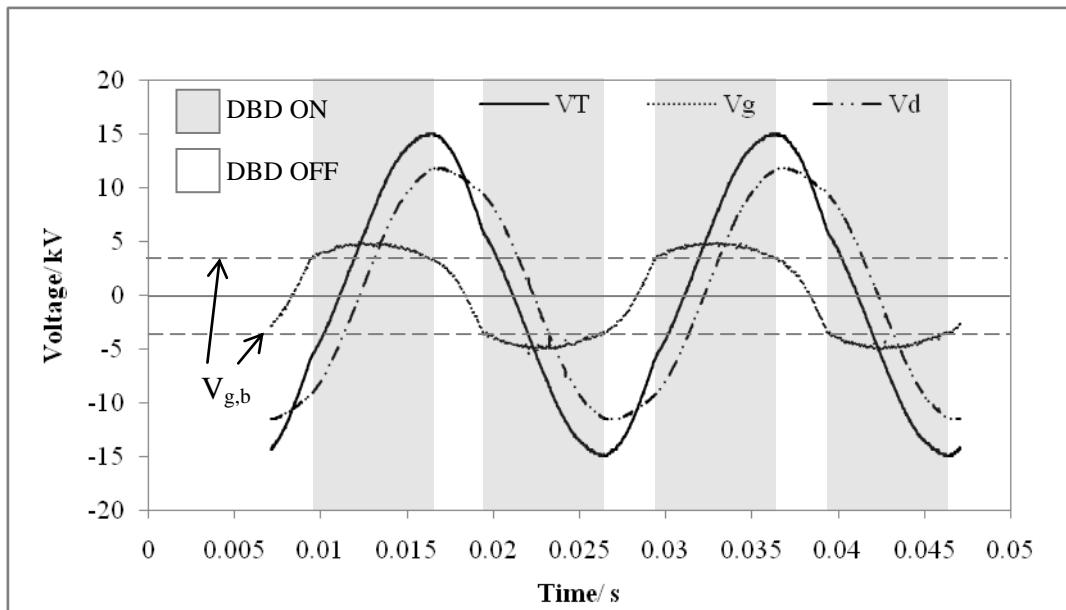


**Figure 2.14:** The typical voltage waveform of the applied voltage, dielectric voltage, and space gap voltage. The gray color background is “ON” mode period. The white color background is “OFF” mode period.

$V_{g,b}$  either in positive or negative magnitude is indicated in Figure 2.14. From the Figure 2.14, the space gap voltage is prior to the phase of the applied voltage. It is attributed to the memory voltage on the dielectric. The memory voltage supports the space gap voltage and triggers the DBD “ON” mode in an earlier time.

# Chapter 3: Electrical Characteristics

## 3.1 Introduction

In this chapter, we shall discuss the electrical characteristics of the DBD system. The electrical characteristics can be investigated by measuring the applied voltage, current, and charge transfer, which have been described in Chapter 2. In particular, the stochastic behavior of the current pulses generated by the filamentary discharge has been investigated.

The investigation of the electrical characteristics has been separately carried out in two series of experiments. First, the stochastic behavior of the current pulses is investigated in order to determine the suitable condition for effective operation of the DBD. The energy dissipation during the discharge is then determined from the charge transfer.

In the first part, the properties of the current pulse amplitude have been investigated to obtain the representative probability function. The correlation between the amplitude of the pulse and pulse separation time has also been determined. The results show that the pulse amplitude is related to the rate of rise of the applied voltage which can be predicted by Manley's formula. This is attributed to the fact that the total charge transported is essentially proportional to the rise of applied voltage during the DBD "ON" period. Based on the experimental results, a probability function expressed in terms of the applied voltage and random breakdown voltage has been derived. This probability function is successfully matched with experimental result.

For the second part, the charge transfer,  $Q$  is measured in order to determine the deposited energy during the discharge. From the charge transfer signal, the QV Lissajous figure can be plotted for the energy dissipation calculation. The enclosed area of the QV Lissajous figure is equal to the total energy dissipated by the DBD. From the experimental observation, a significant expansion of the QV Lissajous figure indicates the occurrence of more energy dissipation in the DBD. This phenomenon can be explained by the surface resistance effect. Particularly, an unbalance potential is believed to be present on the dielectric surface during the discharge. Accordingly, the charges from microdischarge can spread on the dielectric surface due to the unbalance potential. The extra energy is being consumed during the charge spreading through the surface resistance. An electrical model taking into consideration of the dielectric surface resistance is formulated to simulate the expansion of the QV Lissajous figure. This electrical model also explains the increase of breakdown voltage with increasing applied voltage. The surface resistance model can be used to estimate the energy dissipation of the DBD and the surface charge spreading.

## **3.2 The Statistical Studies of Discharge Behavior of DBD**

### **3.2.1 The experimental current pulse distribution**

The typical current pulse amplitude distribution obtained by using the common histogram technique is similar to a log-normal distribution as shown in Figures 3.1, 3.2, 3.3, and 3.4. Commonly, a long tail can be observed at right hand side of the distribution peak. By increasing the applied voltage, the tail of the probability distribution is stretched to the right hand side and the mean of the current pulse amplitude increases with increasing applied voltage.

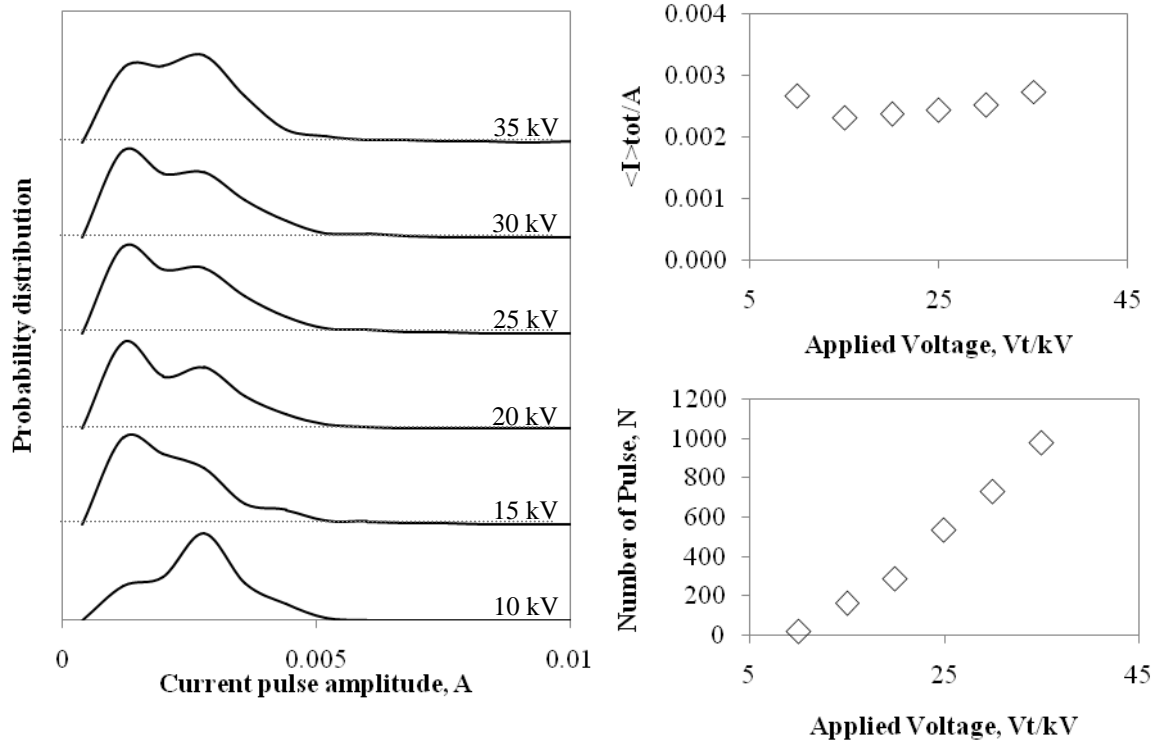


Figure 3.1: The PDF of 0.5 mm space gap.

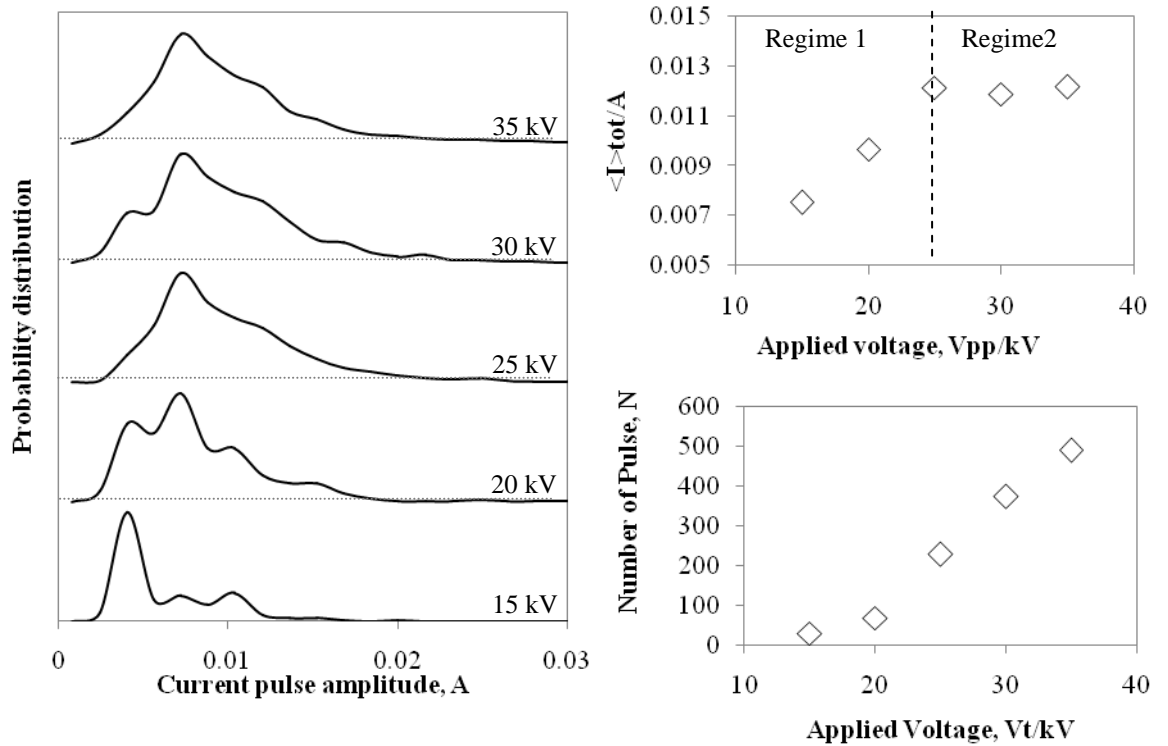
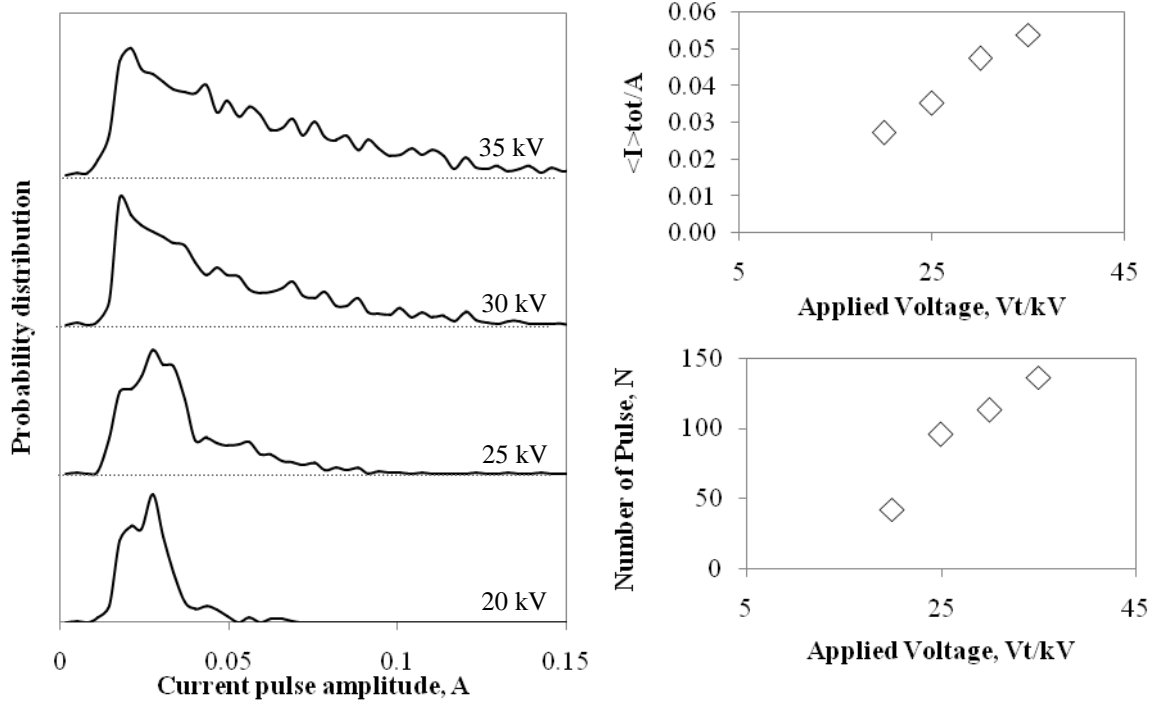
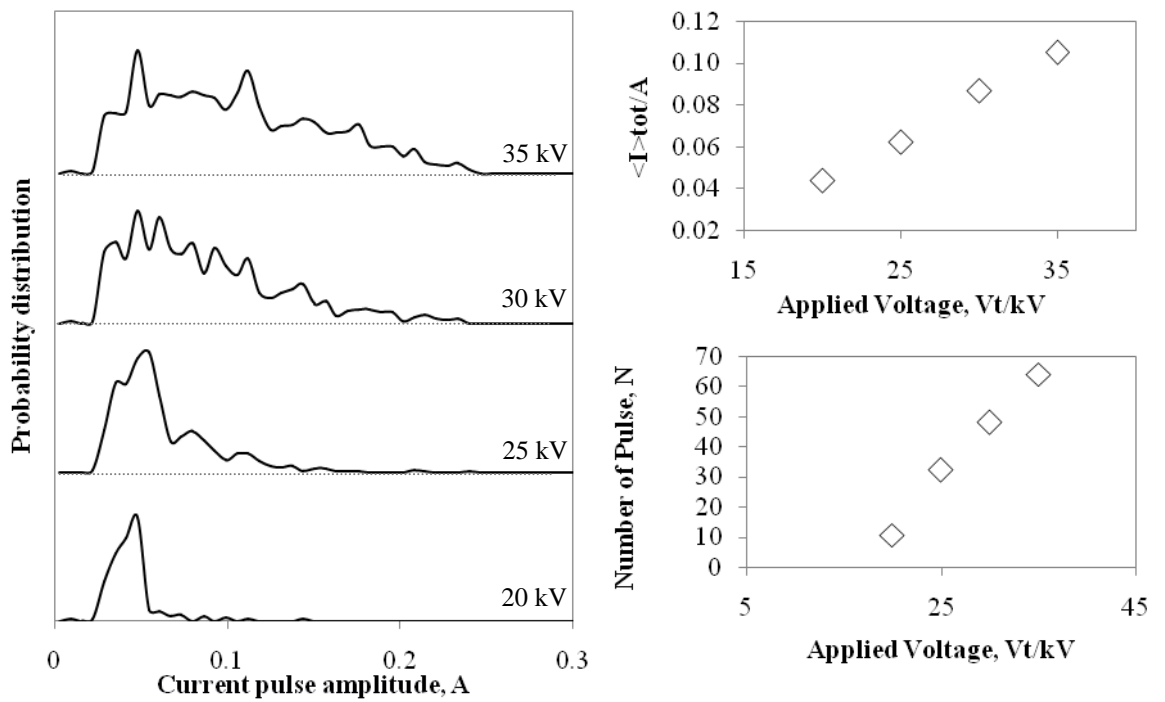


Figure 3.2: The PDF of 1.0 mm space gap.



**Figure 3.3:** The PDF of 1.5 mm space gap.



**Figure 3.4:** The PDF of 2.0 mm space gap.



Further analyses of the current pulse distribution for the case of 1 mm space gap shows that there can be two regimes of average pulse amplitude as shown in the Figure 3.2. The regime transition voltage,  $V_{pp}^t$ , which had been observed by several researchers (Reichen, et al., 2010), is the minimum applied voltage to obtain the maximum average amplitude of current pulse. In regime 1, the average pulse amplitude is increasing with the discharge voltage while in regime 2 the average pulse amplitude is constant. In the case of 1 mm space gap,  $V_{pp}^t = 25$  kV. However, for the case with 0.5 mm space gap, only regime 2 is observed in the range of discharge voltage from 10 to 35 kV, whereas in the case of 1.5 and 2.0 mm space gap, only regime 1 is observed. For the cases of 2.0 mm and 1.5 mm space gap, the tail of the distribution is found to extend further with the applied voltage. The regime transition voltage,  $V_{pp}^t$  is higher than the maximum applied voltage limited by the power supply available, which is 40 kV pk-pk in this case.

According to the experimental observation, we suggest that the increase in the discharge current pulse amplitude can be attributed to the increase in the number of the current channel ignited at higher voltage. In the case of the narrow gap (<1.5 mm) with discharge voltage at or above the critical voltage, the discharge electrodes have been fully cover by current channels, thus further increases in applied voltage will not give rise to higher amplitude current pulse.

The increase in the applied voltage will increase both number of the current pulses as well as the pulse height in regime 1. The number of pulses for smaller space gap is increasing more rapidly with the applied voltage if compared to the case of larger space gap. However, the average height of pulses remains the same with increase of the applied voltage in regime 2. For applications that require high pulse height, it is more

effective to operate the DBD with larger space gap rather than with higher applied voltage.

On the other hand, in order to design a DBD to produce uniform pulses, the DBD reactor should be operated with small space gap (<1.0 mm). Besides, the applied voltage should be higher than  $V_{pp}^t$  to ensure that the pulse height is not affected by the variation of applied voltage.

### **3.2.2 The time separation between consecutive current pulses**

The time separation between consecutive current pulses can be affected by the residual charges generated during the previous pulse. The previous pulse creates a negative electric field which prevents the occurrence of the next pulse at the same position until the electric field builds up again by the rise of applied voltage in the same cycle. Therefore, the occurrence of discharge pulses at the same position is delayed by a time separation which is dependent on the rise of applied voltage and the charge transferred by the discharge pulses. This effect is more apparently observed in a single channel microdischarge as shown in Figure 3.5 (a).

The total charge transfer in DBD is given by Manley's formula as:

$$Q_T = C_d(V_T - V_b) \quad (3.1)$$

Here  $Q_T$  is the total charge transfer,  $C_d$  is the dielectric capacitance,  $V_T$  is the applied voltage and  $V_b$  is the breakdown voltage. This can be taken to confirm that the Manley equation's validity for filamentary discharge.

By differentiating both sides of Equation 3.1:

$$\frac{dQ}{dt} = C_d \frac{dV_T}{dt} \quad (3.2)$$

In fact, the amplitude of the DBD pulse is weakly dependent on the applied voltage after the transition voltage in regime 2 as determined in Section 3.2.1 earlier. If the average charges transferred per pulse by the current pulses is assumed constant, the charge transferred per second is approximated to be the charges transferred by a single pulse divided by the time separation between two consecutive pulses, i.e.:

$$\frac{dQ}{dt} \approx \frac{\langle q \rangle}{\langle \Delta t \rangle} \quad (3.3)$$

$\langle q \rangle$  is the average charge transferred by a single current pulse, while  $\langle \Delta t \rangle$  is the average time separation between two consecutive pulses.

Then Equation 3.2 can be written as:

$$\frac{\langle q \rangle}{\langle \Delta t \rangle} = C_d \frac{dV_T}{dt} \quad (3.4)$$

and,

$$\langle q \rangle = \langle \Delta t \rangle C_d \frac{dV_T}{dt} \quad (3.5)$$

From this simple expression, it can be seen that the time separation is directly proportional to the charge transferred per pulse. This equation will give a very accurate estimate of the time separation for a single microdischarge channel. According to Equation 3.5, the time separation is correlated to the charge transferred by the discharge and gives a uniform time separation of pulses if the charge transfer per pulse is uniform.

In order to demonstrate the concept of Equation 3.5 for the correlation of the pulse height and time separation of a single channel, the electrode geometry has been modified. A short length of copper wire with diameter of 1 mm and length of 2 mm is attached to the centre of the electrode which is not covered by dielectric. The applied voltage is slowly increased until only one microdischarge channel is ignited at the needle. Multiple microdischarge pulses are ignited to occur at fixed frequency from the needle to the surface of the dielectric. Figure 3.5 (a) shows the train of current pulses obtained. For the case of single microchannel, the discharge current occurs in a more regular time separation and uniform pulse amplitude.

However, the actual geometry of the DBD is a parallel plate geometry. The DBD discharge consists of many filamentary structures in which each filament is considered to be a microdischarge channel. All the microdischarges are separated by interleaved non-discharging regions. The filamentary discharge channels are randomly distributed both spatially and temporally. Hence, the current signal pattern is stochastic in nature and all the microchannels are overlapping together resulting in discharge current signal as shown in Figure 3.5 (b).

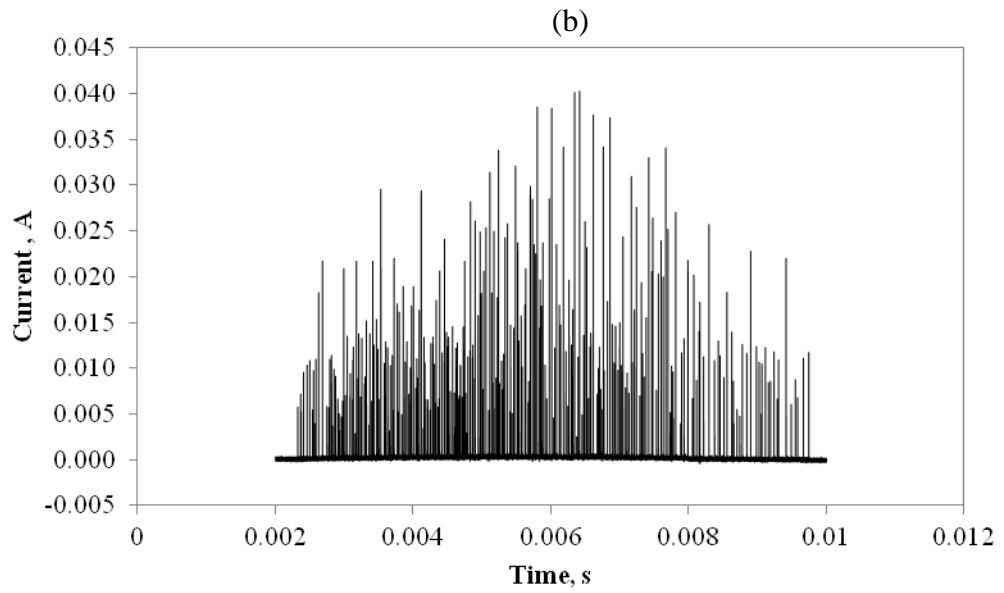
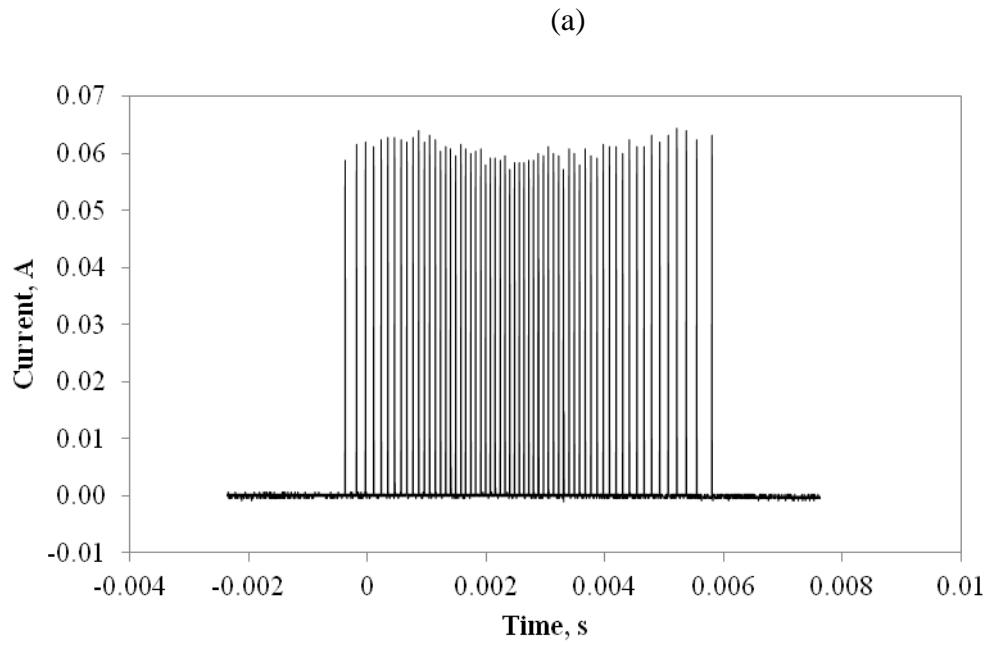


**Figure 3.5:** Comparison of (a) the single point microdischarge with (b) multiple channels microdischarge.

An attempt has been made to analyse the correlation between the pulse separations and the pulse amplitude in parallel plate geometry. Generally, the average time separation is dependent on the total number of pulses ignited per cycle. A larger number of the pulses generated in the same cycle will give rise to shorter time separation. From the experimental results as shown in Section 3.2.1, the number of pulses is proportional to the difference between the applied voltage and the breakdown voltage. It is believed to be attributed to the increase in the total charge transfer for discharge with higher applied voltage as predicted by Equation 3.1.

For the parallel plate geometry, the DBD is generated in a large number of channels resulting in the stochastic behavior of the time separation between pulses. Therefore, a series of the data analyses of the time separation dependent on the charge transfer have been carried out.

The validity of the modified Manley's formula as given by Equation 3.5 will be verified by experimental results as illustrated in the following discussion. Three variable parameters,  $\langle q \rangle$ ,  $\langle \Delta t \rangle$ , and  $dV_T/dt$  are required in Equation 3.5. The change of the applied voltage with time ( $dV_T/dt$ ) has to be obtained first. For this purpose, the current pulses within a time interval where the  $dV_T/dt$  is approximately linear are chosen as shown in Figure 3.6.

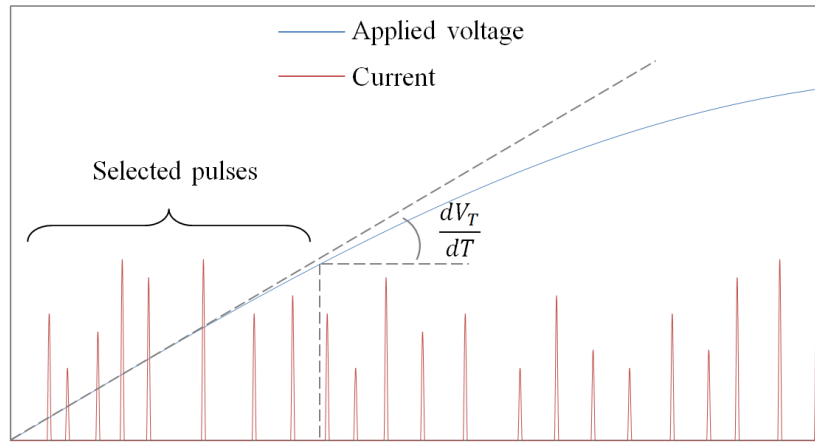


**Figure 3.6:** The gradient of applied voltage near to the zero voltage is determined and only the pulses occur in this range of  $dV_T/dt$  are selected for analysis.

$\langle q \rangle$  had been shown in Section 2.3.6 to be directly proportional to the average current pulse height  $\langle i \rangle$ . The cases with space gap of 1.0 mm and applied voltage larger of 25, 30 and 35 kV where the distribution of current pulses is in regime 2 (and hence the applied voltage does not affect the total average pulse height) are selected for this analysis. From the experimental results, the average current pulse height  $\langle i \rangle$  and hence the charge transferred  $\langle q \rangle$  is linearly proportional to the time separation between consecutive pulses as shown in Figure 3.7.

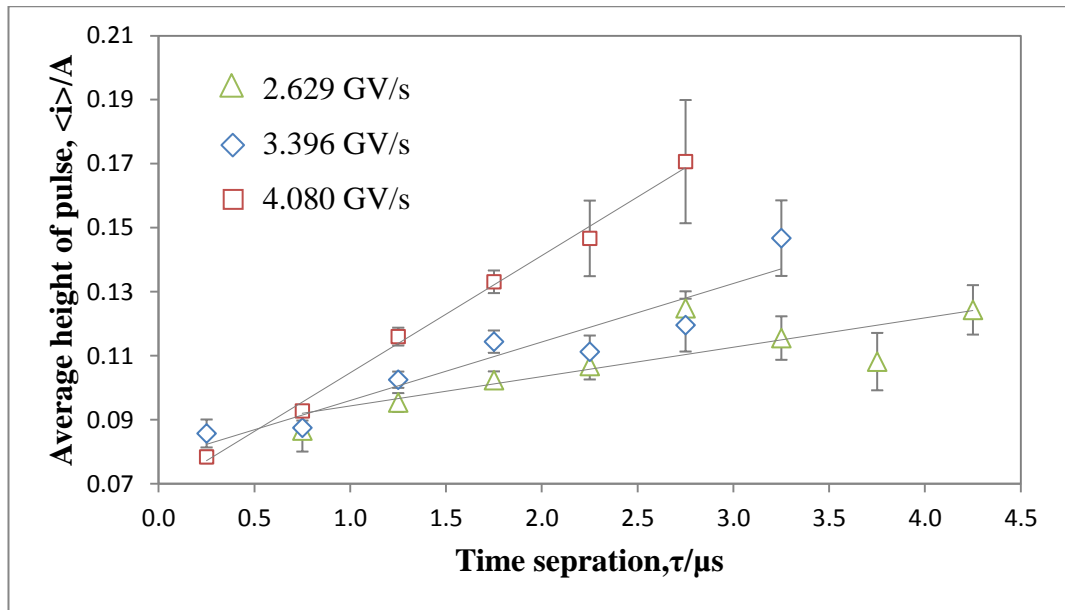


**Figure 3.7:** The correlation between the average height of current pulses and the average time separation for  $dV_T/dt$  of 2.629 GV/s, 3.396 GV/s and 4.080 GV/s.

Figure 3.7 shows that the higher charge transferred by a single pulse, the longer is the time separation of the next pulse for DBD discharge with constant  $dV_T/dt$ , which is in agreement with Equation 3.5. However, it can be observed that the intercept of the plot in Figure 3.7 does not pass through the origin, and the gradient does not agree with that predicted by Equation 3.5. This is suggested to be caused by the effect of multiple channels, and the non-impulsive current.

For the case of multiple channels, the detected pulses are a superposition of current pulses from difference channels. The time separation between consecutive pulses of a single channel is affected by the superposition of current pulses generated through other discharge channel. However, the overall effect of increasing pulse height with time separation has been observed in our experiments. The gradient of the line in Figure 3.7 is dependent on the  $dV_T/dt$ . Larger gradient is expected for larger  $dV_T/dt$  as predicted by Equation 3.5



A correction factor is required to be introduced in Equation 3.1 to estimate the total number of pulses occurring in a cycle and the total charge transfer of all channels. The total charge transfer calculated from the Manley's formula includes the impulsive current and non-impulsive current (see chapter 1 and chapter 2). However, the charge transfer by non-impulsive charges is not measured in this experiment. Therefore, the correction factor  $c_{cor}$  is believed to be the ratio of the charge transferred by impulsive current to the total charge transferred by DBD.

The results suggest that the concept of Manley's formula is valid for predicting the number of pulses in each channel. Hence, the corrected Manley's formula can be used in the distribution function modelling to be presented in Section 3.2.3.

### **3.2.3 The empirical distribution function**

Based on the experimental results on the time separation and pulse height distribution obtained earlier, a statistical function governing the current pulse distribution has been constructed with consideration of the charge transfer equation. The proposed probability function is a function of some important experimental parameters such as applied voltage, dielectric capacitance, space gap capacitance, and space gap distance.

The basic concepts of the DBD in filamentary mode have been considered in the derivation of the proposed probability density distribution. When the applied voltage reaches the breakdown voltage, a discharge filament is generated, and the charges will be transported to the dielectric surface in a few nanoseconds. An inverting local electric field will be developed across the discharge gap at the breakdown location due to the

charge accumulation on the dielectric surface until the discharge is quenched. The next ignition of DBD discharge located at the same channel will occur after sufficient local electric field has been recovered by the applied voltage again. The ignition and quenching processes of the discharge at local channels are repeated at the same half cycle before the change of voltage polarity.

An important feature of the filamentary discharge in parallel plate geometry is the existence of multiple channels as shown in Figure 3.5. It is well illustrated by many experimental observations that there exist fixed discharging regions on the electrode where repetitive discharge ignitions occurring at the same locations during consecutive discharge cycles (Chirokov, et al., 2006). The lifetime of one microdischarge is only a few nanoseconds, but repetitive occurrence of multiple microdischarges at the same location make them appear as continuous.

Based on this concept, our model is developed by representing the microdischarge by small discrete regions as shown in Figure 3.8. The individual channel is occupying a small effective area due to charge diffusion and repulsion force between channels. This small effective occupied area determines the capacitance magnitude, breakdown voltage and discharge charge transfer for that channel. The total occupied area of a single channel on the dielectric surface strongly affects the total charge transfer through that channel. It is further determining the number of the pulses generated through that channel by Manley's formula as presented in Section 3.2.2.

In our work, the different breakdown voltage of channels at different location has been considered. Nevertheless, the current pulse generated by the individual channel at the same location may also follow a certain random function.

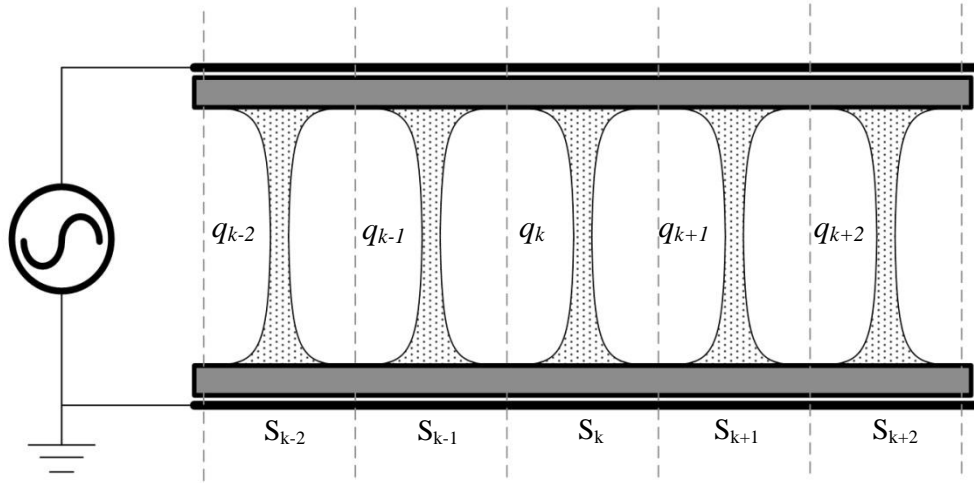


**Figure 3.8:** The schematic diagram of the multiple microdischarge channels.

In Figure 3.8, the area  $S_k$  is the area occupied by the channel  $k$ , the  $u(k)$  is the breakdown voltage of that channel, and the  $q(k)$  is the charge transfer from a single discharge pulse if the current pulse is generated.

If the function of breakdown voltage,  $u$  is directly corresponding to discharge pulse, the number density function of current pulses with amplitude in the range of  $i$  to  $i + \Delta i$  is expressed as:

$$\int_i^{i+\Delta i} n_p(i) di = \int_u^{u+\Delta u} n_p(u) du \quad (3.6)$$

$n_p(i)$  is the total number density of the pulses with current amplitude  $i$ ,

$n_p(u)$  is the total number density function of the pulses with breakdown voltage  $u$ .

The total charge transfer can be estimated by using the breakdown voltage, and the total number of pulses can be obtained from the total charge transfer divided by charge transfer per single pulse. This is the simplest expression used to start a derivation from the function in term of breakdown voltage  $n_p(u)$  instead of from the function expressed in term of current pulse,  $n_p(i)$ . The probability function in term of breakdown voltage,  $n_p(u)$  is introduced based on several assumptions. First, the discharge channels are

assumed to be generated with random breakdown voltage due to the non-uniform surface of the dielectric and electrodes. In our case, the probability function of random breakdown voltage is considered to be following normal distribution function with a standard deviation value,  $\sigma$ .

$$f(u) = \frac{1}{\sqrt{2\pi\sigma^2}} e^{-\frac{(u-\bar{u})^2}{2\sigma^2}} \quad (3.7)$$

The charge transferred by a single current pulse is given by a simplified exponential function expressed in the term of breakdown voltage, which is determined from the experimental results given by:

$$q(k) = \tau_o i_o e^{\alpha u(k)} \quad (3.8)$$

Here,  $\tau_o$  is the time constant of the discharge pulse which can be obtained from Equation 2.13 in chapter 2 and is estimated as  $77 \pm 2$  ns.  $u(k)$  is the space gap breakdown voltage of the channel  $k$ ,  $i_o$  and  $\alpha$  are constants whose values depend on the gas used. The parameter  $\alpha$  is similar to the first discharge coefficient from Townsend's discharge theory (Ficker, 2003). For the computation,  $i_o$  is taken as 0.21 mA and  $\alpha$  is taken as  $0.612 \text{ mV}^{-1}$ , which have been determined from the experimental results.

In our consideration, the charge distribution at different locations on the electrode surface is introduced. The effective occupied area  $S_k$  of individual channel  $k$  is directly proportional to the dielectric capacitance of that channel. This can be expressed by the equation:

$$C_{d,k} = C_d \frac{S_k}{S} \quad (3.9)$$

where  $S$  is equal to the total area of electrode.  $C_d$  is the total dielectric capacitance measured from QV Lissajous figure. The number of discharge pulses can be calculated from the total charge transfer through a single channel. Here, the total charge transferred by DBD in a half cycle is estimated by the modified Manley's equation (Manley, 1943).

The total charge transferred consists of the charges from impulsive discharge and non-impulsive discharge. Therefore, a factor,  $c_{cor}$  is introduced to the modified Manley's equation. The factor  $c_{cor}$  is the ratio of the charge transferred by impulsive current to the total charge transferred by DBD.

$$Q_T = c_{cor}C_d(V_T - \frac{2(c_d+c_g)}{c_d}V_b) \quad (3.10)$$

In our case, the discharge current is divided into channels that are assumed to be not interacting with each other.

$$Q_T(k) = c_{cor}C_{d,k}(V_T - \frac{2(c_d+c_g)}{c_d}u(k)) \quad (3.11)$$

Here,  $Q_T(k)$  is the total charge transferred by an individual channel  $k$  in half cycle,  $C_{d,k}$  is the effective dielectric capacitance associated with individual channel  $k$ . By using the total charge transferred and the charges carried by a single current channel, the total number of pulses associated with a single channel  $k$  can be estimated:

$$n_{p,s}(k) = \frac{Q_T(k)}{q(k)} \quad (3.12)$$

$n_{p,s}(k)$  is the total number of pulses generated in the single channel  $k$ .

For the large number of channels, some of the channels are generating similar discharge pulses due to similar breakdown voltage. The number density of channels with equal discharge pulses and breakdown voltage,  $u$  is represented by  $n_c(u)$ . Therefore, the total number density of similar discharge pulses with similar breakdown voltage,  $u$  is equal to number of pulses carried by a single channel multiplied by the number of channels with breakdown  $u$ , i.e.

$$n_p(u) = \frac{n_c(u)Q_T(u)}{q(u)} \quad (3.13)$$

$Q_T(u)$  is the total charge transferred by the channel with breakdown voltage  $u$ .  $q(u)$  is the charge transferred by a single current pulse with breakdown voltage  $u$ . Substituting Equation 3.11 into Equation 3.13:

$$n_p(u) = \frac{n_c(u)c_{cor}C_{d,s}(V_T - \frac{2(C_d+C_g)}{C_d}u)}{q(u)} \quad (3.14)$$

If the area occupied by every channel is assumed to be equal, then, the dielectric capacitance of a single channel can be estimated as

$$C_{d,k} = \frac{C_d}{N_c} \quad (3.15)$$

where  $N_c$  is the total number of channels. Hence,

$$n_p(u) = c_{cor} \frac{n_c(u)}{N_c} \frac{C_d(V_T - \frac{2(C_d+C_g)}{C_d}u)}{q(u)} \quad (3.16)$$

If the number of channels is sufficiently large,  $\frac{n_c(u)}{N_c}$  is the approximate probability

density of breakdown voltage as a function of  $u$  given by Equation 3.7. Therefore,

$$\int_u^{u+\Delta u} n_p(u) du = \int_u^{u+\Delta u} c_{cor} \frac{1}{\sqrt{2\pi\sigma^2}} e^{-\frac{(u-\bar{u})^2}{2\sigma^2}} \frac{C_d(V_T - \frac{2(C_d+C_g)}{C_d}u)}{\tau_o i_o e^{\alpha u}} du \quad (3.17)$$

We are interested to obtain the distribution function with discharge pulses. Hence, the number density distribution  $n_p(i)$  as a function of  $i$  is transformed from the density distribution  $n_p(u)$  in the function with  $u$ . This procedure is performed by changing the variable to  $i$  by the integration method, we obtain:

$$\int_u^{u+\Delta u} n_p(u) du = \int_{i_1}^{i_2} C_{cor} \frac{1}{\sqrt{2\pi\sigma^2}} e^{-\frac{(\frac{1}{\alpha} \ln(\frac{i}{i_o}) - \bar{u})^2}{2\sigma^2}} \frac{C_d(V_T - \frac{2(C_d+C_g)}{C_d} \frac{1}{\alpha} \ln(\frac{i}{i_o}))}{\alpha \tau_o i^2} di \quad (3.18)$$

By comparing Equation 3.18 with Equation 3.6, a general solution of this model is obtained:

$$n_p(i) = c_{cor} \frac{C_d V_T - 2(C_d + C_g) \frac{1}{\alpha} \ln(\frac{i}{i_o})}{\alpha \tau_o i^2 \sqrt{2\pi\sigma^2}} e^{-\frac{(\frac{1}{\alpha} \ln(\frac{i}{i_o}) - \bar{u})^2}{2\sigma^2}} \quad (3.19)$$

Equation 3.19 is an empirical distribution function, which can be used for predicting the pulse distribution. The correction factor,  $c_{cor}$  in Equation 3.19 is validated by the experimental results to be presented in Section 3.2.4.

### 3.2.4 Comparison of experimental results and proposed distribution function

The minimum breakdown voltage, time constant, dielectric capacitance and space gap capacitance used in Equation 3.19 had been determined in Chapter 2 earlier. The standard deviation of breakdown voltage and the correction factor,  $c_{cor}$  in Equation 3.19 are validated by the experimental distribution. The parameters are listed in Table 3.1. The mean space gap breakdown voltage,  $\bar{u}$  is the summation of minimum breakdown voltage and three times standard deviation voltage.

**Table3.1:** List of the parameters used in the PDF function equation.

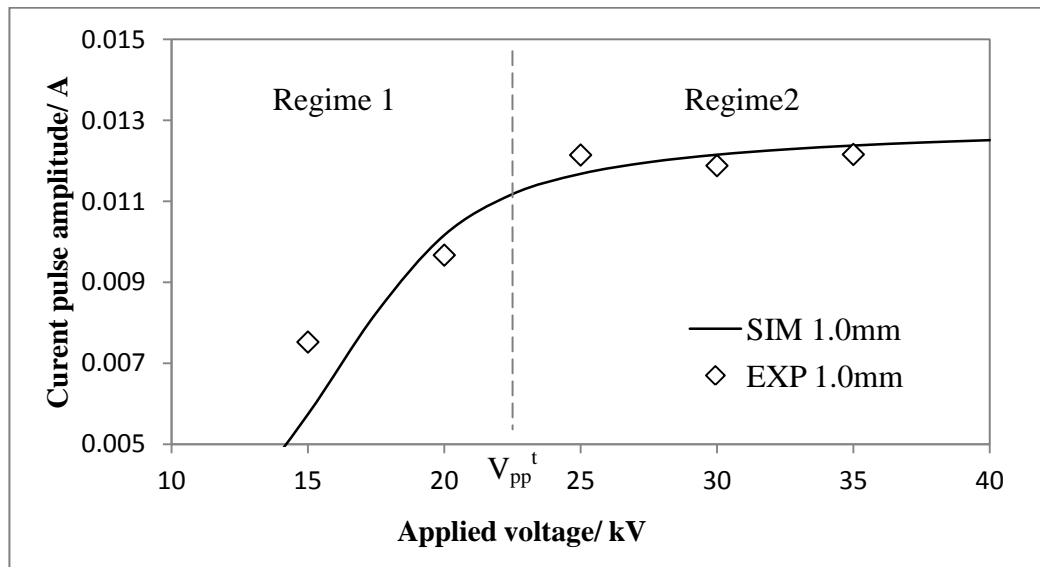
| Space gap<br>distance/mm | Minimum<br>$V_{g,b}/V$ | Standard<br>deviation, $\sigma$<br>/ V | $C_d$ /nF | $C_g$ /pF | Correction<br>factor, $C_{cor}$ |
|--------------------------|------------------------|--|-----------|-----------|---------------------------------|
| 0.5 mm                   | 2930                   | 700                                    | 0.137     | 57.0      | 0.126571                        |
| 1.0 mm                   | 4540                   | 800                                    | 0.137     | 28.5      | 0.245669                        |
| 1.5 mm                   | 6580                   | 1000                                   | 0.137     | 19.0      | 0.333766                        |
| 2.0 mm                   | 8180                   | 820                                    | 0.137     | 14.2      | 0.403303                        |

The parameters used in Equation 3.19 are independent of applied voltages. It allows us to predict the pulse distribution by using this equation without limitation of experiment. Equation 3.19 can also be used to predict the pulse distribution in the two discharge regimes. For applied voltage before the regime transition voltage,  $V_{pp}^t$ , the average discharge current amplitude rapidly increases with applied voltage (regime 1). For applied voltage higher than  $V_{pp}^t$ , the average discharge current amplitude reaches a saturation value (regime 2). From the prediction using our model, the increasing number of channels at higher applied voltage resulting in the amplitudes of pulses to increase in regime 1. For regime 2, all the possible breakdown channels have been ignited. Further

increase of the applied voltage will not generate additional breakdown channel. Therefore, the average amplitude of the discharge pulses will reach a saturation value. In the current experiment, the space gap transition voltage is approximately equal to summation of three times standard deviation voltage and the mean of the breakdown voltage. Hence, the equivalent transition voltage,  $V_{pp}^t$  can be estimated as:

$$V_{pp}^t = \frac{2(c_d+c_g)}{c_d}(\bar{u} + 3\sigma) \quad (3.20)$$

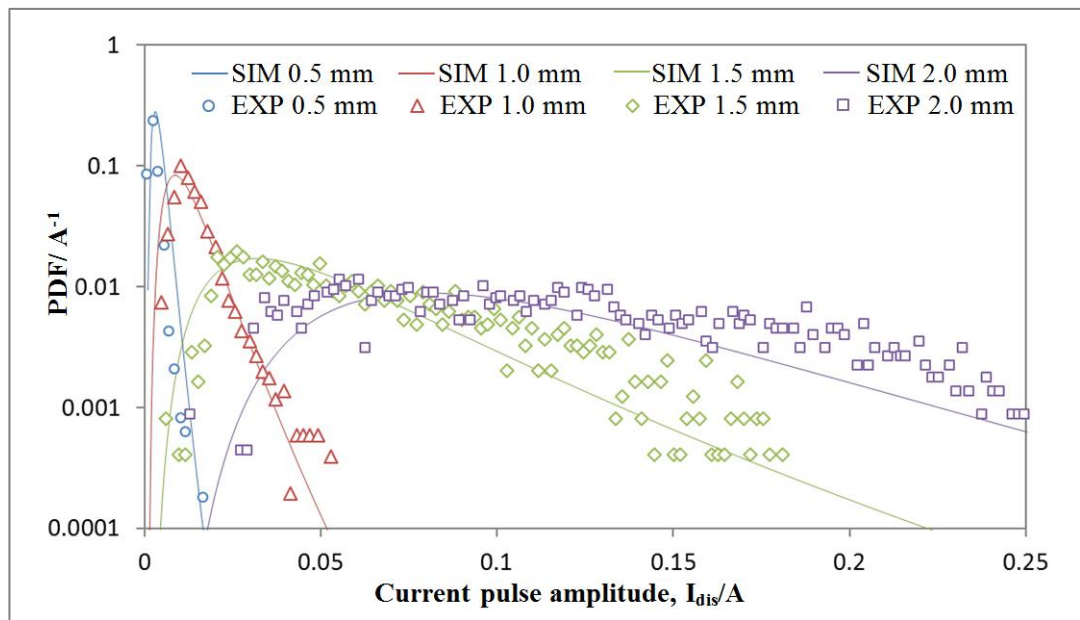
For our experimental results, the pulse distribution for discharge with space gap distance of 1.0 mm is clearly observed to consist of two discharge regimes. According to the empirical Equation 3.19, almost all the channels are ignited after the applied voltage reaches 22.6 kV, which can be considered to be the actual regime transition voltage,  $V_{pp}^t$ . The comparison of experimental regime transition voltage with the simulated result is shown in Figure 3.9.



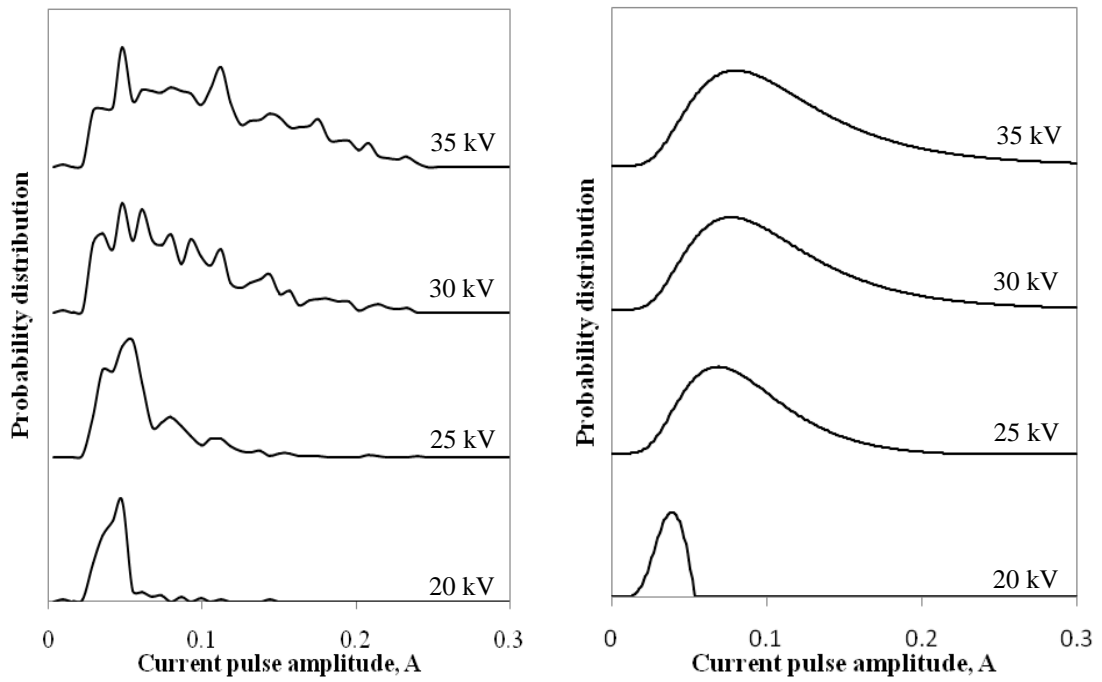
**Figure 3.9:** The comparison of experimental regime transition voltage with simulated result for discharges with 1.0 mm space gap.  $V_{pp}^t$  is the simulated regime transition voltage obtained by using Equation 3.20. The full line is simulated by using Equation 3.19 for each applied voltages.



Figure 3.10 shows that the experimental results are in good agreement with the simulated PDF for discharges with various space gaps. The factor  $c_{cor}$  is due to the combined effect of the ratio of the impulsive charges to total charge transferred by DBD in half cycle. The number of pulses and the average pulse amplitude at different discharge voltages and different space gaps can be predictable by using Equation 3.19 with constant factor  $c_{cor}$  as shown in Figure 3.12 and Figure 3.13 respectively. It is demonstrated that the value of the factor  $c_{cor}$  is not influenced by the applied voltage at 50 Hz.



**Figure 3.10:** The comparison of the computational results and experimental results for PDF with different space gaps with 35 kV pk-pk applied voltage.



**Figure 3.11:** The comparison between the experimental results (left) and the simulated pulse distributions for discharges with 2.0 mm space gap.

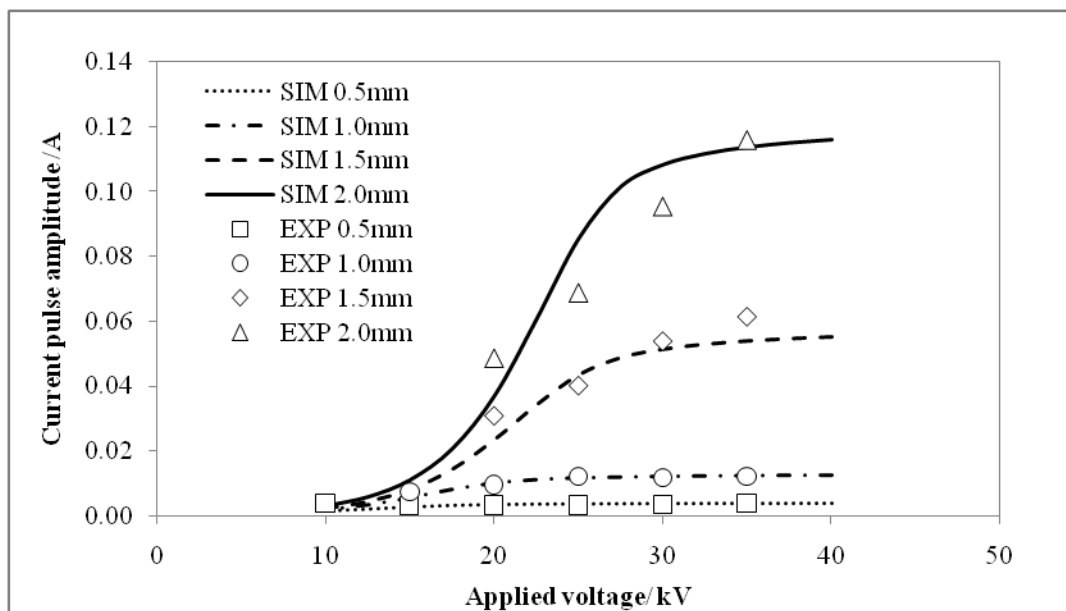


**Figure 3.12:** Comparison of the experimental current pulse amplitude with the simulated results.

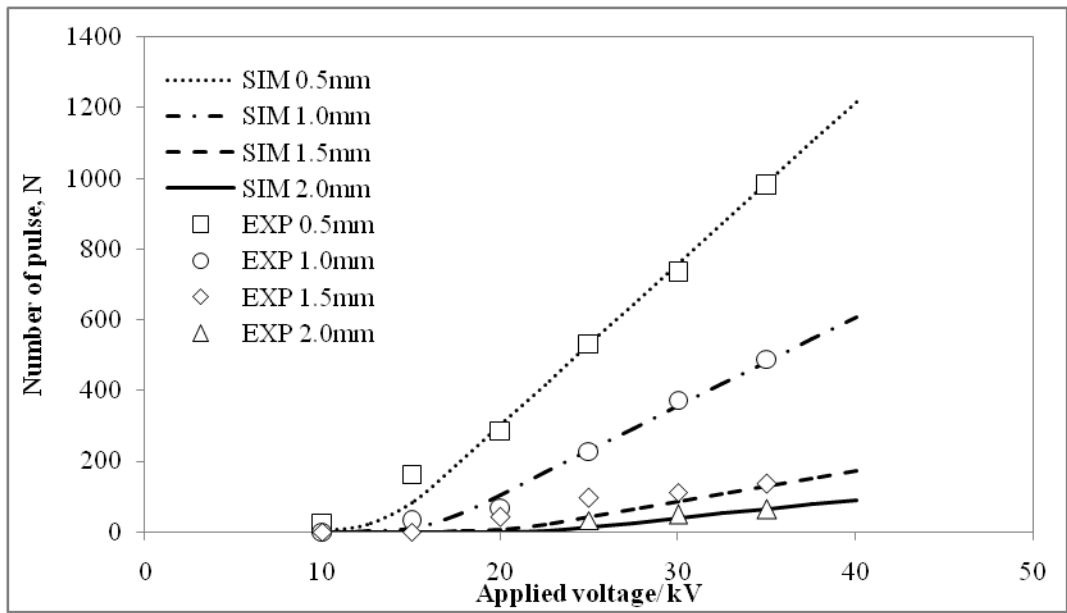


**Figure 3.13:** Comparison of the experimentally detected number of pulses with the simulated results.

In conclusion, it has been shown that the proposed empirical distribution function is able to predict the experimental distribution function for the current pulse amplitudes and the occurrence of the transition regime of the pulse distribution. Besides, this model improves our understanding of the stochastic behaviors of DBD. This will also improve our ability to design the DBD discharge for effective operation and applications.

### 3.3 Discharge Energy Consideration

#### 3.3.1 Observation of experimental QV Lissajous

For the study of the DBD electrical characteristic, the dissipation power is a very important parameter. However, the energy dissipation of individual filament cannot be directly measured from current and voltage signals because the time duration of the individual filamentary pulse is extremely short. Hence, the simplest method to

investigate dissipation power in DBD is the QV Lissajous method, which has been described in Chapter 2.

By plotting the charge versus applied voltage, a typical QV Lissajous has been obtained as shown in Figure 3.14. According to Manley's theory (Manley, 1943), the QV Lissajous obtained for filamentary mode DBD discharge has a parallelogram structure as shown in Figure 3.14 (dotted line). However, the experimental QV Lissajous obtained in our experiment is not following the parallelogram structure and a significant width expansion has been observed.

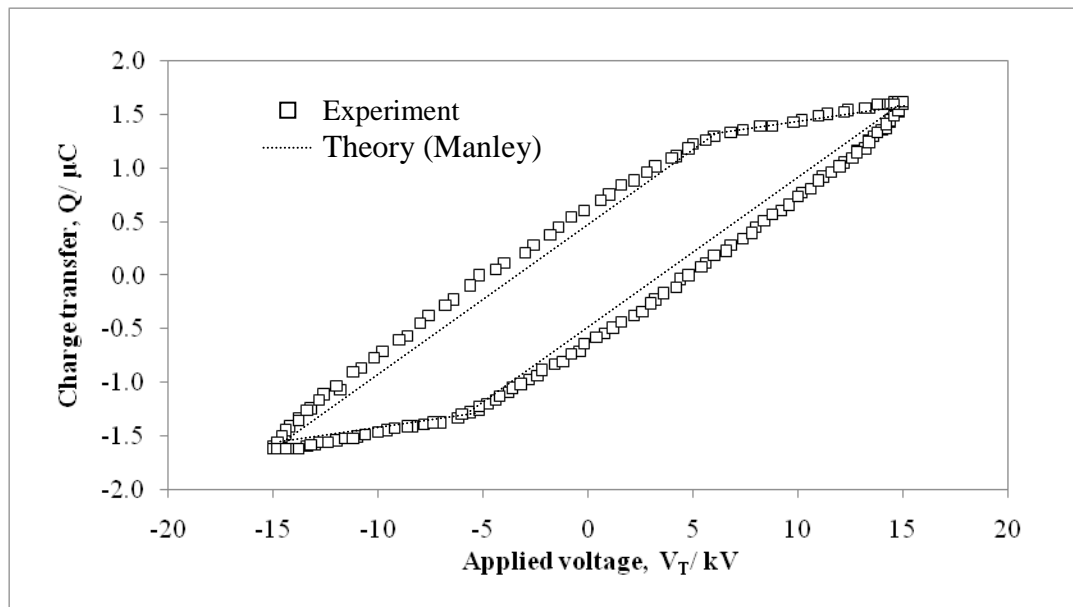


**Figure 3.14:** The experimental and theoretical QV Lissajous figure.

According to Manley's theory, the breakdown voltage across the air gap is considered constant and it does not depend on the applied voltage waveform. Possible leakage of current at the surface of the DBD was not considered. In our case, we assume that the dielectric surface has high surface resistance.

Kriegseis et. al. has compared the QV Lissajous of volume discharge with that of surface discharge (Kriegseis et. al. 2011). They found that the energy consumed is sum of the volume discharge and surface discharge. The parallelogram QV Lissajous is mainly caused by volume discharge and can be accurately predicted by Manley's theory (Manley, 1943), whereas the distorted slope of the QV Lissajous during the discharge 'ON' mode is caused by the surface discharge. Hence, we are suggesting that the width expansion of the QV Lissajous is attributed to the surface resistance effect on the dielectric surface. The existence of the surface resistance on the dielectric is resulting in the non-uniform charge distributed on the dielectric surface. It gives rise to a potential difference between the discharge region and the non-discharge region.

During the discharge "ON" mode, the voltage across the gap at the discharge region can be considered constant. However, the voltage across the gap at the non-discharge region is increasing and is corresponding to the applied voltage. The rise of the average gap voltage is mainly due to the rise of gap voltage at the non-discharge region.

The breakdown voltage  $V_b$ , which is determined from the experimental QV Lissajous, is found to be dependent on the external applied voltage. According to the surface resistance model, the rise of breakdown voltage determined from QV Lissajous can actually be attributed to the leakage of memory charge from the discharge region to the non-discharge region. Higher applied voltage leads to more leakage of memory charge. Therefore, higher applied voltage is required for the DBD ignition during the next half cycle.

The width expansion of the QV Lissajous has can be correlated to the applied voltage. However, the average gradient of the QV Lissajous determined during the “ON” period still corresponds to the dielectric capacitance.

### 3.3.2 The dynamic electrical circuit model

The dynamic circuit model developed to simulate the DBD discharge consists of active circuit elements as shown in Figure 3.15. Each of the microchannels in the space gap is modeled by a voltage-control current source and a capacitor connected in parallel, while the non-discharge region is represented by a single capacitive current. These microchannels when met on the dielectric surface are connected via a resistor representing the surface resistance  $r_{sf}$ .

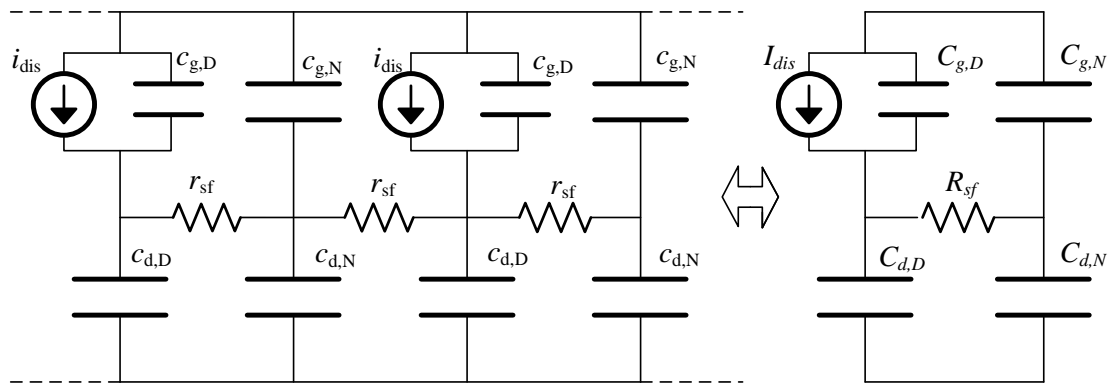


**Figure 3.15:** The equivalent circuit for filamentary discharge with surface resistors.

This electrical circuit can be simplified by combining all the microchannels in the discharge region and the non-discharge region separately as shown in Figure 3.16. The discharge region is modeled by a resistive current and a capacitor connected in parallel to represent the whole discharge region, while the whole non-discharge region is represented by a single capacitive current. A resistor on the dielectric surface

representing the surface resistance  $R_{sf}$  is inserted to separate the two regions. The surface resistance introduced here represents a lump circuit element that accounts for the trapping energy (Bartnikas, Radu, & Wertheimer, 2007; Li, Li, Zhan, Xu, & Wang, 2008; Somerville & Vidaud, 1985) that resists the flow of charges on the surface and also the conductivity attributed to memory charge on the dielectric surface. The surface resistance is also related to the ratio of the area of discharging regions to the total area.

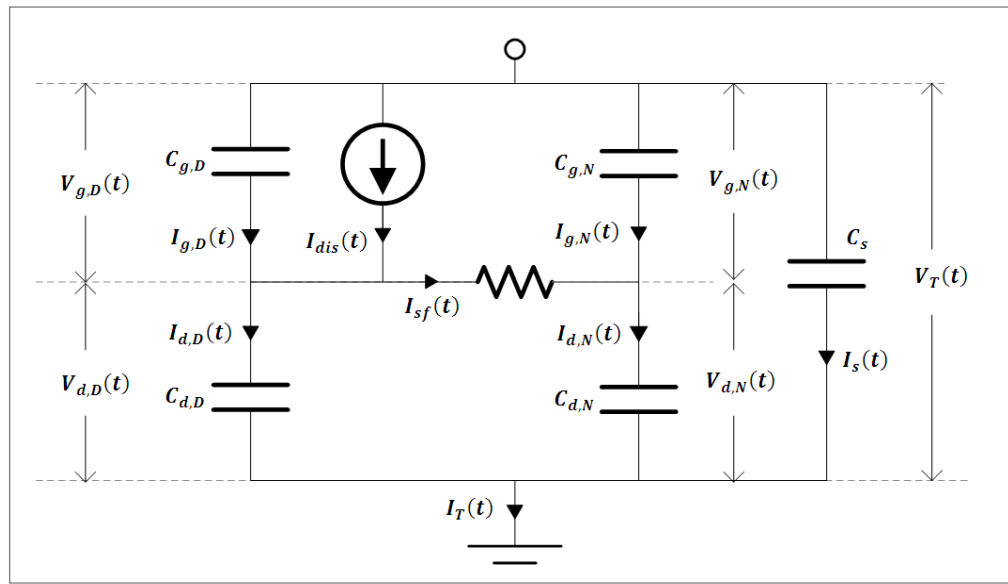


**Figure 3.16:** The electrical model of DBD and the dynamic currents in equivalent circuit.

The ratio of the total area of the discharging regions to the total area of the electrodes is written as,  $D$ , which is given by:

$$D = \frac{\sum S_k}{S} \quad (3.21)$$

where  $S$  is the total area of the electrode,  $\sum S_k$  is the total area occupied by all the microdischarges. Factor  $D$  was obtained experimentally by imaging the discharge through a transparent indium-tin oxide (ITO) electrode. Meanwhile, the surface resistance can be determined by simulation.

The discharge current is strongly dependent on the space voltage of the discharge region. Representing the DBD discharge as a voltage controlled current source (Naude, et al., 2005) , the average current can be expressed by:

$$I_{dis}(t) = I_o \left( \frac{V_{g,D}(t)}{V_{nb}} \right)^\beta \quad (3.22)$$

where  $V_{nb}$  is the breakdown voltage and it is a constant value. The values of  $\beta$  and  $I_o$  are dependent on the operating condition. This approach has been used by Flores-Fuentes et al (Flores-Fuentes, et al., 2009) in their electrical model. This equation is only used as a DBD “ON” and “OFF” switch of the reactor in order to simplify the electrical circuit modeling.

The generated discharge current is flowed into the discharge region. The deposited charge on the dielectric surface creates an unbalanced voltage between the discharge region and non-discharge region on the dielectric surface. The voltage difference between the discharge region and the non-discharge region gives rise to a resistive current on the surface (Somerville & Vidaud, 1985).

The distribution of charges in a DBD essentially extends from the discharge channel to the surface of the dielectric. This effect is more apparent in low frequency discharge such as 50 Hz as there will be sufficient time for the charges to spread on the dielectric surface. This effect has investigated by Akishev (Akishev et al., 2011), where a microdischarge channel was singled out in the modeling. Akishev defined the surface discharge as surface plasma progresses as a surface resistance (Akishev et al., 2011). The current is dependent on the voltage difference between the discharge region and the non-discharge region. In the present model, we fit the surface discharge resistance in the current equation as:



$$I_{sf}(t) = \frac{V_{d,D}(t) - V_{d,N}(t)}{R_{sf}} \quad (3.23)$$

where  $R_{sf}$  is equal to the total effective resistance of the charge surface progresses. The total equivalent current obtained by numerical method multiplies the total voltage calculated from voltage distortion equation is integrated to give the dissipation energy. The total dissipation energy of DBD system in one cycle is written as:

$$E_{Total} = \int_0^T V_T(t) I_T(t) dt \quad (3.24)$$

The energy consumed by the surface resistance in one cycle is:

$$E_{surface} = \int_0^T \frac{(V_{d,D}(t) - V_{d,N}(t))^2}{R_{sf}} dt \quad (3.25)$$

and the energy of the DBD discharge in one cycle is:

$$E_{DBD} = E_{Total} - E_{surface} \quad (3.26)$$

The total energy ( $E_{Total}$ ) calculated from the experimentally measured QV Lissajous is equal to the sum of energy of the surface resistance ( $E_{surface}$ ) and the DBD discharge ( $E_{DBD}$ ).

### 3.3.3 Factor $D$ determination

The DBD reactor has been modified for the experiment to capture the image of the discharge from the top view of the DBD reactor. An ITO layer mounted with a ring shape electrode replaced one of the original electrodes. The exposure time of the camera was adjusted to 5 seconds. The captured image was the superposition of five images to obtain a good ratio of filament emission to background noise.

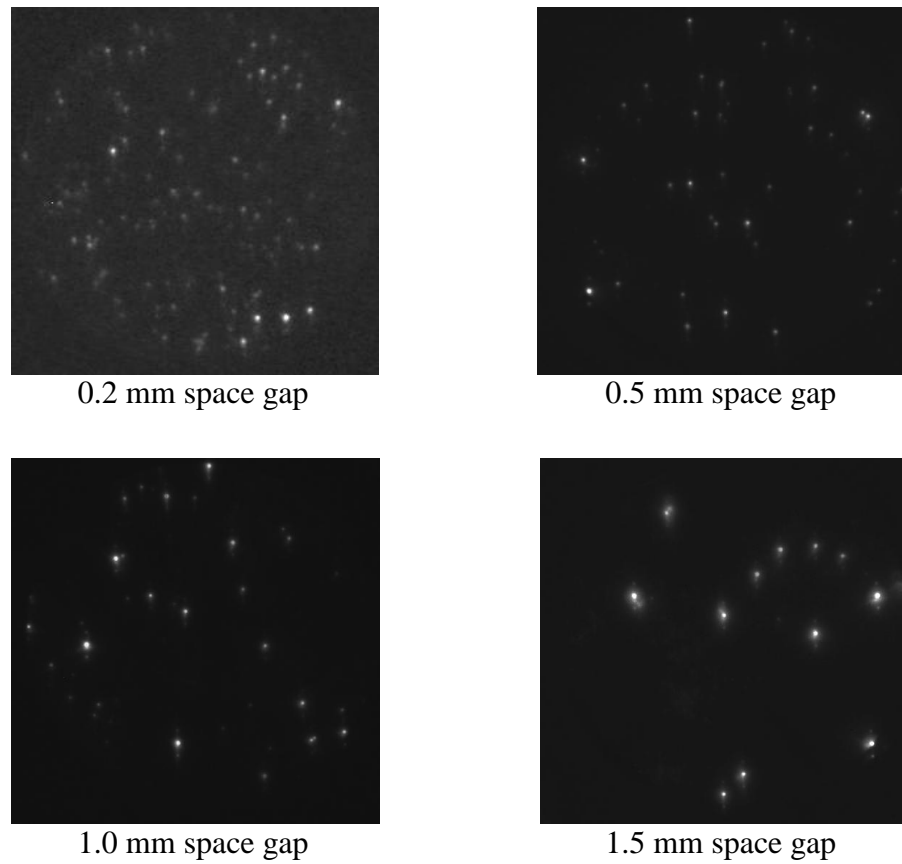


**Figure 3.17:** The image from top view of DBD discharge.

Based on the intensity of the filamentary discharge emission, the factor  $D$  is obtained by adjusting the contrast level and the image is analyzed by using the Matlab image processing function within the Matlab code. In this method, the image is converted to a matrix corresponding to the pixels. The higher intensity pixel is represented by value 1 in the matrix, while lower intensity pixel is represented by value of 0. The ratio factor  $D$  can be obtained by summation of the value in the matrix divided the total number of pixels occupied by the electrode area.

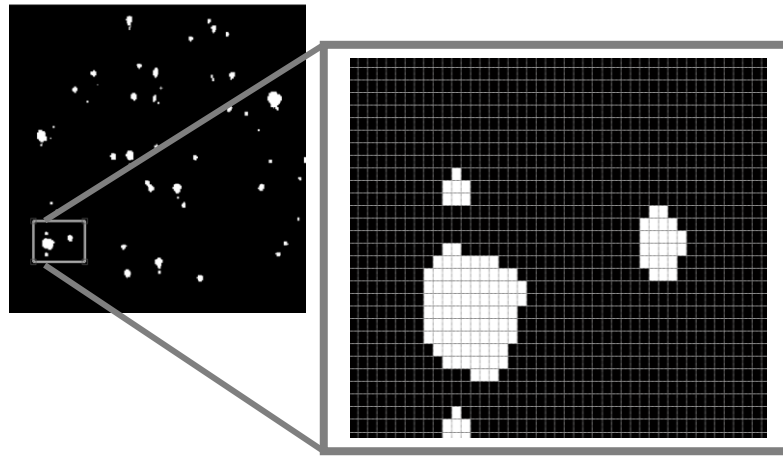


**Figure 3.18:** The process to convert the image file to matrix format. The black color represents zero value and white color represents value 1.

The factor  $D$  can be expressed as below:

$$D = \frac{\text{Total number of pixels represents value 1}}{\text{Total number of pixels of the eletrode area}} \quad (3.27)$$

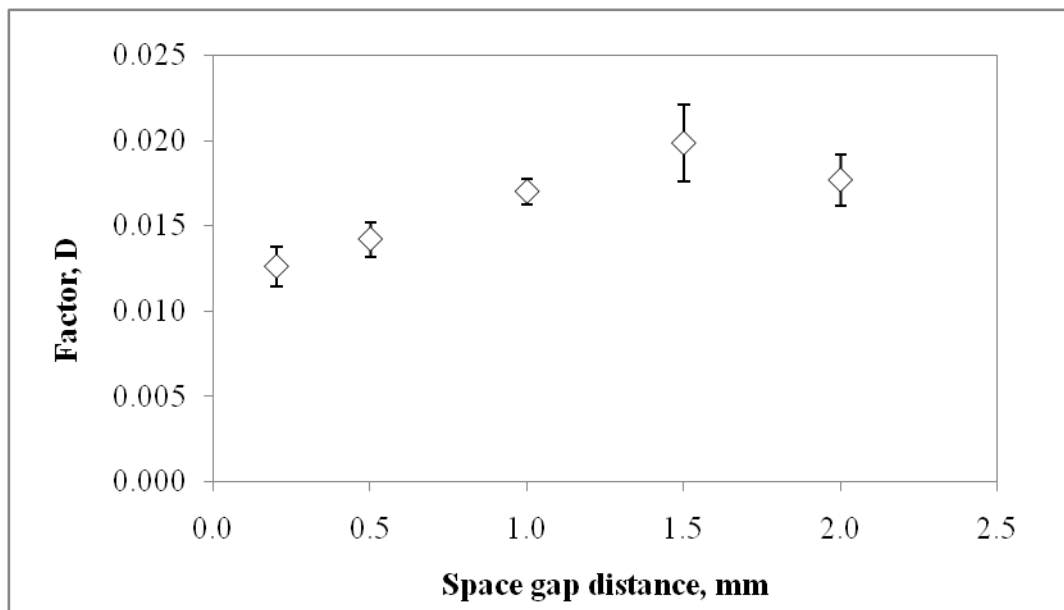


**Figure 3.19:** The variation of factor  $D$  for discharges with various space gaps distance.

The factor  $D$  is found to be increasing with the space gap. This is because the size of the individual filament is also increasing with increase of space gap. However, the number of the microchannels decreases with the space gap. The error of factor  $D$  determination may be due to the low intensity of the light emission of the microchannel. The size and the number of filaments can be larger than the calculated value due to the lower light emission from the filaments and the number of filaments captured by the camera can be less than the actual number.

### 3.3.4 Matlab Simulink code

The dynamic circuit model is implemented by using Matlab Simulink. The arrangement of the circuit elements in Simulink code is shown in Figure 3.20. The discharge current and voltage used for the simulation are registered. An AC voltage source at 50 Hz is employed as the power source, where the inductance of the power transformer is ignored.

The surface current is simulated according to Equation 3.23 and the simulation code is shown in Figure 3.20. Meanwhile, the discharge current signal is registered according to Equation 3.22 and the simulation code is shown in Figure 3.21 (a). The voltage registered between the IN and OUT of the voltage measurement block represents the space gap voltage of the discharge region,  $V_{g,D}$ . The signal from this voltage measurement block is sent to the analysis block.

The voltage across the DBD reactor and the equivalent current measured experimentally can be compared with the simulated output. Other measurable and simulated quantities compared include the dissipated power, voltage across the space gap and dielectric. Hence, in order to compare with experiment results, the current and

voltage registered in Simulink are sent to the analysis block via input IN1 and IN2 respectively. The analysis code is shown in Figure 3.21 (b). By employing the Equations 3.24, 3.25, and 3.26, the simulated energy is compared with experimental results.

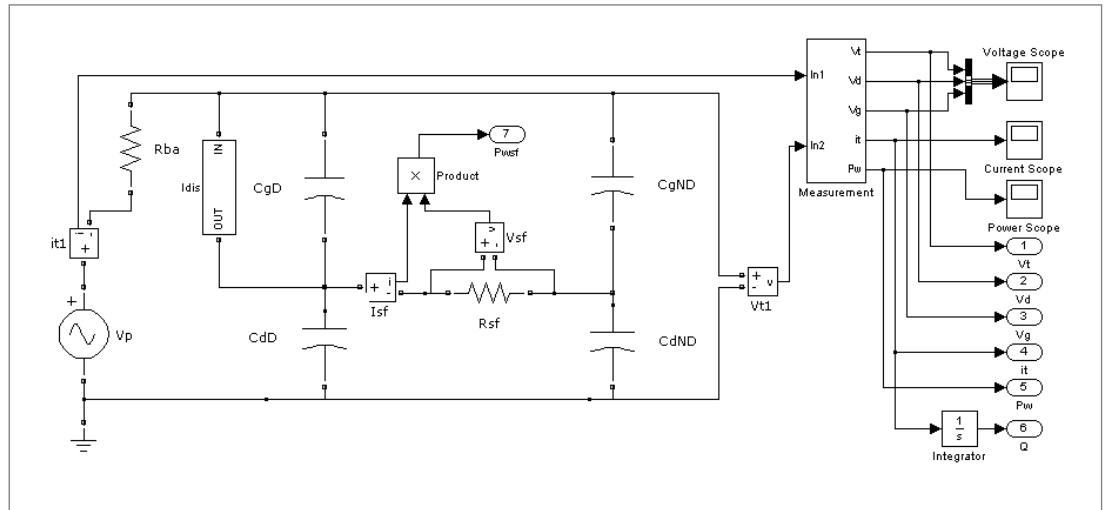


**Figure 3.20:** The interface of Matlab Simulink code.

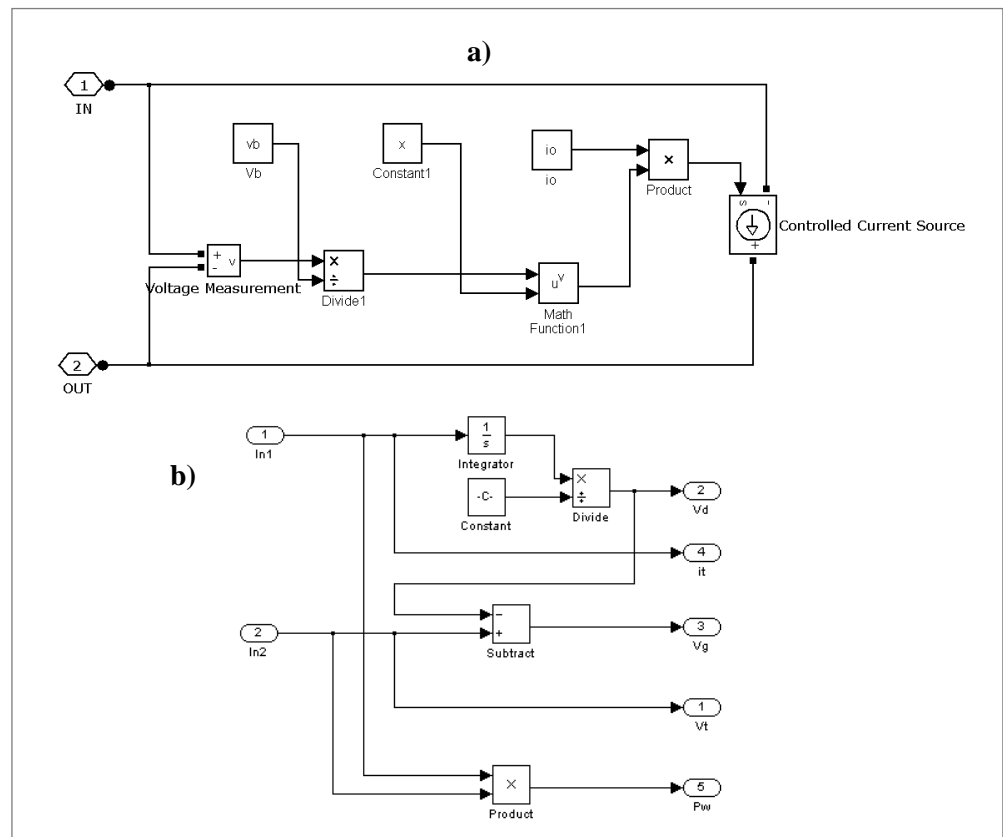


**Figure 3.21:** The Simulink codes of (a) discharge current block, and (b) measurement analysis block.

### 3.3.5 Results and discussions

A typical set of experimental results and simulated results are presented in Figure 3.22 for DBD with 0.5 mm air gap and 30 kV applied voltage. The simulated results are in good agreement with the experimental results.

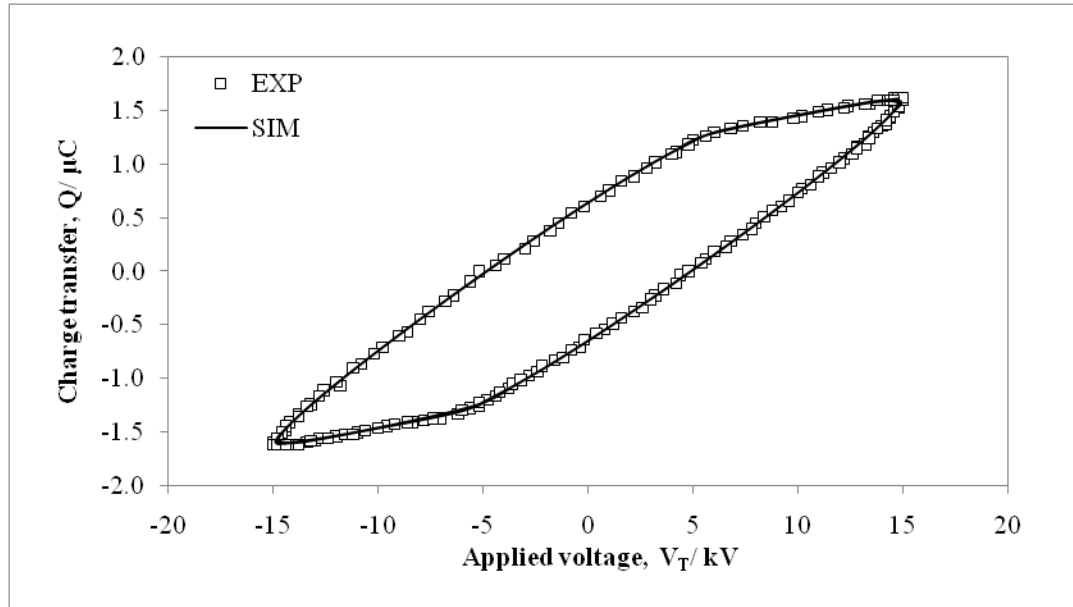


**Figure 3.22:** The comparison between the experimental result and simulated result.

The rate of change of the charge transfer measured across the charge measurement capacitor as shown in Chapter 2, Figure 2.2 gives the average total currents, while the instantaneous power dissipated by the discharge across the air gap can be obtained by multiplying the total current by the voltage of the air gap. Figure 3.23 shows the comparison of simulated and experimental values of the dissipated power and the total current for a discharge with 0.5 mm air gap and 30 kV pk-pk applied voltage. The simulated results are used to plot the QV Lissajous and compared to that obtained experimentally. The Factor  $D$  was determined based on experimental imaging as described earlier. In order to fit the QV Lissajous plotted from the experimental results, a suitable value of surface resistance  $R_{sf}$  is introduced. The resistor representing the

surface resistance  $R_{sf}$  is determined by fitting the computed QV Lissajous from the simulation output with the experimentally obtained QV Lissajous.

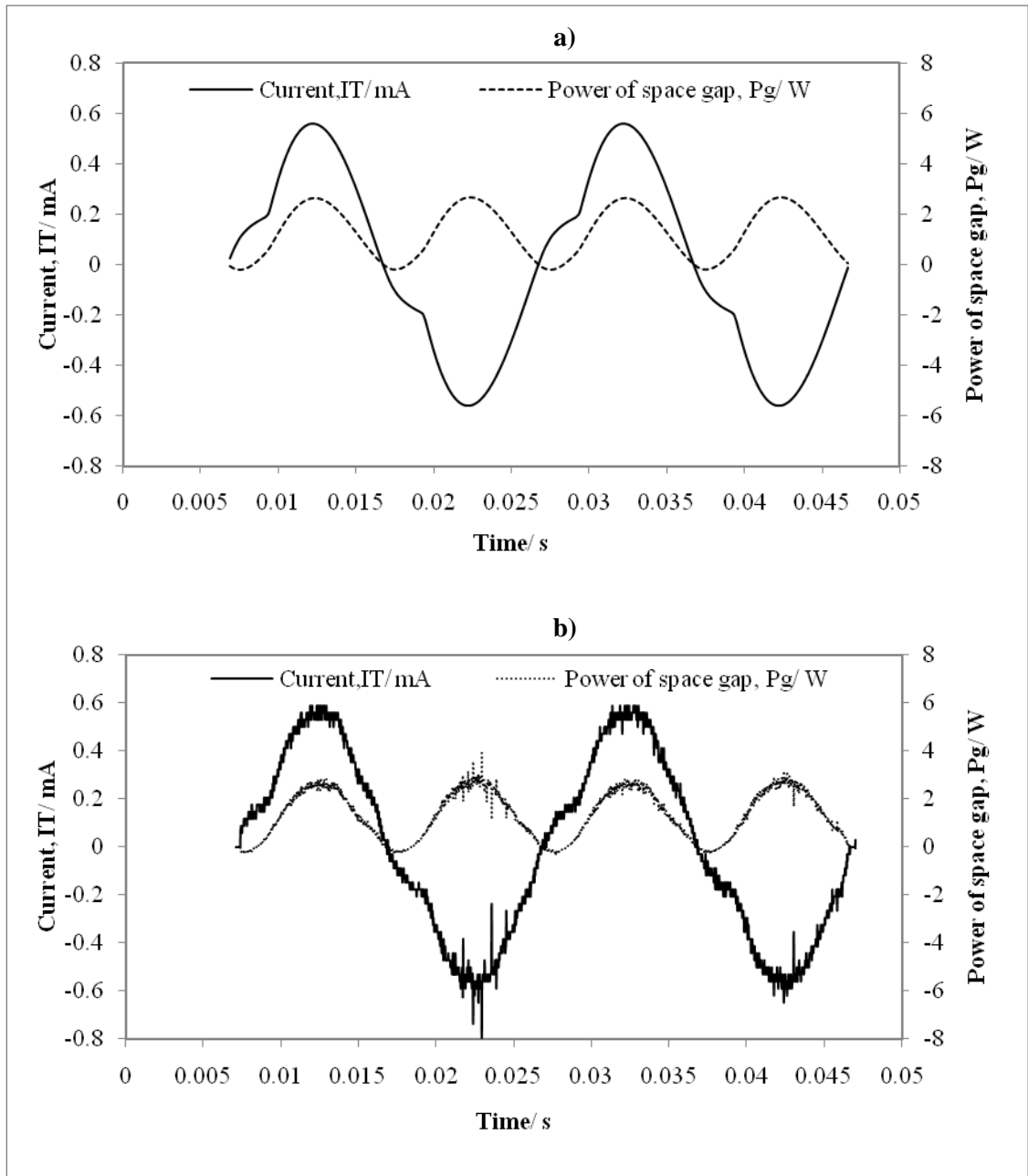


**Figure 3.23:** Comparison of (a) simulated and (b) experimental waveforms of the dissipation power of space gap and the total current for discharge with 0.5 mm air gap and 30 kV pk-pk applied voltage.

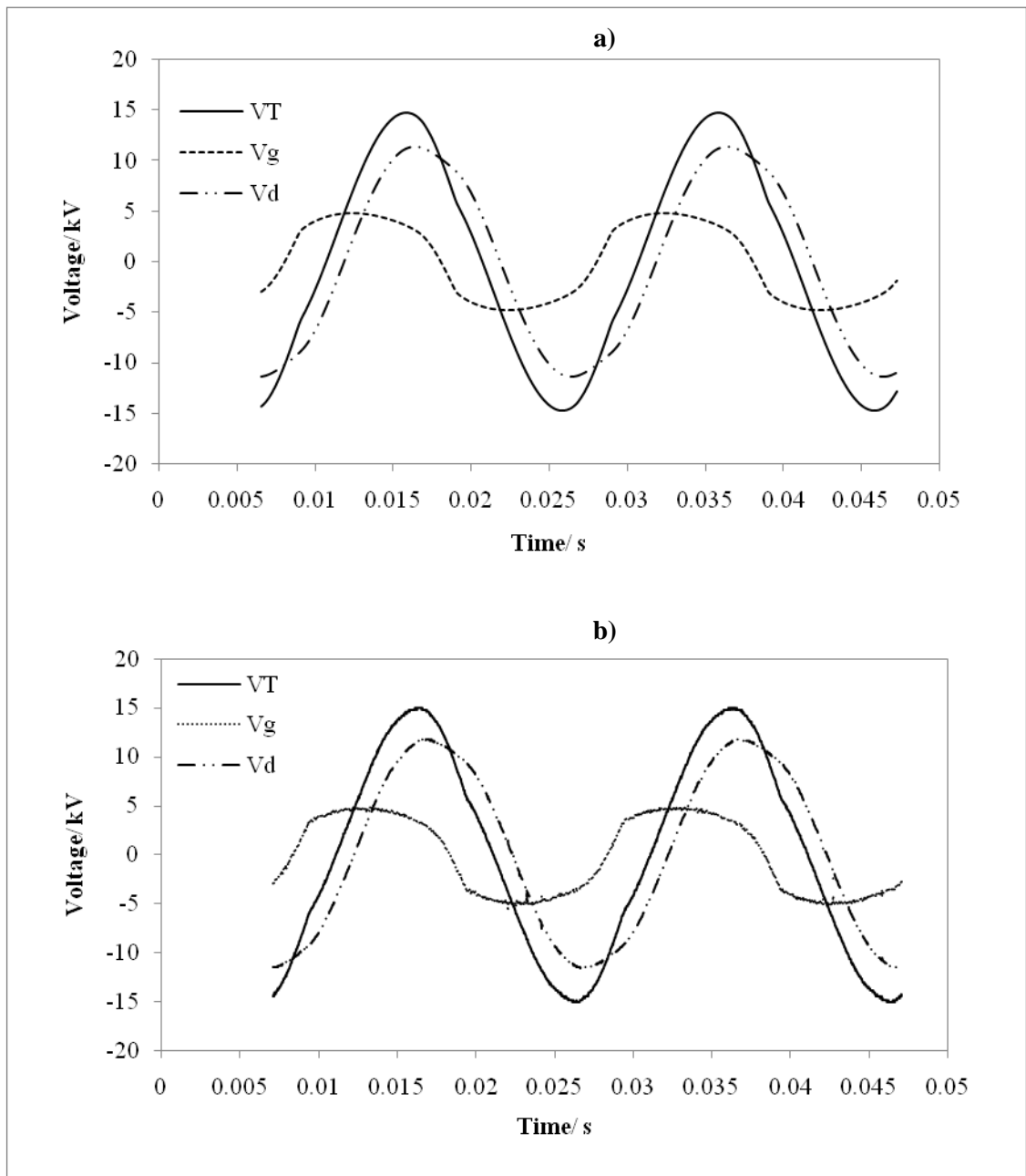


**Figure 3.24:** Comparison of (a) simulated and (b) experimental waveforms of the applied voltage  $V_T$ , air gap voltage  $V_g$ , and dielectric voltage  $V_d$  for discharge with 0.5 mm air gap and 30 kV pk-pk applied voltage.



These procedures are repeated for DBD with applied voltages of 10 kV to 35 kV, and space gaps of 0.2 mm, 0.5 mm, and 1.0 mm. The effect of the surface resistance is correlated to the surface roughness of the dielectric layer. Two types of dielectric layers (glass plates), one of rough surface and one of smooth surface, have been studied.

For DBD with 0.2 mm air gap, with the smooth glass as the dielectric layer, the suitable value of surface resistance is found to be 2.1 M $\Omega$  for all the applied voltages. The QV Lissajous obtained from the simulated results with this value of the surface resistance show almost perfect match with the QV Lissajous obtained experimentally. The QV Lissajous plotted with applied voltages of 10 kV to 35 kV are shown in Figure 3.25. When the space gap is increased to 0.5 mm and 1.0 mm, the effective surface resistance required to give the observed QV Lissajous is found to be 2.3 M $\Omega$  and 1.0 M $\Omega$  respectively. The results for 1.0 mm air gap are shown in Figure 3.26. The results suggest that the effective surface resistance is also affected by the thickness of the air gap. This is due to the fact that in a very thin gap, the microdischarges are regularly distributed on the dielectric surface due to repulsion between the nearby microdischarge channels and the repulsive force limits the mobility of the deposited charges on the dielectric surface. Particularly, the density of the deposited memory charge on the dielectric surface is inversely proportional to the dielectric surface resistivity. The total memory charge deposited by one microdischarge is relatively low for smaller air gap as compared to that for larger air gap. Hence, the effective surface resistance  $R_{sf}$  obtained for smaller air gap is higher than that of larger air gap.

The QV Lissajous also shows significant expansion when the applied voltage is increased from 10 kV to 35 kV. The energy dissipated, which is indicated by the area of the respective QV Lissajous is observed to increase with the applied voltage. The higher energy dissipation is beyond what is given by Manley's equation, but can be accurately determined with our model. The additional energy dissipated is closely related to the surface resistance as energy is consumed during charge transfer from the discharge region to the non-discharge region through the surface resistance.

The results obtained with smooth dielectric surface can be compared with the rough dielectric surface. The experiment with space gap of 1.0 mm is repeated but with a rough dielectric surface for applied voltage of 10 kV to 35 kV. The surface resistances obtained for rough dielectric surfaces are significantly higher. The effective surface resistance of the rough dielectric surface is determined as 4.5 M $\Omega$ , compared to that obtained with the smooth dielectric surface which is 1.0 M $\Omega$ . Figure 3.27 shows the QV Lissajous obtained from simulation with surface resistance of 4.5 M $\Omega$  which matches well with the experimentally obtained QV Lissajous for air gap of 1.0 mm.

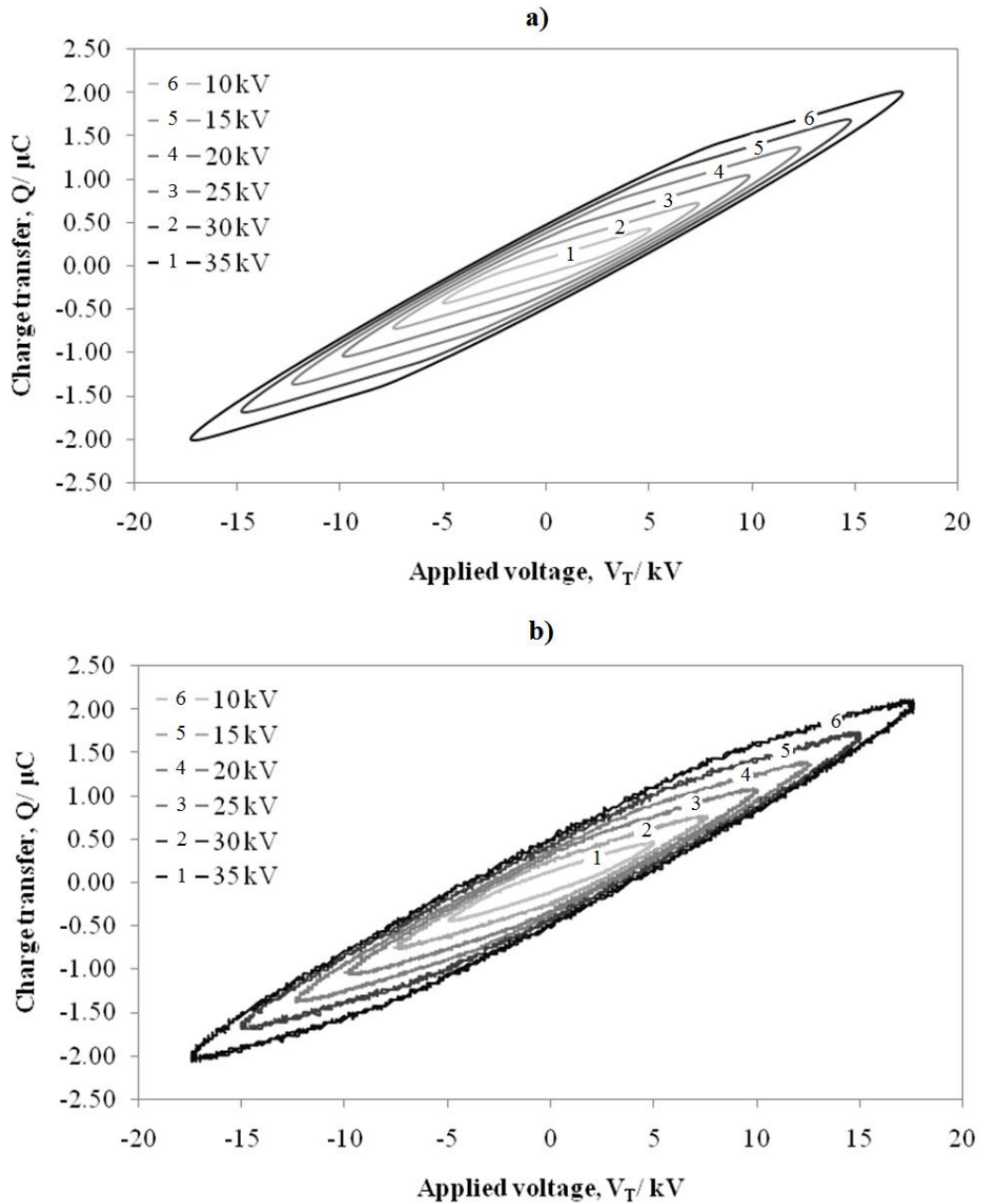


**Figure 3.25:** QV Lissajous resulting from (a) simulation and (b) experiment for 0.2 mm air gap and various applied voltages when factor  $D$  and surface resistance are 0.013 and 2.18 M $\Omega$  respectively.

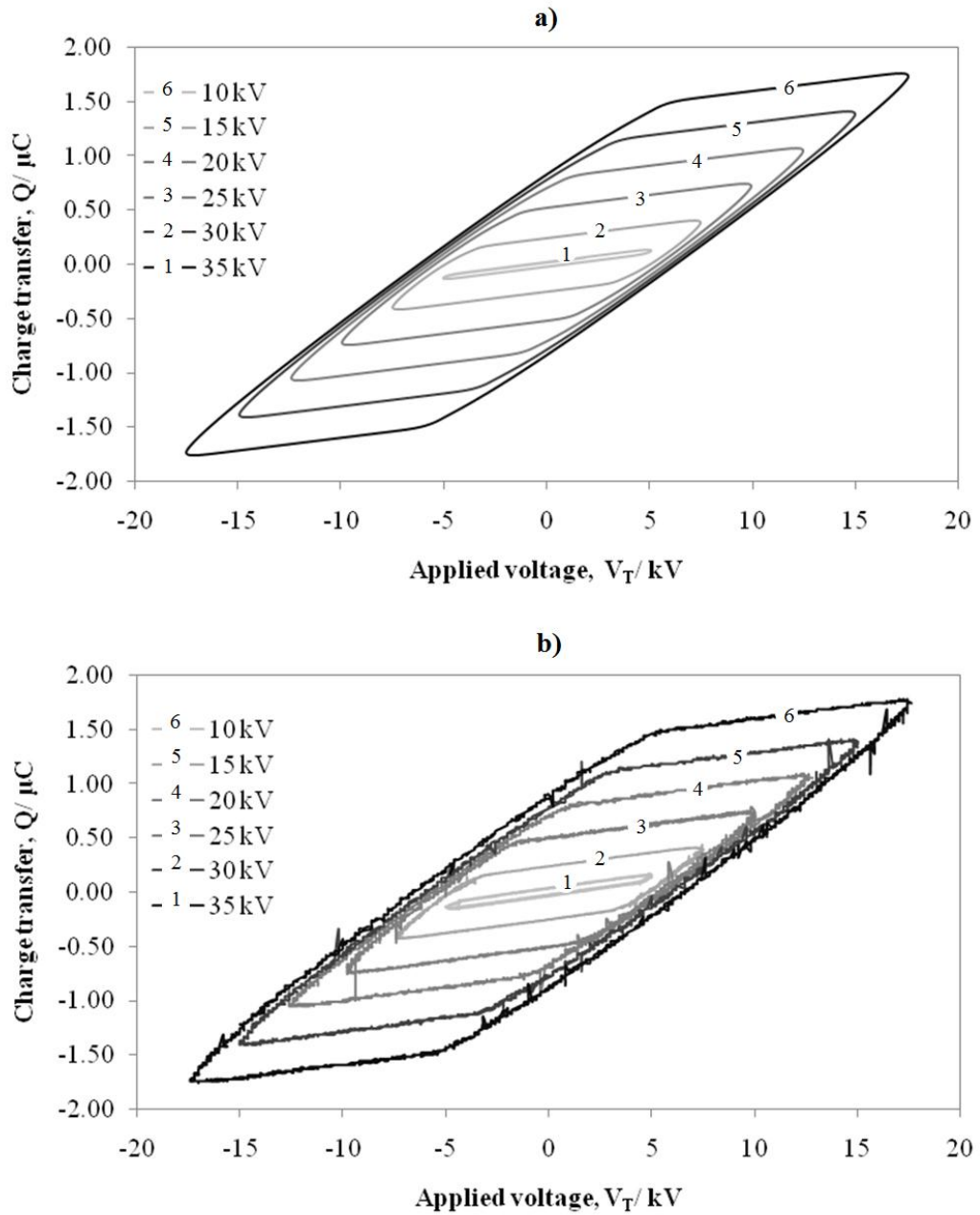


**Figure 3.26:** QV Lissajous resulting from (a) simulation and (b) experiment for 1.0 mm air gap and various applied voltages when factor  $D$  and surface resistance are 0.014 and 2.3 M $\Omega$  respectively.

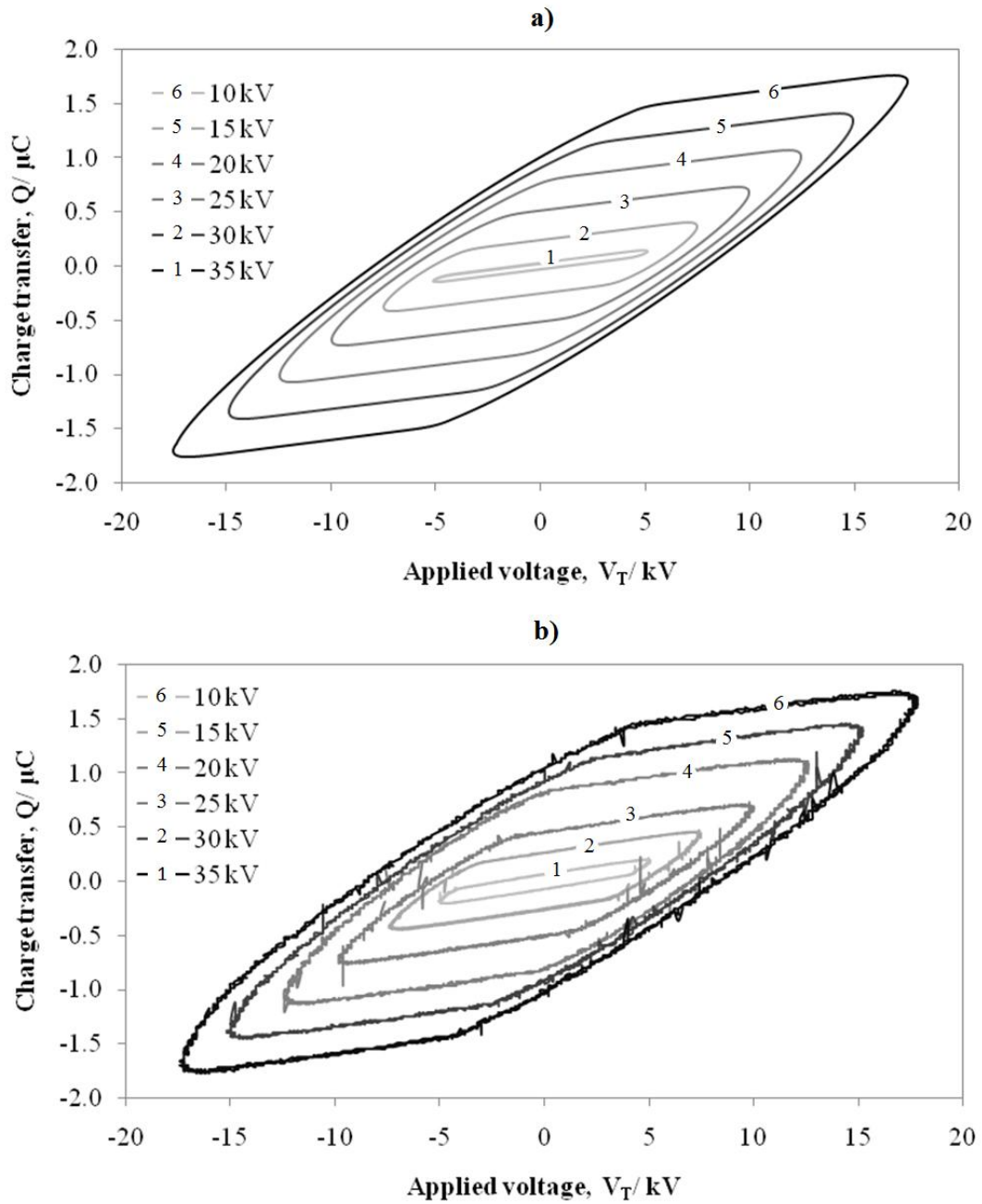


**Figure 3.27:** QV Lissajous resulting from (a) simulation and (b) experiment for 1.0 mm air gap and rough dielectric surface when factor  $D$  and surface resistance are 0.017 and 4.5 M $\Omega$  respectively.

The total energy consumed in the DBD for one complete cycle can be calculated based on Equation 3.24 or determined from the area under the QV Lissajous. The values obtained from the QV Lissajous based on experimental data are plotted as points in Figure 3.28 for all the applied voltages and discharge gaps. Calculated values are plotted in the same figure for comparison. The experimental points are found to be in good agreement with the calculated curves. The results obtained from our model for all the experimental parameters are summarized in Table 3.2. The value of factor  $D$  used is estimated as discussed earlier.

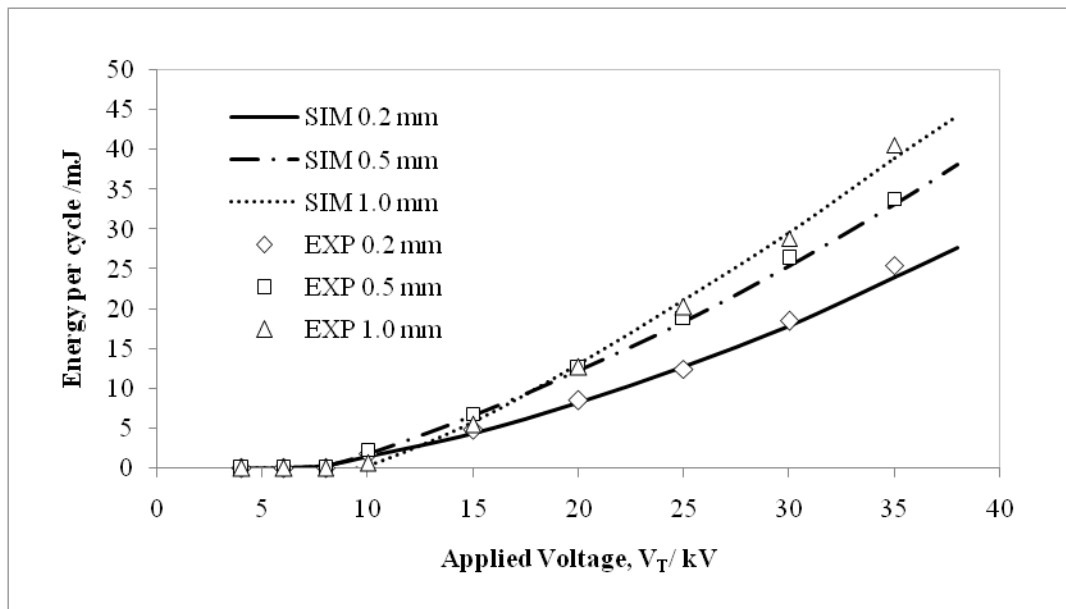


**Figure 3.28:** The total energy dissipated versus the applied voltage for DBD with various air gaps. The lines represent the simulated results and the symbols represent the experimental results.

**Table 3.2.** List of the parameters used in the simulation.

| <b>Glass plate</b> | <b>Space gap</b>    | <b>Factor,</b>  | <b>Surface</b>                     | <b>Dielectric</b>         | <b>Space gap</b>          |
|--------------------|---------------------|-----------------|------------------------------------|---------------------------|---------------------------|
|                    | <b>distance/ mm</b> | <b><i>D</i></b> | <b>resistance,</b>                 | <b>capacitance,</b>       | <b>capacitance,</b>       |
|                    |                     |                 | <b><math>R_{sf}/M\Omega</math></b> | <b><math>C_d/F</math></b> | <b><math>C_g/F</math></b> |
| <b>Smooth</b>      | 0.2                 | 0.013           | 2.1                                | 1.39E-10                  | 1.42E-10                  |
|                    | 0.5                 | 0.014           | 2.3                                | 1.39E-10                  | 5.70E-11                  |
|                    | 1.0                 | 0.017           | 1.0                                | 1.39E-10                  | 2.85E-11                  |
| <b>Rough</b>       | 1.0                 | 0.017           | 4.5                                | 1.48E-10                  | 2.85E-11                  |
| <b>surface</b>     |                     |                 |                                    |                           |                           |

The total capacitance as measured from the gradient of the QV Lissajous remains about the same with different applied voltages at consecutive cycles. This indicates that during the DBD OFF period, charges remain on the dielectric surface and contribute to the memory effect. Otherwise, if the remaining charges recombine on the dielectric surface during the DBD OFF period, the QV Lissajous will reflect the change in total capacitance in the gradient of QV Lissajous.

By having the experimental results accurately fitted with the simulated results from the model, we can calculate the efficiency of the discharge in term of the power dissipation at the DBD. The total energy represents the sum of the energy consumed by the discharge and the energy dissipated on the surface of the dielectric. Thus, the energy efficiency is high for smooth surface, which has low effective surface resistance. The efficiency of the discharge with air gap 0.2 mm, 0.5 mm and 1.0 mm at applied voltage of 10 kV to 35 kV are plotted in Figure 3.29 (a,b,c,d). The efficiency for discharge with 0.5 mm air gap, for example, at applied voltage of 10 kV is 94.6% but it is reduced to

70.1% for 35 kV discharge. Similar trend is shown for 0.2 mm and 1.0 mm air gap. The reduction at higher applied voltage can be explained by the fact that more energy is dissipated in the charge spreading process on the dielectric surface when the applied voltage is much higher than the breakdown voltage.

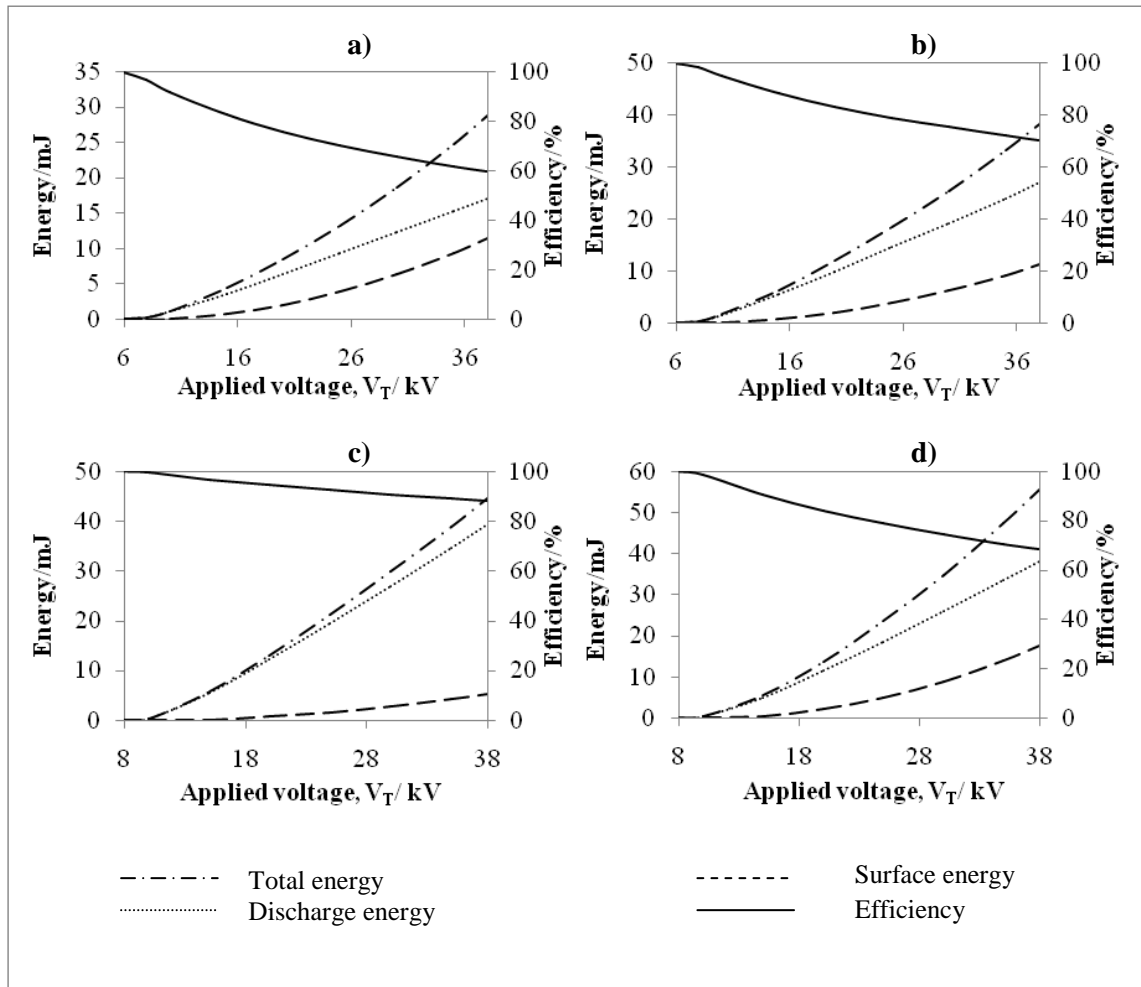


**Figure 3.29:** The simulated total energy, discharge energy, surface energy, and efficiency versus the applied voltage for smooth dielectric with (a) 0.2 mm air gap, (b) 0.5 mm air gap, and (c) 1.0 mm air gap. For rough dielectric with 1.0 mm air gap the results are shown in (d).



The dynamic circuit model constructed with Matlab Simulink has been shown to be able to accurately simulate the discharge energy of a 50 Hz filamentary discharge. This electrical model can be used to determine the optimum condition for DBD. According to this model, the efficiency of the DBD has been found to be higher with a smooth surface and low effective surface resistance compared to a rough surface. The efficiency reduces when the applied voltage is increased.

# Chapter 4: Conclusion and Suggestion for Future Work

## 4.1 Conclusion

The DBD can be used for generating non-equilibrium plasma under atmospheric air. As compared to the other types of gas discharge, the simplicity in the configuration and absence of the vacuum system of the DBD are obvious advantages for consideration of industrial applications. Hence, the DBD has attracted growing interest from many researchers for various potential applications in industry such as ozone synthesis, surface treatment, pollution control, production of excimer, flow control, and biomedical applications (see Chapter 1). Despite the industrial application of the DBD has a long tradition, many fundamental understanding of the device are still lacking. The problem of the stochastic behavior which may affect the usefulness the DBD, for example, is one of the challenges facing the researcher. In this project, we have put in considerable efforts to study this fundamental phenomenon.

According to the experimental results, the non-uniform breakdown voltage on the dielectric surface is suggested to be one of the stochastic factors. Theoretically, the higher breakdown voltage, the higher discharge pulse can be generated. The local breakdown voltage is determined by the distance of the space gap and the local properties of the electrode surface. Therefore, the breakdown voltage of each channel is randomly varied according to the local electrode surface properties, thus generating a discharge pulse with certain pulse height, which is different from other channels.

Based on the theoretical calculation of the local total charge transfer for the discrete volume, the number of the pulses generated in the local channel can be predicted (see chapter 3). By combining all the channels, we propose the empirical equation for the pulse height distribution.

This empirical equation can successfully predict the existence of two discharge regimes, which has been observed from the experimental results. By using the proposed empirical equation, the ratio of the impulsive current and non-impulsive current can be validated from the experimental results. The increase in the ratio of charge transported by the impulsive discharge for discharge with larger air gap is believed to be caused by the increase of the impulsive discharge in larger air gap.

Besides, this distribution function obtained will allow us to predict the distribution of the current pulses of the discharge, thus improving our ability to control the DBD discharge. The increase in the applied voltage will increase both the number of the current pulses and the current pulse amplitude in regime 1. However, the amplitude of the current pulse is found to be saturated when the applied voltage is increased in regime 2 (see Chapter 3). This empirical equation can be used in the design of the DBD system. For the production of higher pulse amplitude, the DBD is suggested to have a larger space gap rather than a higher applied voltage.

For the energy investigation, the dynamic circuit model constructed with Matlab Simulink has been found to be able to accurately simulate the energy dissipated by a 50 Hz filamentary discharge. The surface resistance introduced in this electrical model represents the average effect that effectively accounts for the resistance encountered by the charges that flow between the discharging and non-discharging regions on the

dielectric. The surface resistance is believed to be contributed by the surface roughness of the dielectric layer, the trapping energy and the memory effect. The factor  $D$  was obtained experimentally before the determination of the surface resistance. The values of surface resistance are found to be dependent on the width of the air gap. In any case, the expanded QV Lissajous can be reasonably explained by the fact that the total energy is the sum of the of the DBD discharge energy and the energy consumed by the spreading of charges on the dielectric surface.

The efficiency of the DBD can be defined as the percentage of the energy consumed by the space gap to the total dissipation energy. By having the experimental results accurately fitted with the simulated results from the model, the efficiency of discharge can be obtained from the electrical modeling. The efficiency of the DBD has found to be higher with a smooth surface and low effective surface resistance compared to a rough surface. The efficiency reduces when the applied voltage is increased. This is because at higher applied voltage, more energy is dissipated in the charge transferred process on the dielectric surface as in this case the excess voltage is expected to be higher.

## **4.2 Suggestion of Future Work**

### **4.2.1 High-speed imaging**

The single DBD pulse lasted for only a few nanoseconds. By using a high-speed camera, the formation mechanism of a filamentary discharge can be investigated. One of the DBD behaviors of interest is the collective effect. The collective effect of DBD have been observed by Allegraud et al. (Allegraud, Guaitella & Rousseau, 2007), where more than one filamentary discharge can be generated in a single current pulse.

The high-speed intensified charge-coupled device (iCCD) camera can be used to investigate the collective effect of the filamentary discharge. The image of the synchronous breakdown across the discharge gap under the different configurations can be captured by the iCCD camera. The role of the memory charges in the formation of filamentary mode dielectric barrier discharge (DBD) can also be visualized. The mechanism of the electron avalanche happened in the direction from the dielectric surface towards the opposite electrode is believed to be different from that in the reverse direction. This can be explained by the existence of the memory charge on the dielectric surface, which supports the secondary emission effect on the dielectric surface. From the preliminary result, the synchronous breakdown in the discharge gap resulting in the capturing of three pulses corresponding to a single current pulse was observed as shown in the Figure 4.1. Further experiments can be carried out to investigate the phenomenon.



**Figure 4.1:** Image of the single negative current pulse in the 5 mm gap DBD captured by ICCD camera with gate width of 500  $\mu$ s. Three synchronous breakdowns were observed in a single negative discharge current pulse.

#### 4.2.2 Optical emission spectroscopy

The kinetics of the chemical reactions in the plasma is strongly dependent on the discharge temperature. The optical emission spectroscopy (OES) is a traditional diagnostic tool for the plasma temperature investigations. Particularly, this technique can be used for determining the energy of the gas particles from the plasma emission. The composition of the metastable and the discharge species can also be determined from the spectra. For the DBD operated under the atmospheric air, several band system of nitrogen can be observed as shown in Figure 4.2.

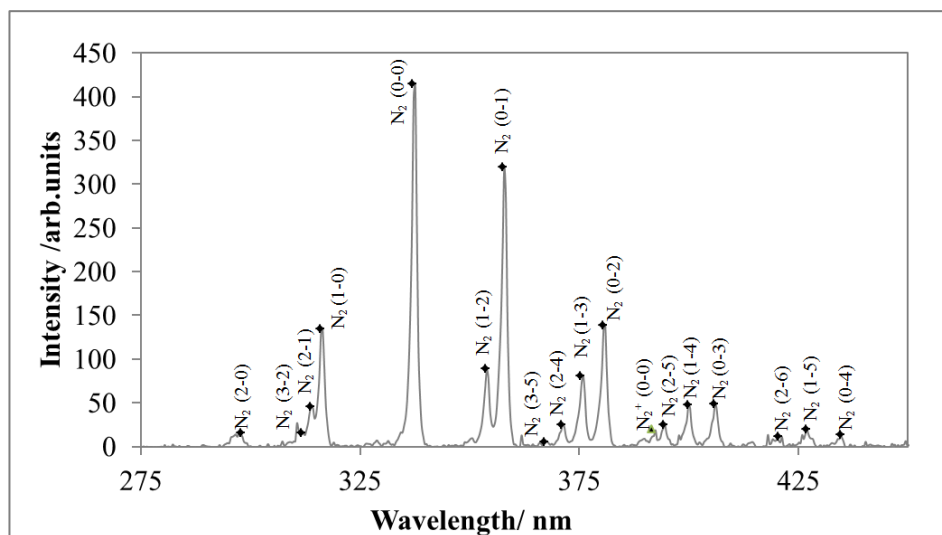


**Figure 4.2:** The DBD optical emission spectra under atmospheric gas.

In general, the DBD is not in local thermodynamic equilibrium. Therefore, the vibrational, rotational and translational temperatures may differ from each other. Since the vibrational mode exchanges energy with the electrons faster than the rotational and translational mode (Williamson & DeJoseph, 2003) the vibrational temperature is higher than the rotational and translational temperature.

The Boltzman plot method can be used for determining the vibrational and rotational temperature (Herzberg, 1957). The Franck-condon factor, which is related to the transition probability, is required for calculating the vibrational temperature. Lofthus and Krupenir (Lofthus, & Krupenir, 1977) had summarized the Franck-condon factor of nitrogen metastables thus allowing the calculation of the vibrational temperature and rotational temperature. Therefore, further study for the vibrational temperature and rotational temperature can be carried up for improving the understanding of kinetics of the chemical reaction in DBD.

#### **4.2.3 Homogenous discharge**

Under certain condition, the homogenous discharge can be generated in the atmospheric air (Massines, et al., 2009; Massines, et al., 2003). The homogenous discharge has drawn attention of many researchers as this type of discharge may be preferred for various applications (Zhang, Shao, Long, et al., 2010). A possible direction of future work can be the development of the homogenous DBD. However, there are still many challenges that need to be addressed. One of the important challenges is to improve the understanding of the transition between the homogenous discharge and filamentary discharge. Currently, the researchers still question the required condition and formation mechanism of the homogenous discharge. The study for the condition of

the transition from the filamentary discharge to homogenous discharge under atmospheric air can be a great interest for further study.

The transition from the filamentary discharge to homogenous discharge is affected by the frequency of the applied voltage or the voltage rise time. Therefore, either a frequency variable power supply or a nanosecond pulse generator can be constructed for developing a homogenous DBD system. The comparison of the filamentary discharge and the homogenous discharge for the application, such as surface treatment, can be conducted experimentally.



## References

- Akishev, Y., Aponin, G., Balakirev, A., Grushin, M., Karalnik, V., Petryakov, A., & Trushkin, N. (2011). 'Memory' and sustention of microdischarge in a steady-state DBD: volume plasma or surface charge?\*. *Plasma Source Science and Technology*, 20(2), 024005.
- Allegraud, K., Guaitella, O., & Rousseau, A. (2007). Spatio-temporal breakdown in surface DBDs; evidence of collective effect. *Journal of Physics D-Applied Physics*, 40, 7698.
- Atten, P., Pang, H. L., & Reboud, J. L. (2009). Study of dust removal by standing-wave electric curtain for application to solar cells on mars. *IEEE Transactions on Industry Applications*, 45(1), 75-86.
- Bartnikas, R., Radu, I., & Wertheimer, M. R. (2007). Dielectric electrode surface effects on atmospheric pressure glow discharges in helium. *IEEE Transactions on Plasma Science*, 35(5), 1437-1447.
- Bhosle, S., Zissis, G., Damelincourt, J. J., & Dawson, F. P. (2004). Calculation of the impedance of an axisymmetric DBD lamp for power supply design purposes. *Conference Record of the 2004 IEEE Industry Applications Conference*, 3, 1667-1670.
- Borcia, G., Anderson, C. A., & Brown, N. M. D. (2004). The surface oxidation of selected polymers using an atmospheric pressure air dielectric barrier discharge. Part I. *Applied Surface Science*, 221, 203-214.
- Carman, R. J., Kane, D. M., & Ward, B. K. (2010). Enhanced performance of an EUV light source ( $\lambda = 84$  nm) using short-pulse excitation of a windowless dielectric barrier discharge in neon. *Journal of Physics D-Applied Physics*, 43(2), 025205.

- Chen, Z. Y. (2003). PSpice simulation of one atmosphere uniform, glow discharge plasma (OAUGDP) reactor systems. *IEEE Transactions on Plasma Science*, 31(4), 511-520.
- Chirokov, A., Gutsol, A., Fridman, A., Sieber, K. D., Grace, J. M., & Robinson, K. S. (2006). A study of two-dimensional microdischarge pattern formation in dielectric barrier discharges. *Plasma Chemistry and Plasma Processing*, 26(2), 127-135.
- De Geyter, N., Morent, R., Gengembre, L., Leys, C., Payen, E., Van Vlierberghe, S., et al. (2008). Increasing the hydrophobicity of a PP film using a helium/CF<sub>4</sub> DBD treatment at atmospheric pressure. *Plasma Chemistry and Plasma Processing*, 28(2), 289-298.
- Eliasson, B., Egli, W., & Kogelschatz, U. (1994). Modeling of dielectric barrier discharge chemistry. *Pure and Applied Chemistry*, 66(8), U1766-U1778.
- Eliasson, B., Hirth, M., & Kogelschatz, U. (1987). Ozone synthesis from oxygen in dielectric barrier discharges. *Journal of Physics D-Applied Physics*, 20(11), 1421-1437.
- Eliasson, B., & Kogelschatz, U. (1991). Modeling and applications of silent discharge plasmas. *IEEE Transactions on Plasma Science*, 19(2), 309-323.
- Enloe, C. L., McHarg, M. G., & McLaughlin, T. E. (2008). Time-correlated force production measurements of the dielectric barrier discharge plasma aerodynamic actuator. *Journal of Applied Physics*, 103(7), 073302.
- Esen, P., Riccardi, C., Zanini, S., Tontini, M., Poletti, G., & Orsini, F. (2005). Surface modification of PET film by a DBD device at atmospheric pressure. *Surface & Coatings Technology*, 200(1-4), 664-667.
- Falkenstein, Z., & Coogan, J. J. (1997). Microdischarge behaviour in the silent discharge of nitrogen-oxygen and water-air mixture. *Journal of Physics D-Applied Physics*, 30(5), 817-825.

- Ficker, T. (1995). Fractal statistics of partial discharges with polymeric samples. *Journal of Applied Physics*, 78(9), 5289-5295.
- Ficker, T. (2003). Electron avalanches I - Statistics of partial microdischarges in their pre-streamer stage. *IEEE Transactions on Dielectrics and Electrical Insulation*, 10(4), 689-699.
- Ficker, T., Macur, J., Pazdera, L., Kliment, M., & Filip, S. (2001). Simplified digital acquisition of microdischarge pulses. *IEEE Transactions on Dielectrics and Electrical Insulation*, 8(2), 220-227.
- Flores-Fuentes, A., Pena-Eguiluz, R., Lopez-Callejas, R., Mercado-Cabrera, A., Valencia-Alvarado, R., Barocio-Delgado, S., et al. (2009). Electrical model of an atmospheric pressure dielectric barrier discharge cell. *IEEE Transactions on Plasma Science*, 37(1), 128-134.
- Fridman, G., Peddinghaus, M., Ayan, H., Fridman, A., Balasubramanian, M., Gutsol, A., et al. (2006). Blood coagulation and living tissue sterilization by floating electrode dielectric barrier discharge in air. *Plasma Chemistry and Plasma Processing*, 26(4), 425-442.
- Fridman, G., Shereshevsky, A., Jost, M. M., Brooks, A. D., Fridman, A., Gutsol, A., et al. (2007). Floating electrode dielectric barrier discharge plasma in air promoting apoptotic behavior in melanoma skin cancer cell lines. *Plasma Chemistry and Plasma Processing*, 27(2), 163-176.
- Gherardi, N., Gouda, G., Gat, E., Ricard, A., & Massines, F. (2000). Transition from glow silent discharge to micro-discharges in nitrogen gas. *Plasma Sources Science & Technology*, 9(3), 340-346.

- Gherardi, N., & Massines, F. (2001). Mechanisms controlling the transition from glow silent discharge to streamer discharge in nitrogen. *IEEE Transactions on Plasma Science*, 29(3), 536-544.
- Goujard, V., Tatibouet, J. M., & Batiot-Dupeyrat, C. (2011). Carbon dioxide reforming of methane using a dielectric barrier discharge reactor: effect of helium dilution and kinetic model. *Plasma Chemistry and Plasma Processing*, 31(2), 315-325.
- Gulski, E., & Kreuger, F. H. (1990). Computer-aided analysis of discharge patterns. *Journal of Physics D-Applied Physics*, 23(12), 1569-1575.
- Hashim, S. A., Wong, C. S., Abas, M. R., & Dahlan, K. Z. (2007). Feasibility study on the removal of nitric oxide (NO) in gas phase using dielectric barrier discharge reactor. *Malaysia journal of science*, 26(2) 111-116.
- Herzberg, G. (1957). *Molecular spectra and molecular structure I; Spectra of diatomic molecules*. New York: D. Van Nostrand.
- Hoder, T., Brandenburg, R., Basner, R., Weltmann, K. D., Kozlov, K. V., & Wagner, H. E. (2010). A comparative study of three different types of barrier discharges in air at atmospheric pressure by cross-correlation spectroscopy. *Journal of Physics D-Applied Physics*, 43(12), 124009.
- Jidenko, N., Petit, M., & Borra, J. (2002). Volatile organic compounds depollution by dielectric barrier discharge in porous media. *Int. Symp. On high Pressure Low Temperature Plasma Chemistry (Hakone VIII), Contributed paper*, 364-368.
- Jidenko, N., Petit, M., & Borra, J. P. (2006). Electrical characterization of microdischarges produced by dielectric barrier discharge in dry air at atmospheric pressure. *Journal of Physics D-Applied Physics*, 39(2), 281-293.
- Kalghatgi, S. U., Fridman, G., Fridman, A., Friedman, G., & Clyne, A. M. (2008). Non-thermal dielectric barrier discharge plasma treatment of endothelial cells. *2008*

*30th Annual International Conference of the IEEE Engineering in Medicine and Biology Society, Vols 1-8, 3578-3581.*

- Kamchouchi, H. E., & Zaky, A. A. (1975). A direct method for the calculation of the edge capacitance of thick electrodes. *Journal of Physics D-Applied Physics*, 8, 1365–1371.
- Kanazawa, S., Kogoma, M., Moriwaki, T., & Okazaki, S. (1988). Stable glow plasma at atmospheric-pressure. *Journal of Physics D-Applied Physics*, 21(5), 838-840.
- Kersten, H., Steffen, H., & Behnke, J. K. (1996). Investigations on plasma-assisted surface cleaning of aluminum contaminated with lubricants. *Surface & Coatings Technology*, 86/87, 762-768.
- Kogelschatz, U. (1990). Silent Discharges for the generation of ultraviolet and vacuum ultraviolet excimer radiation. *Pure and Applied Chemistry*, 62(9), 1667-1674.
- Kogelschatz, U. (2002). Filamentary, patterned, and diffuse barrier discharges. *IEEE Transactions on Plasma Science*, 30(4), 1400-1408.
- Kogelschatz, U. (2003). Dielectric-barrier discharges: Their history, discharge physics, and industrial applications. *Plasma Chemistry and Plasma Processing*, 23(1), 1-46.
- Kogelschatz, U., Eliasson, B., & Egli, W. (1997). Dielectric-barrier discharges. Principle and applications. *Journal De Physique Iv*, 7(C4), 47-66.
- Kogelschatz, U., Eliasson, B., & Egli, W. (1999). From ozone generators to flat television screens: history and future potential of dielectric-barrier discharges. *Pure and Applied Chemistry*, 71(10), 1819-1828.
- Kolb, J. F., Mohamed, A. A. H., Price, R. O., Swanson, R. J., Bowman, A., Chiavarini, R. L., et al. (2008). Cold atmospheric pressure air plasma jet for medical applications. *Applied Physics Letters*, 92(24).

- Kozlov, K. V., Brandenburg, R., Wagner, H. E., Morozov, A. M., & Michel, P. (2005). Investigation of the filamentary and diffuse mode of barrier discharges in N<sub>2</sub>/O<sub>2</sub> mixtures at atmospheric pressure by cross-correlation spectroscopy. *Journal of Physics D-Applied Physics*, 38(4), 518-529.
- Kozlov, K. V., Wagner, H. E., Brandenburg, R., & Michel, P. (2001). Spatio-temporally resolved spectroscopic diagnostics of the barrier discharge in air at atmospheric pressure. *Journal of Physics D-Applied Physics*, 34, 3164-3176.
- Kriegseis, J., Moller, B., Grundmann, S., & Tropea, C. (2011). Capacitance and power consumption quantification of dielectric barrier discharge (DBD) plasma actuators. *Journal of Electrostatics*, 64 (4), 302-312.
- Kwon, O. J., Myung, S. W., Lee, C. S., & Choi, H. S. (2006). Comparison of the surface characteristics of polypropylene films treated by Ar and mixed gas (Ar/O<sub>2</sub>) atmospheric pressure plasma. *Journal of Colloid and Interface Science*, 295(2), 409-416.
- Kwon, O. J., Tang, S., Myung, S. W., Lu, N., & Choi, H. S. (2005). Surface characteristics of polypropylene film treated by an atmospheric pressure plasma. *Surface & Coating Technology*, 192(1), 1-10.
- Lagmich, Y., Callegari, T., Pitchford, L. C., & Boeuf, J. P. (2008). Model description of surface dielectric barrier discharges for flow control. *Journal of Physics D-Applied Physics*, 41(9).
- Laurentie, J. C., Jolibois, J., & Moreau, E. (2009). Surface dielectric barrier discharge: Effect of encapsulation of the grounded electrode on the electromechanical characteristics of the plasma actuator. *Journal of Electrostatics*, 67(2-3), 93-98.
- Li, M., Li, C. R., Zhan, H. M., Xu, J. B., & Wang, X. (2008). Effect of surface charge trapping on dielectric barrier discharge. *Applied Physics Letters*, 92(3), 031503.

- Liu, S. H., & Neiger, M. (2001). Excitation of dielectric barrier discharges by unipolar submicrosecond square pulses. *Journal of Physics D-Applied Physics*, 34(11), 1632-1638.
- Liu, S. H., & Neiger, M. (2003). Electrical modelling of homogeneous dielectric barrier discharges under an arbitrary excitation voltage. *Journal of Physics D-Applied Physics*, 36(24), 3144-3150.
- Lofthus, A., & Krupenir, P. H. (1977). The spectrum of molecular nitrogen. *Journal of Physical and Chemical Reference Data*, 6, 113.
- Lomaev, M. I., Sosnin, E. A., Tarasenko, V. F., Shits, D. V., Skakun, V. S., Erofeev, M. V., Lisenko, A. A. (2006). Capacitive and barrier discharge excilamps and their applications (Review). *Instruments and Experimental Techniques*, 49(5), 595-616.
- Luo, H., Liang, Z., Lv, B., Wang, X., Guan, Z., & Wang, L. (2007). Observation of the transition from a Townsend discharge to a glow discharge in helium at atmospheric pressure. *Applied Physics Letters*, 91(22), 221504.
- Manley, T. C. (1943). The Electric characteristics of the ozonator discharge. *Trans. Electrochem. Soc.*, 84, 83-96.
- Manojlovic, D., Popara, A., Dojcinovic, B. P., Nikolic, A., Obradovic, B. M., Kuraica, M. M., et al. (2008). Comparison of two methods for removal of arsenic from potable water. *Vacuum*, 83(1), 142-145.
- Massines, F., Gherardi, N., Naude, N., & Segur, P. (2005). Glow and Townsend dielectric barrier discharge in various atmosphere. *Plasma Physics and Controlled Fusion*, 47, B577-B588.
- Massines, F., Gherardi, N., Naude, N., & Segur, P. (2009). Recent advances in the understanding of homogeneous dielectric barrier discharges. *European Physical Journal-Applied Physics*, 47(2), 22805.

- Massines, F. & Gouda, G. (1998). A comparison of polypropylene-surface treatment by filamentary, homogeneous and glow discharges in helium at atmospheric pressure. *Journal of Physics D-Applied Physics*, 31(24), 3411-3420.
- Massines, F., Gouda, G., Gherardi, N., Duran, M., & Croquesel, E. (2001). The role of dielectric barrier discharge atmosphere and physics on polypropylene surface treatment. *Plasma and Polymers*, 6, 35.
- Massines, F., Segur, P., Gherardi, N., Khamphan, C., & Ricard, A. (2003). Physics and chemistry in a glow dielectric barrier discharge at atmospheric pressure: diagnostics and modelling. *Surface & Coatings Technology*, 174, 8-14.
- Moreau, E. (2007). Airflow control by non-thermal plasma actuators. *Journal of Physics D-Applied Physics*, 40(3), 605-636.
- Naude, N., Cambronne, J. P., Gherardi, N., & Massines, F. (2005). Electrical model and analysis of the transition from an atmospheric pressure Townsend discharge to a filamentary discharge. *Journal of Physics D-Applied Physics*, 38(4), 530-538.
- Okazaki, S., Kogoma, M., Uehara, M., & Kimura, Y. (1993). Appearance of stable glow-discharge in air, argon, oxygen and nitrogen at atmospheric-pressure using a 50-Hz source. *Journal of Physics D-Applied Physics*, 26(5), 889-892.
- Pal, U. N., Sharma, A. K., Soni, J. S., Kr, S., Khatun, H., Kumar, M., et al. (2009). Electrical modelling approach for discharge analysis of a coaxial DBD tube filled with argon. *Journal of Physics D-Applied Physics*, 42(4), 045213.
- Petit, M., Jidenko, N., Goldman, A., Goldman, M., & Borra, J. P. (2002). Electrical characterization of gas discharges using a numerical treatment. Application to dielectric barrier discharges. *Review of Scientific Instruments*, 73(7), 2705-2712.
- Ramasamy, R. K., Rahman, N. A., & Wong, C. S. (2001). Effect of temperature on the ozonation of textile waste effluent. *Coloration Technology*, 117(2), 95-97.



- Reichen, P., Sonnenfeld, A., & von Rohr, P. R. (2010). Influence of increased velocity on the statistical discharge characteristics of He and air barrier discharges. *Journal of Physics D-Applied Physics*, 43(2), 025207.
- Roth, J. R., Rahel, J., Dai, X., & Sherman, D. M. (2005). The physics and phenomenology of one atmosphere uniform glow discharge plasma (OAUGDP (TM)) reactors for surface treatment applications. *Journal of Physics D-Applied Physics*, 38(4), 555-567.
- Siddiqui, M. S., Amy, G. L., & Murphy, B. D. (1997). Ozone enhanced removal of natural organic matter from drinking water sources. *Waste Air Treat. Res.*, 31(12), 3098-3106.
- Siliprandi, R. A., Roman, H. E., Barni, R., & Riccardi, C. (2008). Characterization of the streamer regime in dielectric barrier discharges. *Journal of Applied Physics*, 104(6), 063309.
- Somerville, I., & Vidaud, P. (1985). Surface spreading of charge due to ohmic conduction. *Proceedings of the Royal Society of London Series a-Mathematical Physical and Engineering Sciences*, 399(1817), 277-293.
- Tanino, M., Xilu, W., Takashima, K., Katsura, S., & Mizuno, A. (2007). Sterilization using dielectric barrier discharge at atmospheric pressure. *International Journal of Plasma Environmental Science & Technology*, 1(1), 102-107.
- Valdivia-Barrientos, R., Pacheco-Sotelo, J., Pacheco-Pacheco, M., Benitez-Read, J. S., & Lopez-Callejas, R. (2006). Analysis and electrical modelling of a cylindrical DBD configuration at different operating frequencies. *Plasma Sources Science & Technology*, 15(2), 237-245.
- Vanbrunt, R. J., & Cernyar, E. W. (1991). Influence of memory propagation on phase-resolved stochastic-behavior of AC-generated partial discharges. *Applied Physics Letters*, 58(23), 2628-2630.

- Vanbrunt, R. J., Cernyar, E. W., & Vonglahn, P. (1993). Importance of unraveling memory propagation effects in interpreting data on partial discharge statistics. *IEEE Transactions on Electrical Insulation*, 28(6), 905-916.
- Vanbrunt, R. J., Misakian, M., Kulkarni, S. V., & Lakdawala, V. K. (1991). Influence of a dielectric barrier on the stochastic-behavior of trichel-pulse corona. *IEEE Transactions on Electrical Insulation*, 26(3), 405-415.
- Vanbrunt, R. J., Vonglahn, P., & Las, T. (1995). Nonstationary behavior of partial discharge during discharge induced aging of dielectrics. *IEEE Proceedings-Science Measurement and Technology*, 142(1), 37-45.
- Wagner, H. E., Brandenburg, R., Kozlov, K. V., Sonnenfeld, A., Michel, P., & Behnke, J. F. (2003). The barrier discharge: basic properties and applications to surface treatment. *Vacuum*, 71(3), 417-436.
- Wang, X., Luo, H., Liang, Z., Mao, T., & Ma, R. (2006). Influence of wire mesh electrodes on dielectric barrier discharge. *Plasma Sources Science & Technology*, 15(4), 845-848.
- Wang, C., Zhang, G., Wang, X., & He, X. (2010). The effect of air plasma on barrier dielectric surface in dielectric barrier discharge. *Applied Surface Science*, 257(5), 1698-1702.
- Weltmann, K. D., Kindel, E., von Woedtke, T., Hahnel, M., Stieber, M., & Brandenburg, R. (2010). Atmospheric-pressure plasma sources: Prospective tools for plasma medicine. *Pure and Applied Chemistry*, 82(6), 1223-1237.
- Williamson, J. M., & DeJoseph, C. A. (2003). Determination of gas temperature in an open-air atmospheric pressure plasma torch from resolved plasma emission. *Journal of Applied Physics*, 93(4), 1893-1898

- Wong, C. S., Hashim, S. A., Abas, M. R., & Dahlan, K. Z. H. (2010). Discharge Based Processing Systems for Nitric Oxide Remediation. *Sains Malaysiana*, 39(6), 981-987.
- Xia, L. Y., Huang, L., Shu, X. H., Zhang, R. X., Dong, W. B., & Hou, H. Q. (2008). Removal of ammonia from gas streams with dielectric barrier discharge plasmas. *Journal of Hazardous Materials*, 152(1), 113-119.
- Xu, G. M., Zhang, G. J., Shi, X. M., Ma, Y., Wang, N., & Li, Y. (2009). Bacteria inactivation using DBD plasma jet in atmospheric pressure argon. *Plasma Science & Technology*, 11(1), 83-88.
- Yi, C. H., Lee, Y. H., & Yeom, G. Y. (2003). The study of atmospheric pressure plasma for the surface cleaning. *Surface & Coatings Technology*, 171(1-3), 237-240.
- Zhang, C., Shao, T., Long, K. H., Yu, Y., Wang, J., Zhang, D. D., et al. (2010). Surface treatment of polyethylene terephthalate films using DBD excited by repetitive unipolar nanosecond pulses in air at atmospheric pressure. *IEEE Transactions on Plasma Science*, 38(6), 1517-1526.
- Zhang, C., Shao, T., Yu, Y., Niu, Z., Yan, P., & Zhou, Y. X. (2010). Comparison of experiment and simulation on dielectric barrier discharge driven by 50 Hz AC power in atmospheric air. *Journal of Electrostatics*, 68(5), 445-452.

## Appendix: Research outputs

Abstract of accepted paper in Sains Malaysiana

### **The Electrical Characteristics and Modeling of a Filamentary Dielectric Barrier Discharge in Atmospheric Air**

**(Ciri-Ciri Elektrik Dan Kemodelan Suatu Nyahcas Dielektrik Berpenghadang Dalam Udara Atmosfera)**

W.H. Tay, S.L. Yap and C.S. Wong

*Plasma Technology Research Centre, Physics Department, University of Malaya  
50603 Kuala Lumpur, Malaysia*

#### **Abstract**

The electrical characteristics of a filamentary dielectric barrier discharge (DBD) are studied experimentally and numerically. The DBD system has a parallel plate electrodes geometry is powered by a 50 Hz power supply and operated at atmospheric air. A dynamic electric circuit model considering the discharge region and the non-discharge region being connected by a surface resistance is proposed. Simulation using this model is shown to fit the experimentally measured QV diagram satisfactorily. The effects of the air gap distance and the dielectric surface on the discharge behavior are then investigated. It is found that the surface resistivity of the dielectric is one of the important parameters governing the discharge behavior.

**Keywords:** *Dielectric Barrier Discharge, Filamentary Discharge, Electrical characteristics, Electrical Modeling.*

#### **Abstrak**

Ciri-ciri nyahcas dielektrik berpenghadang (DBD) telah dikaji secara eksperimen dan berangka. Sistem DBD yang mengandungi dua elektrod plat yang selari dikuasakan dengan bekalan kuasa yang 50 Hz and difungsi dalam udara atmosfera. Satu model elektrik yang mengambil kira rantau tidak bernyahcas and rantau bernyahcas telah dicadangkan. Dalam model elektrik ini, rantau tidak bernyahcas and rantau bernyahcas disambungi dengan satu rintangan permukaan. Keputusan simulasi berjaya menyamai keputusan Lissajous QV yang didapati daripada eksperimen. Kesan jarak jurang ruang dan rintangan permukaan dielektrik dalam DBD juga dikaji dan didapati bahawa rintangan permukaan dielektrik adalah satu parameter yang penting untuk mengawal sifat nyahcas.

**Kata kunci:** *nyahcas dielektrik berpenghadang, nyahcas filamen, ciri-ciri elektrik, model elektrik.*

**Abstract of published paper in proceedings.**

National Conference on Physics (PERFIK2009)  
AIP conference proceedings

## **The Electrical Characteristics of a Filamentary Dielectric Barrier Discharge**

W. H. Tay, S. L. Yap and C. S. Wong

*Plasma Research Laboratory, Physics Department, University of Malaya  
50603 Kuala Lumpur, Malaysia.*

**Abstract.** The electrical characteristics of a filamentary dielectric barrier discharge using parallel-plate electrodes geometry were statistically studied. The dielectric barrier discharge (DBD) system was powered by a 50 Hz power supply and operated at atmospheric pressure. The influence of the air gap and position of dielectric on the discharge had been investigated. It was found that the air gap distance and position of dielectric had significant influence on the discharge current pulse. The results showed that discharge with large distance between the high voltage electrode and the dielectric would generate higher current pulses during the positive cycle. The discharge energy of single pulse was also determined.

**Keywords:** *Dielectric Barrier Discharge, Filamentary Discharge, Atmospheric discharge.*

**PACS:** *52.80.-s, 52.38.Hb, 52.80.Mg*

## **Abstract of presentation**

The 6<sup>th</sup> Mathematics and Physical Sciences Graduates Congress (MPSGC 2010)  
Faculty of Science, University of Malaya.

### **The Statistical Characteristics of Dielectric Barrier Discharge Powered by 50 Hz in Atmospheric Air**

W.H. Tay, S. L. Yap, and C. S. Wong

*Plasma Research Center, Department of Physic, University of Malaya  
50603 Kuala Lumpur, Malaysia.*

**Abstract.** Applications of the plasma technologies based on the dielectric-barrier discharge (DBD) are numerous and involve many industries. A DBD operated at low frequency power supply of 50 Hz is used here because of its simplicity and effective. In this paper, a representative statistical analysis of the dielectric barrier discharge characteristics is studied. The effects due to different driven voltage and space gap distance on the maximum current pulse, amount of the charge, and breakdown voltage are investigated. A simple model is proposed to estimate the probability density distribution of current amplitude based on the experimental result.

**Keywords:** *Dielectric Barrier Discharge, Filamentary Discharge, Atmospheric discharge*